Ab initio and experimental techniques for studying non-stoichiometry and oxygen transport in mixed conducting oxides

Thesis by

Chirranjeevi Balaji Gopal

In Partial Fulfillment of the Requirements

for the Degree of

Doctor of Philosophy

California Institute of Technology

Pasadena, California

2015

(Defended August 15, 2014)

Acknowledgments

My life as a graduate student at Caltech has been nothing short of life-changing and I owe this to a lot of people. First out, my parents have always put my ambitions and interests above all else and backed me to come to Caltech. I am tremendously grateful to my advisers, Axel van de Walle and Sossina Haile for mentoring me through the years. Transitioning from simulations to full-blown experiments requires patience, trust and genuine excitement from the adviser. Sossina supported me with all this and much more.

I met some really smart, inspiring and yet humble people here, many of who have had a lasting influence on my life. In particular, I can't thank Cindy enough for the personal and academic support she provided me with and numerous life lessons in my formative years here. Aron and Steve, with their towering brilliance and (periodically) near-juvenile maturity, made my time at Caltech intellectually stimulating and fun in equal measure. I am also grateful to PT, Alex(s), Himanshu, Christina, Joel, Vanessa and many more friends for making me feel home at work. These are all wonderful people that I would like to always be in touch with. Thanks to the caltech alpine club, I got hooked to mountains, snow, and other outdoorsy pursuits that are borderline suffer-fests on occasions and met many a colorful character.

I would also like to acknowledge my colleagues from Axel's group - PT, Steve, Qijun, Greg and Ljuba for many engaging discussions - scientific or otherwise. These are among the smartest people I have come to know. Big thanks to Aron, William, Tae-sik, Yong, Woochul and other Haile group members for helping me get set in the lab. I would also like to thank Arun, my SURF student for some great work in the summer of 2012. Thanks to Anu and Vanessa for proofreading parts of the thesis.

Caltech is truly a remarkable place to mature as a scientist and I feel very fortunate to have been in such good academic company.

Lastly, but very importantly, I would like to express my love and gratitude to Jenny for the unconditional love, joy and encouragement she has offered me over the last year and making me realize what is truly valuable in life.

Portions of this thesis have been adapted with permission from the following sources in which I am the first author.

- Chirranjeevi Balaji Gopal and Axel van de Walle, *Ab initio thermodynamics of intrinsic oxygen vacancies in ceria*, Physical Review B, 86, 13, 134117, 2012
- Chirranjeevi Balaji Gopal and Sossina M Haile, *An electrical conductivity relaxation study of oxygen transport in samarium doped ceria*, Journal of Materials Chemistry A, 2, 7, 2405-2417, 2014
- Chirranjeevi Balaji Gopal, Arun Asundi and Sossina M Haile, *Effect of Zr addition on oxygen transport in ceria : an electrical conductivity relaxation study*, (in preparation)
- Chirranjeevi Balaji Gopal and Sossina M Haile, *Electrochemical determination of non-stoichiometry in mixed conducting oxide thin films*, (in preparation)
- Chirranjeevi Balaji Gopal and Sossina M Haile, *Membrane reactor for thermochemically driven fuel production*, Provisional Patent, CIT-6744-P

Abstract

The ability of cerium oxide ($CeO_{2-\delta}$, also called ceria), to vary its oxygen stoichiometry in response to changes in temperature or oxygen activity is key to many of its applications in catalysis and electrochemical energy storage and conversion. This thesis explores *ab initio* and experimental approaches to study the fundamental thermodynamic and oxygen transport properties of ceria ($M_xCe_{1-x}O_{2-\delta}$), but the methods are applicable to other mixed conducting oxides as well.

In the first part of the thesis, a computational thermodynamics approach that integrates quantum mechanical and statistical ensemble-based simulations is used to calculate the reduction-oxidation thermodynamics of non-stoichiometric ceria entirely from first principles. This procedure is well understood and has been successfully implemented for metallic alloys, but has not been extended to correlated electron systems such as ceria, for which the physics of electronic structure calculations is significantly more complicated. Density functional calculations were used to obtain the ground state energies of ceria with vacancy concentrations ranging from fully stoichiometric up to $\delta = 0.25$. For each δ, numerous vacancy configurations were sampled to capture the interactions between vacancies and other atoms. Using the frozen phonon method, lattice dynamical calculations of phonon density of states were performed for various δ. Based on the ground state energies of nearly 40 structures, a cluster expansion Hamiltonian was used to parametrize the energy as a polynomial in occupation variables. The vibrational energies were used to make the Hamiltoninan temperature dependent. Lattice Monte Carlo (MC) simulations using the cluster expansion Hamiltonian were then used to study, for the first time, the effect of temperature and chemical potential on the vacancy concentration in ceria from first principles.

The temperature composition phase diagram constructed from the MC simulations successfully reproduced the experimentally reported miscibility gap. The inclusion of vibrational and electronic contributions to the entropy made the agreement quantitative. Further, the partial molar enthalpy and entropy of reduction as a function of δ were extracted and found to deviate significantly from those of an ideally behaved system. The deviations were quantified by calculating the Warren-Cowley short range order parameters. This was the first demonstration of an *ab initio* approach being used to accurately model the defect thermodynamics of a correlated electron system without resorting to experimental inputs. Using ceria as benchmark material, this project lays the groundwork for a computational approach to screen new oxides for thermochemical cycling.

The rest of the thesis describes experimental investigations of oxygen transport and non-stoichiometry in doped and undoped ceria. Oxygen transport studies were performed using electrical conductivity relaxation (ECR). In ECR, a small step change in pO_2 forces the sample non-stoichiometry δ, and other dependent properties such as electrical conductivity, to equilibrate to a new value. The rate of this re-equilibration is governed by the bulk oxygen diffusivity, D_{Chem}, and surface reaction rate constant, k_S – the two principal kinetic properties. By fitting the solution to Fick's second law, with the appropriate boundary conditions, to the conductivity relaxation profile, D_{Chem} and k_S can be extracted. The instrumental capability for performing electrical conductivity relaxation experiments was set up and a systematic data analysis procedure was developed to reliably and accurately extract D_{Chem} and or k_S. The experimental and data analytical methodologies were successfully benchmarked with 15 mol% Sm doped ceria, for which approximate values of the two principal transport properties, bulk oxygen diffusivity, D_{Chem}, and surface reaction rate constant, k_S, can be found in the literature. An unexpectedly high p-type electronic transference number enabled ECR measurements under oxidizing conditions. A systematic data analysis procedure was developed to permit reliable extraction of the kinetic parameters even in the general case of simultaneous bulk and surface limitation. When the surface kinetics were too sluggish compared to bulk diffusion, Pt catalyst nanoparti-

cles were sputtered to catalyze the surface reaction and enable extraction of D_{Chem}. The D_{Chem} from this study showed excellent qualitative and quantitative agreement with expected values, falling in the range from $\sim 2 \times 10^{-5}$ to 2×10^{-4} cm^2/s. The surface reaction constant under H_2/H_2O mixtures also showed good agreement with literature results. Remarkably, this value increased by a factor of 40 under mixtures of CO/CO_2 or O_2/Ar. This observation suggests kinetic advantages for production of CO rather than H_2 in a two-step solar-driven thermochemical process based on samarium doped ceria.

Using ECR, the effect of 20% Zr addition on the electrical conductivity and oxygen transport properties of ceria as a function of pO_2 and T was investigated. Under oxidizing conditions, both $CeO_{2-\delta}$ and $Zr_{0.2}Ce_{0.8}O_{2-\delta}$(ZDC20) showed n type, mixed conduction. The conductivity of ZDC20 was two orders of magnitude higher than that of undoped ceria. Contrary to previous studies, we found that Zr addition does not change the electronic mobility in this pO_2 regime. The enhancement in conductivity is a consequence of higher vacancy concentration in ZDC20 under identical conditions compared to ceria. Under reducing conditions, while the n-type conductivity of ceria continued to increase with decreasing pO_2, that of ZDC20 reached a broad maximum, eventually decreasing with pO_2 (p-type) despite increasing carrier concentration. We show that the electronic mobility becomes strongly concentration dependent at high oxygen non-stoichiometry. This leads to a marked decrease in mobility with increase in δ, causing the conductivity to roll over from n to p type. The chemical diffusion coefficient and surface reaction rate constant of both ceria and ZDC20 showed strong dependence on pO_2 under oxidizing conditions, decreasing by nearly an order of magnitude between 10^{-2} atm and 10^{-5} atm. The unexpectedly high sensitivity to pO_2 was ascribed to the effect of extrinsic vacancies generated by trace quantities of lower valence cation impurities, that dramatically increase both the absolute value of the thermodynamic factor and its sensitivity to pO_2 close to stoichiometry. Overall, the addition of Zr lowers the D_{Chem} and k_S of ceria in the temperature and oxygen partial pressure range of this study, the effect being more pronounced under reducing conditions. Beyond its relevance to ceria, this work demonstrates the potential of

ECR to isolate the effect of kinetics from thermodynamics of the real thermochemical cycle, reveal the limiting transport parameters, and ultimately guide microstructure design for maximizing the rate of fuel production.

Lastly, we improve upon an existing formalism to calculate the oxygen non-stoichiometry in thin films of mixed conducting oxides using AC impedance spectroscopy. Cerium oxide was once again chosen as the benchmarking material, since it shows both ideal and non-ideal thermodynamic behavior under different conditions, and has been well studied in its bulk form. In this method, the impedance response of dense, thin films of $CeO_{2-\delta}$ deposited on a $Y_{0.84}Zr_{0.16}O_{1.92}$ (YSZ) substrate was measured using AC impedance spectroscopy. To explore potential grain boundary effects on bulk thermodynamic properties. A physically derived equivalent circuit model was fit to the impedance response to extract a quantity called the 'chemical capacitance', which was subsequently related to the non-stoichiometry. Previous studies employing this method were restricted to systems that can be described using ideal solution thermodynamics, which allows simplifications to the theoretical treatment of their capacitance. Apart from extending this technique to a non-ideally behaved oxide, we report excellent agreement between the non-stoichiometry of single crystal and polycrystalline films and that of bulk ceria. By virtue of using thin films, equilibration times are dramatically decreased, enabling faster measurements compared to bulk techniques like thermogravimetry and coulometric titration. Further, the electrochemical method is ideal for thin films, for which the mass changes are below the detection limits of bulk techniques.

Contents

List of Figures

List of Tables

Chapter 1

Introduction and background

1.1 Big picture

Fossil fuels, comprising coal, natural gas and petroleum, are the primary source of energy in the modern world. The high energy density of these carbon rich compounds and the ability to easily store and transport them, has spearheaded the industrial and economic development of entire societies worldwide. As of 2012, 82%[3] of the total energy use in the United States was supplied by fossil fuels. However, fossil fuels take millions of years to form, and known, viable reserves are being depleted much faster than new ones are being created. Moreover, indiscriminate use of fossil fuels has drastically increased the concentration of greenhouse gases in the atmosphere, contributing to global climate disruption and worsening air quality. At 26%, the burning of coal, natural gas, and oil for electricity is the single largest source of greenhouse gas emissions globally[3]. This has led to the need for sustainable energy solutions to help ease the dependence on, if not facilitate a complete removal from fossil energy.

Solar energy is virtually inexhaustible and is the biggest renewable energy source available to us. At any instant, 176000 terawatts of solar radiation strikes the earth. In comparison, the global power consumption, as of 2012, was 16 terawatts. If only 0.1% of the incident solar energy were to be utilized at 10% efficiency, we would meet the global energy needs using solar[4]. However, proliferation of solar power generation has been limited by lack of effective storage technologies. Thus, one of

the biggest objectives of sustainable energy research is developing a means to harvest and store solar energy and make it available for use when necessary.

1.2 Storing solar energy in chemical bonds

Storing energy in chemical bonds is highly attractive for the same reasons that fossil fuels are extremely sought after – high energy density, ease of storage and transportation, and demand based use. Efforts are being made world wide to improve the energy density of batteries for efficient storage of electricity and to develop efficient and economically viable methods of hydrogen production from water. Hydrogen is an excellent and clean fuel, whose utilization produces water as the only waste product. There are a variety of ways to produce hydrogen, each with its own merits and demerits. Thermolysis using concentrated solar radiation is the most direct means of dissociating steam and generating hydrogen. However, to dissociate 50% of the water molecules, temperatures in excess of 3000 °C are necessary, placing severe requirements on the materials used to engineer such a device. Another possible route is to convert solar energy to electricity using photovoltaic cells, which could then be used to power an electrolyzer for water electrolysis. Rapid strides are being made to improve the efficiency of photovoltaics and to develop better water oxidation catalysts. By combining the light harvesting and water splitting steps using a photoelectrochemical cell, significant reduction in capital costs and improvement in system efficiency can be achieved. Despite the advantage of low temperature operation, photoelectrochemical cells use only a limited portion (visible, UV) of the solar spectrum, require exotic catalysts and suffer from serious material limitations. In this regard, photoactive semiconductors with desirable band gap, band alignment with the electrochemical potentials for oxygen/hydrogen evolution reactions, rapid charge transfer kinetics and long term stability in aqueous media are being actively researched. There are several excellent reviews describing the concepts and recent developments in the field, dubbed 'artificial photosynthesis'[5] and identifying the design constraints and research breakthroughs that are necessary to make solar water-splitting cells com-

mercially viable[6].

An alternate approach is to use solar energy to thermochemically split water using the redox active nature of certain metal oxides. The process is typically carried out in two steps. First, concentrated solar energy is used to release oxygen from the metal oxide by partially or completely reducing it at a high temperature step. In the second step, the reduced metal oxide or metal is re-oxidized back to the original state by reacting it with steam (H_2O), generating hydrogen (H_2). Hydrogen, together with carbon dioxide, can subsequently be used as a feedstock for the Fischer Tropsch process to produce methane, or can be delivered to fuel cells to produce electricity.

Metal-metal oxide based redox systems (e.g. Zn/ZnO, FeO/Fe_3O_4) have been been studied for over 35 years[7, 8, 9, 10]. The large gravimetric changes associated with complete reduction of the oxide translate to large theoretical fuel productivities. However, there are considerable engineering challenges and kinetic impediments due to extremely high reduction temperatures (>2500 K), the formation of an impervious oxide layer on the surface, and the need to use nanoparticles for reaction sufficient kinetics[11]. To prevent aggressive coarsening of particles at elevated temperatures, catalyst supports such as zirconia are used at the cost of lower gravimetric fuel producivity[12] (since zirconia is redox-inactive). Most of these shortcomings are overcome using thermochemical cycles based on non-stoichiometric oxides. In non-stoichiometric oxides, only a fraction of the stoichiometric quantity of oxygen is released and reincorporated, implying lower fuel productivity per cycle compared to completely reduced oxides, but the oxygen exchange occurs without loss of the original crystal structure. Further, a number of non-stoichiometric oxides are well known for their high temperature stability, excellent surface activity for oxygen exchange and bulk oxygen diffusivity in other applications such as solid oxide fuel cells, oxygen sensors and oxygen storage catalysts[13, 14, 15]. The combination of all these properties make a strong case for thermochemical water splitting based on the redox behavior of non-stoichiometric oxides. In particular, cerium oxide (CeO_2) is an excellent candidate, since it satisifies the aforementioned criteria[16, 17] and cerium (despite being classified a rare-earth element) is as earth abundant as copper - an

important economic advantage for scalability.

1.3 Thermochemical water splitting using $CeO_{2-\delta}$

Ceria, CeO_2, crystallizes in the cubic fluorite structure (Fig. 1.1), with the oxygen ions (O^{2-}) occupying the tetrahedral voids in the face centered cubic lattice of cerium ions (Ce^{4+}). Under reducing conditions, achieved either by heating the oxide and/or reducing the oxygen activity in the environment, a fraction of the oxygen atoms is released from the structure to equilibrate the chemical potential of oxygen in the gas and solid phase. This re-equilibration leads to creation of bulk oxygen vacancies, charge compensated by the conversion of twice as many Ce^{4+} to Ce^{3+}. In fact, at temperatures above 1000 °C, up to $\delta \approx 0.25$ can be generated within the cubic fluorite structure of $CeO_{2-\delta}$[18]. In a two step thermochemical cycle, schematically depicted

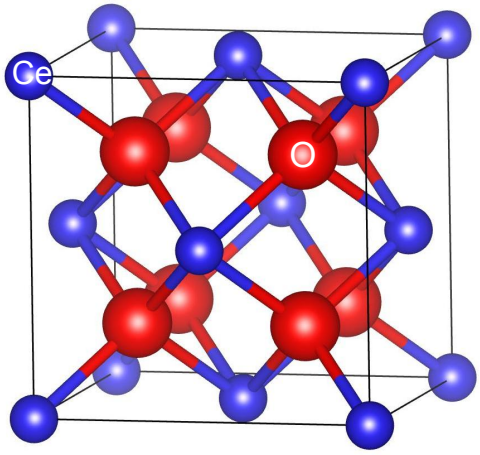

Figure 1.1: Cubic fluorite unit cell of stoichiometric ceria, CeO_2. The oxygen ions sit in the tetrahedral voids of a face centered cubic lattice of cerium ions.

in Fig. 1.2, ceria is first thermally reduced at 1500 °C or above in an inert atmosphere, followed by hydrolysis at 800 °C to liberate hydrogen,

$$CeO_{2-\delta_L} \xrightarrow{T_H} CeO_{2-\delta_H} + \frac{\delta_H - \delta_L}{2} O_2, \tag{1.1}$$

$$CeO_{2-\delta_H} + (\delta_H - \delta_L)H_2O \xrightarrow{T_L} CeO_{2-\delta_L} + (\delta_H - \delta_L)H_2. \tag{1.2}$$

δ_L and δ_H respectively denote the oxygen non-stoichiometry at the low temperture

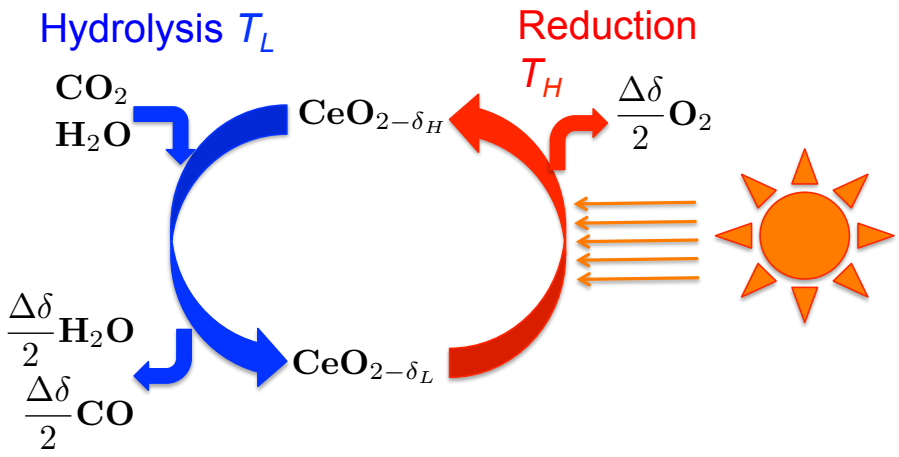

Figure 1.2: Illustration of a two step solar thermochemical cycle that uses non-stoichiometric ceria to split water and produce hydrogen. δ_L and δ_H respectively denote the oxygen non-stoichiometry at the low temperature (T_L) and high temperature (T_H) steps, and $\Delta\delta = \delta_H - \delta_L$

(T_L) and high temperature (T_H) steps, and δ_L is typically ~ 0. A similar reaction scheme can be constructed for dissociation of carbon dioxide (CO_2), which generates carbon monoxide (CO) at temperatures high enough to inhibit carbon formation. The process variables - temperature and oxygen partial pressure in the carrier gas - are chosen to maximize the fuel productivity and production rates. The feasibility of a ceria-based thermochemical process to split water has been demonstrated successfully[19, 20, 21, 22]. Fuel productivities of up to 11.8 ml hydrogen per gram of ceria at 6.2 ml per gram per minute have been achieved and a closed system efficiency analysis reveals that solar-to-fuel conversion efficiencies of up to 19% can be obtained even without solid state heat recovery[21].

1.4 Motivation and outline

Maximizing the solar-to-fuel conversion efficiency of a thermochemical cycle requires a multidisciplinary approach. From an engineering perspective, important considerations include efficient solar concentrators that can achieve the desired heat flux, reactor components capable of handling repeated thermal cycling and high temper-

atures, and minimization of heat losses. The "material specific properties" can be broadly classified into thermodynamic and kinetic. The fuel productivity per cycle is the important thermodynamic criterion, and is governed by the change in equilibrium non-stoichiometry between the reduction and hydrolysis steps, i.e. $\Delta\delta = \delta_H - \delta_L$. The non-stoichiometry, δ, is a function of the oxygen partial pressure, $p\mathrm{O}_2$, and temperature, T, and is related to the enthalpy and entropy of reduction. It contains all relevant information about the redox thermodynamics of the system and provides the basis for predicting the equilibrium gravimetric fuel productivity under a given choice of cycling conditions. The goal is to maximize the thermodynamic driving force (increase $\Delta\delta$) without compromising the rate of fuel production – the other important metric. Both the oxygen release and water dissociation steps require serial steps of (i) oxygen diffusion through the bulk of the solid, and (ii) surface reaction involving transport of oxygen across the gas-solid interface. The bulk diffusion of oxygen is quantified by the chemical diffusion coefficient, D_{Chem}, and the surface transport is quantified by the surface reaction rate constant, k_S. Unlike D_{Chem}, which is a material property and hence a function of the oxygen activity and temperature only, k_S also depends on the gas phase composition (not just $p\mathrm{O}_2$), surface morphology and surface composition. In principle, the fuel production curves from a thermochemical cycling experiment embody all the material specific parameters. However, the large driving forces (*i.e.* large changes in T and $p\mathrm{O}_2$), porous microstructures and poorly controlled gas flow dynamics convolve thermodynamic and kinetic effects, precluding a meaningful comparison of the kinetic properties of candidate materials. Experiments aimed at directly and quantitatively revealing the kinetic properties must use small perturbations from equilibrium to avoid non-linear effects, employ well-defined sample geometries, and present well-controlled gas flow dynamics.

A physical understanding of the redox thermodynamics and oxygen transport is essential to rationally guide the search for newer and better performing materials. This work explores state-of-the-art simulations - bridging the gap between quantum mechanical and statistical mechanical calculations - and electrochemical measurements to determine oxygen non-stoichiometry in undoped ceria. It also improves upon

an established experimental technique for measuring transport properties, to enable a systematic study of the effect of dopants on the behavior of ceria. In Chap. 2, ab initio calculations are integrated with lattice Monte Carlo simulations to predict, for the first time, the phase diagram and macroscopic thermodynamic properties such as reduction enthalpy and entropy of ceria as a function of non-stoichiometry and temperature and short range order parameters, entirely from first principles. In Chap. 3, the versatility of the electrical conductivity relaxation (ECR) technique to quantitatively extract the transport properties of an oxide is demonstrated, using 15 mol% Sm doped ceria as the reference material. A systematic data-analysis procedure was developed to reliably and uniquely determine the chemical diffusivity and/or surface reaction rate constants without making prior assumptions about the nature of the transport process (surface vs bulk vs co-limited). The experimental and data analytical methodologies were then used to study the effect of Zr doping on the eletrical conductivity and oxygen transport properties of ceria, the results of which are discussed in Chap. 4. In Chap. 5, the focus reverts back to thermodynamics. We demonstrate the capability to calculate the bulk non-stoichiometry of oxide thin films using electrochemical measurements. Cerium oxide was once again used as the benchmark material, since it displays both ideal and non-ideal thermodynamic behavior under different environmental conditions and is a well studied system in the literature. Aside from providing greater precision and resolution relative to conventional gravimetric methods of determing defect densities, electrochemical studies on well-defined sample geometries can yield interfacial thermodynamic properties as well. The appendix includes some recent results from ECR studies of ceria and Zr doped ceria at 1400 °C under both small driving forces and large driving forces representative of thermochemical cycling conditions. Each chapter is self contained, in that, the necessary background, theory and experimental details are first presented before discussing the results.

Chapter 2

Vacancy thermodynamics in ceria using first principles calculations

2.1 Why computational thermodynamics ?

Experimentation based science has been the norm for centuries. Existing tools have been constantly refined and newer, sophisticated ones have been developed to push the boundaries of what is measurable. Characterization of sub angstrom length scales and femtosecond timescales are within the realm of experiments today. On the other hand, computers are a relatively new addition to our repertoire of scientific tools. A key advantage of computer simulations is the absolute and precise control that the user possesses over the system variables. Everything starts out ideal unless made otherwise. Testing conditions which are impractical or hazardous to attempt in a lab can be safely obtained in a simulation. Borrowing Prof Cosma Shalizi's quote, "*no one gets wet in a simulated thunderstorm*". Also unique to simulations is the ability to isolate and selectively probe one of many mechanisms that could explain an experimental observation. For instance, the use of zinc phosphide as a low cost, high efficiency photovoltaic material has been limited by the difficulty in n-type doping it. While the synthesis and processing conditions can be varied in anticipation of a desired physical property, computer simulations are necessary to explain the atomistic mechanism linking the electronic structure and processing to the observed experimental result. In case of zinc phosphide, based on the formation energies of all

possible point defects computed using density functional theory, it was revealed that phosphorus interstitials are thermodynamically favored in the n-type regime, which act as electron sinks and nullify the intended doping effect[23].

Despite their many advantages, computational methods have largely served to validate or support experimental observations in place of predicting new properties or discovering new materials. This is because simulations rely on a physical model and to date, there is not a single model spanning all the length scales and time scales of known physical processes. One option is to resort to quantum mechanics and solve for the wave function of a system, using what are called first principles calculations. The all-electron wave function provides a complete description of the system and can be used to extract the thermodynamic properties across all length scales. Unfortunately, the computational cost of first principles calculations scale rapidly with the number of electrons in the system, and become prohibitively large beyond a few tens of unit cells even for modern supercomputers. Hence, any calculation aimed at investigating macroscopic properties of a system needs some abstractions to transition across the length scales while preserving the underlying physics of problem.

For non-stoichiometric ceria, the workhorse of this thesis, the thermodynamics of vacancies are of practical interest only at temperatures over 600 °C and low oxygen activities. As such, the DFT formalism is implemented at absolute zero, so any attempt to model entropic contributions (which favor defects) would need an abstraction to incorporate finite temperature effects. Further, experimentally measurable equilibrium properties such as entropy and enthalpy of reduction and non-stoichiometry at a given pO_2 are ensemble averages over a large number of configurations. Thus, a second level of abstraction is needed to include the configurational degrees of freedom. These abstractions have been proposed and initially implemented for metallic alloys, which are substantially simpler systems to model physically. Extending these methods to ceria and other such non-stoichiometric oxides pushes the boundaries of the computational thermodynamics approach and is the focus of this chapter.

2.2 Background

Significant research has been devoted to understanding the electronic structure of non-stoichiometric ceria from first principles using density functional theory (DFT)[24, 25] with the standard local density approximation (LDA) and generalized gradient approximation (GGA) exchange correlation functionals. It is well known that the 4f electrons in CeO_2 need to be treated as valence states to accurately reproduce the experimentally observed properties[26]. The use of conventional LDA and GGA exchange correlation functionals in ceria leads to self interaction error and failure to reproduce the insulating character of defect-free ceria. This necessitates adding a Hubbard potential (U) correction for the Ce 4f electrons to generate the experimentally observed band gap[27]. Hybrid functionals yield improvement in the electronic picture of ceria, but do not significantly change the energetics of vacancy formation[28]. The effects of transition and rare earth metal dopants[29, 30, 31]: both aliovalent[32, 33] and isovalent[34, 35] on oxygen vacancy formation have been investigated using a supercell approach. The oxygen storage capacity is correlated to the structural relaxation brought about by dopants with smaller ionic radius than Ce^{4+} and electrostatic effects. Activation energies for potential vacancy migration pathways have been computed from first principles[36, 37, 38] to understand the mechanisms of defect migration at atomistic scale. With the development of density functional perturbation theory, lattice dynamical properties, Born effective charges and phonon density of states have been calculated and these are found to agree well with experimental data[39, 40].

However, *ab initio* calculations are currently intractable for system sizes greater than a few hundred atoms. To obtain finite temperature bulk properties, it is necessary to move beyond the realm of DFT calculations to statistical thermodynamics of larger system sizes ($> 10^3$ atoms). While literature abounds with experimental investigations of the properties of ceria at high temperatures, the computational work described above has been primarily limited to studying the electronic structure and defect formation energies of ceria at absolute zero without attempting to obtain ther-

modynamic properties at higher temperatures, which is where its most interesting applications and properties emerge.

Our computational study aims to isolate and focus on the thermodynamics of intrinsic oxygen vacancies in ceria relevant to thermochemical cycling. While vacancies are central to the thermochemical cycling process, the thermodynamic driving force is governed by the change in δ (i.e. $\Delta\delta$) between T_H and T_L. For repeatability of the redox cycle, it is necessary to operate in the regime of single phase non-stoichiometric ceria. Furthermore, at such high values of δ, defect interactions become considerable and can negatively impact the entropic driving force for the reduction of ceria. Understanding the nature of vacancy interactions as a function of temperature and concentration in ceria will therefore be instrumental in motivating the exploration of dopants used to improve its suitability. Aside from its immediate relevance to thermochemical fuel production, we chose ceria as our model system since its phase diagram and vacancy thermodynamics are established experimentally. This would help test the accuracy of the computational thermodynamics approach to studying non-stoichiometric oxides, and extend it to screen dopants and predict the properties of doped ceria, for which literature is not as extensive.

Modeling of ceria presents a unique challenge: it requires the ability to capture electron-localization and associated electronic entropy effects. A step in this direction was made for the Li_xFePO_4 system[41] by showing that including electronic entropy via a cluster expansion approach yields a phase diagram whose topology is in qualitative agreement with experiments. We build upon this effort and seek to conclusively demonstrate the thermodynamic validity of such an approach, by verifying that the inclusion of both electronic and vibrational entropies results in excellent quantitative agreement with experiments for not only the phase diagram, but other thermodynamic quantities as well, such as the entropy of reduction and short-range order.

2.3 Methodology

The standard first principles approach to computing phase equilibria has been documented for alloys and solid solutions[42, 43, 44]. We present a brief overview here to highlight salient features of this approach relevant to non-stoichiometric oxides. Phase equilibria studies from first principles integrate both rigorous first principles calculations over selected small structures and large scale statistical ensemble based methods. The partition function, which contains all the thermodynamic information for a system, can be coarse grained over a hierarchy of degrees of freedom as described in Equation 2.1.

$$Z = \sum_{\sigma \in L} \sum_{\nu \in \sigma} \exp\left[-\beta E(\sigma, \nu)\right], \tag{2.1}$$

where ν,σ are respectively the vibrational and configurational states of the system constrained to a lattice L. Here, the configurational states include both genuine configuration variables (location of oxygen vacancies) and electronic state information (location of Ce^{3+} ions). The coarse graining takes advantage of the Born Oppenhiemer approximation to separate electronic and nuclear motion in the Hamiltonian. The energy $E(\sigma, \nu)$ is obtained by first computing the electronic ground state for a fixed composition in the lattice, followed by ionic relaxation (once the electrons are thermalized about fixed nuclear positions, they can be assumed to re-equilibrate instantaneously when the nucleii are perturbed). Vibrational frequencies of the system are then calculated for small displacements away from the relaxed ground state at 0 K. The cluster expansion then parametrizes this information in terms of larger structural units and enables estimation of energies of cells and compositions inaccessible through first principles calculations in a fast and efficient manner. Finally, the thermodynamic integration procedure, with the aid of Monte Carlo simulations, incorporates the effect of compositional fluctuations and temperature on the properties of the system and is used to derive other thermodynamic quantities.

2.3.1 First principles calculations

Electronic structure calculations were performed using the Vienna *ab initio* simulation package (VASP), a plane wave pseudopotential based DFT code[45]. GGA exchange correlation functional using the PAW (projector augmented wave) method[46] was employed. To correct for the strong on-site coulombic interaction of the Ce 4f electrons, we adopted the rotationally invariant GGA+U formalism introduced by Dudarev et al[47]. The Hubbard potential term 'U' penalizes partial occupancy of the f states and opens up a band gap. The value of U is typically set by fitting to experimentally established band gaps, or quantities such as lattice constant and bulk modulus. For non-stoichiometric ceria, based on previous LDA+U and GGA+U studies[25, 27] of oxygen vacancy formation energies and electron localization on Ce^{3+}, U=5 for GGA+U and U=6 for LDA+U have been proposed as optimal. Spin polarized GGA+U calculations in this work were all performed using U=5. Defect

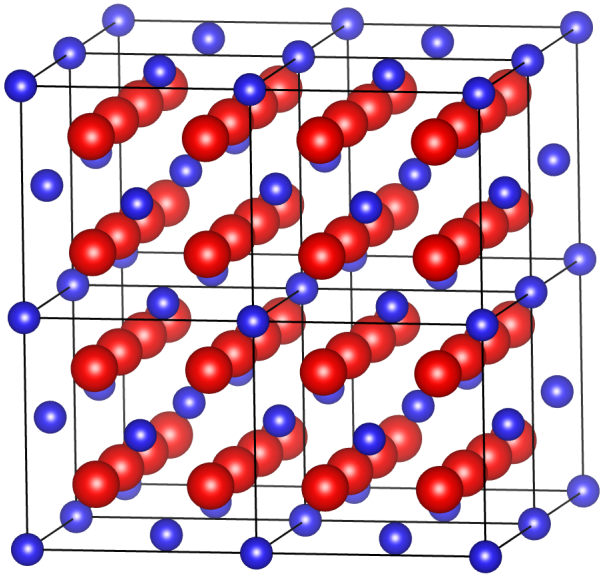

Figure 2.1: $2 \times 2 \times 2$ supercell of stoichiometric ceria.

calculations were performed on 2x2x2 supercells (Fig. 2.1) of ceria (96 atoms), using a 2x2x2 k-point grid. To sample structures with different vacancy content and configurations, the desired fraction of oxygen atoms were removed from a 96 atom supercell prior to the simulation. Fig. 2.2 shows a subset of the starting structures

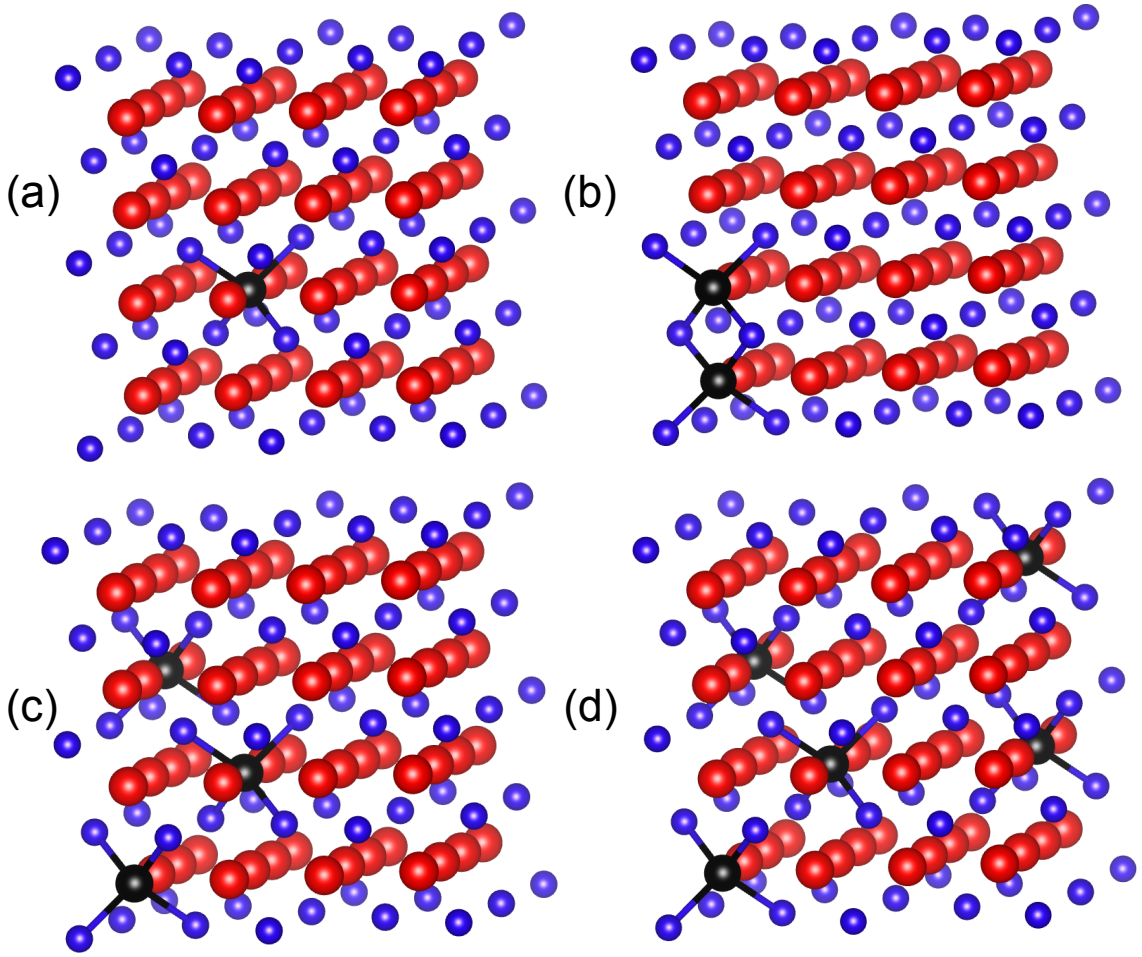

Figure 2.2: $2\times2\times2$ supercells of ceria with (a) 1 vacancy ($\delta = 0.0313$), (b) 2 vacancies ($\delta = 0.0625$), (c) 3 vacancies ($\delta = 0.0938$) and (d) 5 vacancies ($\delta = 0.1563$).

used for defect calculations. Electronic relaxations were performed until the total energy difference was less than 10^{-4} eV while ionic relaxations were carried out until residual forces less than 0.02 eV/ were achieved. Formation of vacancies in ceria leads to expansion of the lattice resulting from increased coulombic repulsion between the Ce^{4+} ions and larger ionic radius of Ce^{3+}. We account for this by performing multiple constant volume relaxations at distinct volumes for each structure. The energy benefit accrued from the volume relaxation is significant, and if overlooked, could lead to erroneous energies predicted with the cluster expansion later on. In all, 36 different configurations of vacancies were studied with compositions ranging from CeO_2 to $CeO_{1.75}$.

First principles lattice dynamics calculations were performed to incorporate vibrational effects on phase stability. We used the 'small displacement' finite differences method as implemented in VASP 5.2 to compute the Hessian matrix for the structures. Displacements of 0.015 away from the equilibrium relaxed positions were employed. For higher vacancy concentrations, we included structures with both pseudo-randomly dispersed and clustered arrangements to span the configurational dependence of the vibrational frequencies. The force constants output by VASP were used to obtain the dynamical matrix at other q-points and calculate out the phonon density of states (DOS) using Phonopy[48]. Gaussian smearing and an 8x8x8 q-point mesh were employed for the DOS calculation. The vibrational free energy (F_{Vib}) and entropy (S_{Vib}) were evaluated under the harmonic approximation as

$$\frac{F_{Vib}(T)}{N} = \frac{E^*}{N} + k_B T \int_0^\infty \ln\left(2\sinh\left(\frac{h\nu}{2k_B T}\right)\right) g(\nu) d\nu, \tag{2.2}$$

$$\frac{S_{Vib}(T)}{N} = \left(\frac{\partial F_{Vib}/N}{\partial T}\right)_V, \tag{2.3}$$

where N is the total number of atoms in the system, ν is the frequency of the phonon mode, g(ν) is the phonon density of states.

2.3.2 Cluster expansion : configurational degrees of freedom

The cluster expansion (CE) Hamiltonian treats configurational disorder by decomposing the energy of a lattice into a basis of clusters (points, pairs, triplets etc.) of lattice sites. Each cluster is a polynomial in occupation variables and has an associated effective cluster interaction (ECI), 'J' in Eq. 2.4. The ECIs are obtained by fitting to the database of *ab initio* energies:

$$E(\sigma) = J_0 + \sum_i J_i \sigma_i + \sum_{i \neq j} J_{ij} \sigma_i \sigma_j + ... \tag{2.4}$$

Vacancies are treated as independent species, so any site in the anion sub-lattice can be occupied by an oxygen ion or vacancy. Additionally, we explicitly treat charge state

disorder in the cation sub-lattice resulting from Ce^{4+}/Ce^{3+} (configurational electronic entropy). In order to describe the energetics of this system with two interacting sub-lattices, we use a multicomponent multilattice CE formalism[49, 50] that works in the product basis of cluster functions defined on each sublattice. Despite the presence of four distinct species (O, Vac, Ce^{3+}, Ce^{4+}), constraints of site and charge balance ($2[Ce^{3+}] = [Vac]$) render the system essentially pseudo-binary. Our cluster expansion fit was obtained using the mmaps code in the alloy theoretic automated toolkit (ATAT)[44, 51].

The knowledge of ECIs provides a computationally inexpensive and efficient means to compute the energy of a large system on the fly during Monte Carlo simulations, circumventing the need for time consuming *ab initio* calculations. As such, the CE fit to *ab initio* energies is independent of temperature. By cluster expanding phonon free energies in the basis of clusters fit to configurational energies, the ECIs, and consequently the MC data, can be made to include vibrational effects.

2.3.3 Lattice Monte Carlo simulations : thermodynamic properties

The fundamental external variables of interest to the thermochemical cycling of ceria are temperature (T) and oxygen partial pressure (p_{O_2}). Its properties are strongly dependent on the oxygen nonstoichiometry, which is uniquely set for a given (T, p_{O_2}). Thus, ceria lends itself to be conveniently studied by semi-grand canonical Monte Carlo simulations, treating temperature and chemical potential as external variables. A semi-grand canonical ensemble fixes the total number of lattice sites, letting the concentration of individual species fluctuate in response to an an applied temperature or chemical potential change. Consideration of macroscopic charge-neutrality leaves us with one independent chemical potential μ written as :

$$\mu = (\mu_{Vac} - \mu_{O^{2-}}) + 2(\mu_{Ce^{3+}} - \mu_{Ce^{4+}}), \tag{2.5}$$

where $\mu_{Vac}, \mu_{O^{2-}}, \mu_{Ce^{3+}}$ and $\mu_{Ce^{4+}}$ denote the chemical potentials of the individual species which are externally imposed. μ can be described as the free energy cost associated with swapping a pair of Ce^{4+} and O^{2-} with a pair of Ce^{3+} and Vac.

The Grand Potential $\Phi(\mu, T)$ with respect to a reference can be obtained by thermodynamic integration along a fixed T or fixed μ path:

$$\Phi(T_0, \mu) = \Phi(T_0, \mu_0) - \int_{\mu_0}^{\mu} \langle N(T_0, \mu) \rangle \, d\mu, \tag{2.6}$$

$$\frac{\Phi(T, \mu_0)}{k_B T} = \frac{\Phi(T_0, \mu_0)}{k_B T_0} + \int_{T_0}^{T} (\langle E(T, \mu_0) \rangle - \mu \langle N(T, \mu_0) \rangle) d\beta. \tag{2.7}$$

$\langle E \rangle$ is the thermodynamically averaged energy, $\langle N \rangle$ is the thermodynamically averaged concentration, μ_0 and T_0 are the reference chemical potential and temperature, and $\beta = 1/k_B T$. The low temperature and high temperature expansions used to obtain the reference points for integration are not central to this paper and can be found elsewhere[52]. Our MC runs were performed on 5184 atom cells (larger sizes were attempted and found to not affect the results) using the memc2 code from ATAT[49]. Temperature steps of 40 K were used for the MC runs, with 2000 equilibrium passes and 1000 averaging passes at each (T, p_{O_2}). Simultaneous spin flips were used to maintain charge balance and were constrained to occur within two unit cell distances of each other.

It should be noted that the constraint of charge balance alone is not sufficient to guarantee that the system will never undergo a phase separation into multiple spurious ground states that are locally non-charge balanced although the overall simulation cell is. This can occur when the cluster expansion is only fitted to charge-balanced structures, thus providing little guarantee that the extrapolated energy of non-charge-balanced structures is physically meaningful. We avoided this problem by an iterative procedure. Starting with a cluster expansion fitted to charge-balanced structures only, we monitored the simulation for evidence of phase separation into non-charge-balanced structures. Whenever this was observed, the energy of the structure was calculated from first principles and included in the cluster expansion to reduce extrap-

olation errors from the fit. Since *ab initio* calculations imposing periodic boundary conditions necessarily enforce charge-neutrality, we used a neutralizing background charge to estimate the energy of non-charge-balanced structures. This ansatz is justified whenever the resulting calculated energies are sufficiently high, so that these configurations are very rarely sampled in equilibrium.

2.4 Results and discussion

2.4.1 First principles calculations

Using GGA+U calculations, the equilibrium lattice constant for stoichiometric ceria was found to be 5.48. The formation of an oxygen vacancy in a 2x2x2 supercell is accompanied by the localization of two electrons onto the 4f states of two Ce atoms with anti-symmetric spins. True ground state convergence in other vacancy structures was tested by assigning different starting spin configurations to the Ce atoms (up or down spin, and their locations) and looking for the lowest energy structure. The 2p-5d and 2p-4f energy gaps were 5.3 eV and 2.5 eV respectively. The formation energy for an oxygen vacancy in a 2x2x2 supercell was calculated to be 3.2 eV, agreeing with previous GGA+U studies[24]. We included up to eight vacancies in a 2x2x2 supercell (corresponding to $CeO_{1.75}$) in different configurations. Such defect concentrations, while high, have been shown to exist in ceria under appropriate (T, p_{O_2}) and are of interest to us. The lattice expansion associated with vacancy formation was evaluated through multiple constant volume relaxations of each configuration and found to be around 2% for $CeO_{1.75}$ (eight vacancies in a 2x2x2 supercell). The formation energies (per mole of gaseous oxygen), E^f_{vac}, of all the structures relative to the defect-free supercell are plotted in Fig. 2.3. E^f_{vac} is defined as

$$E^f_{\mathrm{vac}}(\delta) = 2\left(\frac{E_{\mathrm{CeO_{2-\delta}}} - E_{\mathrm{CeO_2}}}{\delta}\right) + E_{\mathrm{O_2}}, \tag{2.8}$$

where $E_{\mathrm{CeO_{2-\delta}}}$ and $E_{\mathrm{CeO_2}}$ are the ground state energies of supercells with and without vacancies respectively, and $E_{\mathrm{O_2}}$ is the energy of a molecule of gaseous oxygen at stan-

dard state. The convex hull (solid black line) connects the ground state configurations at each composition.

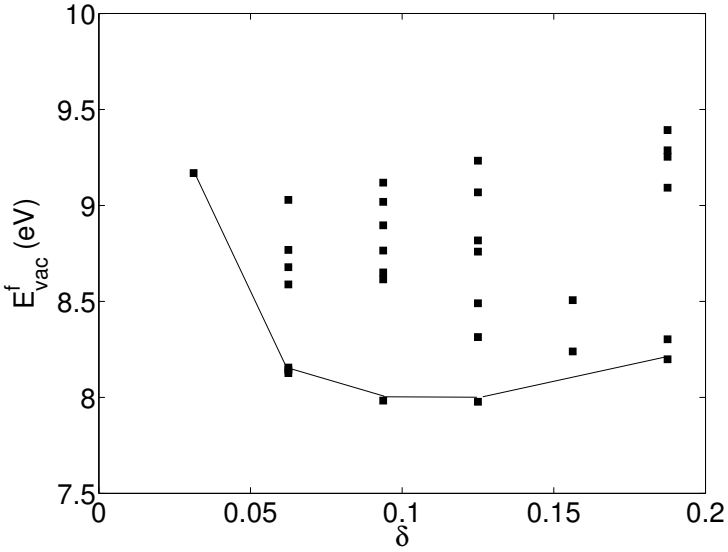

Figure 2.3: Plot of formation energies of various defect structures as defined in Eq. 2.8. The line connecting the ground states at each composition is the convex hull.

Phonon density of states computed under the harmonic approximation are plotted in Fig. 2.4. Vacancies are clearly stabilized by vibrations as evidenced by the softening of modes in $CeO_{1.91}$ (three vacancies in a 2x2x2 supercell) compared to CeO_2. Further, for a given concentration, clustered vacancies had stiffer phonon modes than vacancies dispersed over the supercell.

2.4.2 Cluster expansion

The optimal cluster expansion fit to the calculated *ab initio* energies (CE 1) of the 36 relaxed geometries comprised 13 pair and 1 triplet clusters apart from the null and 2 point clusters. Considering that ceria is an ionic compound, it is important to ascertain if the long range electrostatic interactions are adequately described by a short-range cluster expansion. To ascertain this, we fit another cluster expansion (CE 2) to the *ab initio* energies after subtracting out the coulombic energy term (computed through an Ewald summation). The latter was then cluster expanded in

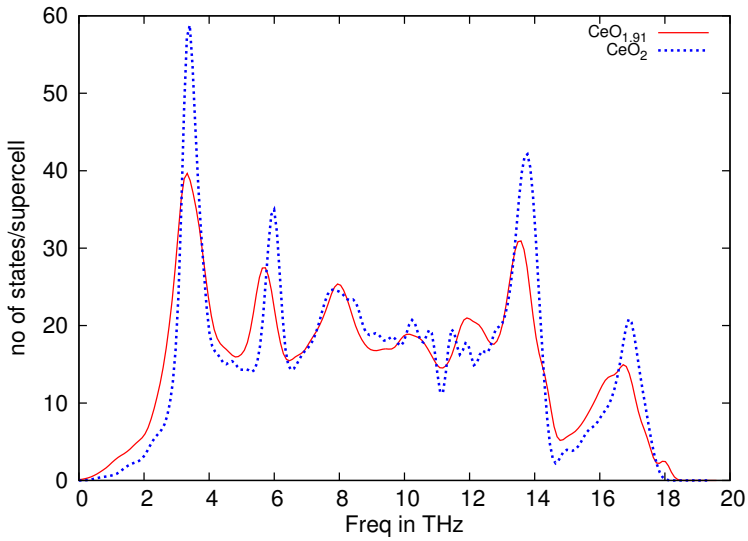

Figure 2.4: Phonon density of states from first principles calculated under the harmonic approximation. Oxygen vacancies lead to softening of vibrational modes in $CeO_{1.91}$ (three vacancies in a 2x2x2 supercell) compared to CeO_2.

the basis of clusters identified by the fit, and added as an energetic correction to the ECIs. The results are illustrated by Fig. 2.5. The pair and triplet cluster ECIs of CE 2 show identical decay characteristics with cluster diameter as CE 1, indicating that electrostatic interactions are captured well by the cluster expansion. The cross-validation score[44], which provides a measure of the predictive power of a cluster expansion fit, was close to 0.003 eV for both CE 1 and CE 2. In view of these results, we justify using CE 1 for further work, given its higher computational efficiency.

The effect of temperature on ECIs was incorporated by cluster expanding the vibrational free energies in the basis of clusters of CE 1. This introduced a temperature dependent correction to 7 clusters (determined via cross-validation) out of a total of 17.

2.4.3 Monte Carlo simulations

The Ce-O phase diagram in the composition range of Ce_2O_3 - CeO_2 has been determined by experiments. The low temperature portion of the phase diagram is complicated by the many vacancy ordered phases of composition Ce_nO_{2n-m}, and is

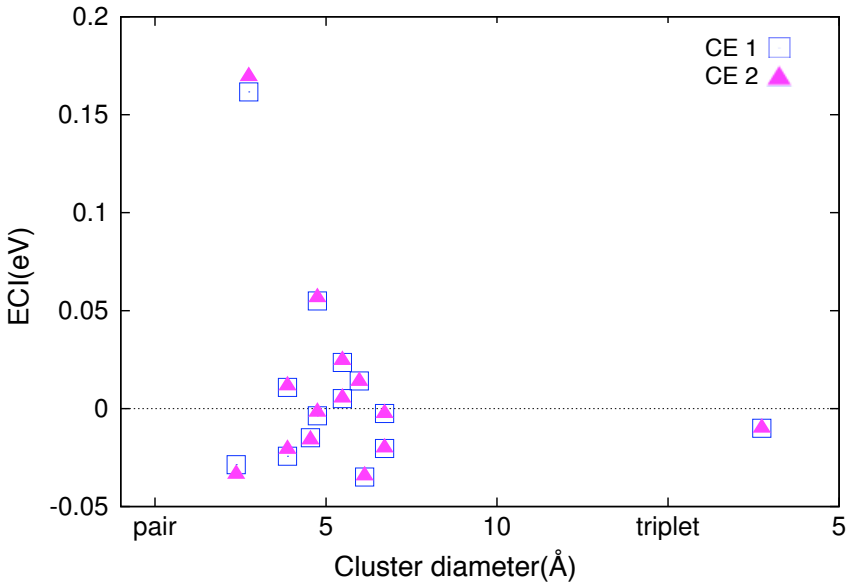

Figure 2.5: ECI vs cluster diameter for a cluster expansion fit to the as-scalculated first principles energies (squares, CE 1). Subtracting the electrostatic energy prior to fitting and later adding it back (as an energetic correction) does not change the variation of ECIs with cluster diameter (filled triangles, CE 2). This indicates that the electrostatic interactions are captured by the cluster expansion and do not need an explicit treatment.

not of primary concern to this work. Of interest to us is the high temperature phase diagram and the ability of first principles calculations to predict the miscibility gap and vacancy thermodynamics in single phase non-stoichiometric ceria.

A temperature-composition plot along a constant μ trajectory starting from 0 K is shown in Fig. 2.6. Defect free CeO_2, the starting ground state (GS), is stable up to 1300°C before oxygen vacancies start to form. With the inclusion of vibrational effects, the onset of vacancies happens at a much lower temperature of 900°C, all other variables being the same. Most *ab initio* phase diagram studies have in the past neglected the non-configurational contributions to defect formation entropy, and these can substantially affect phase stability.

In order to accurately predict the miscibility gap, it is necessary to perform simulations from two different starting points for each μ – a heating simulation from the low temperature ordered ground state, and a cooling simulation from the high tem-

perature disordered phase. At a given temperature, the discontinuity in concentration when the grand potentials from the two runs are equated leads to the miscibility gap. The phase diagram in the composition range of $CeO_{1.8}$ to CeO_2 obtained using this approach is shown in Fig. 2.7. A miscibility gap shows up even in the absence of vibrations, but the temperature scale is off by nearly a factor of two compared to experiments. The solubility limit of vacancies in ceria is underestimated and the miscibility gap is shown to persist up to temperatures as high as 1500°C. The temperature dependent cluster expansion provides a closer agreement : the miscibility gap closes at 800°C (690°C in experiments) and single phase ceria is shown to be stable at higher oxygen nonstoichiometry at any given temperature.

The cluster expansion technique was principally intended to model configurational disorder in alloys in which interatomic interactions tend to be much simpler than in insulators or semiconductors. Studies have however expanded its domain of applications to describe the energetics of Li intercalation in battery materials and model charge state disorder through a localized electronic entropy term[41], equilibrium composition profile across interfaces of doped ceria superlattices[53]. This is the first study of the high temperature phase diagram of ceria from first principles. That it captures the thermodynamics and detects a miscibility gap in a correlated electron system is in itself a significant result; the quantitative agreement with experiment upon including the effect of vibrations and electronic entropy shows even more promise.

The phase diagram helps identify thermodynamically stable phases at equilibrium, but even in the region of single phase non-stoichiometric ceria, significant short range order can persist leading to deviation of bulk thermodynamic properties from that of an ideal solution. Indeed, this is the case and ceria deviates from an ideal solution model for δ values as low as 0.007. It is characterized experimentally by studying the dependence of nonstoichiometry (or a dependent property thereof, such as electrical conductivity) on the partial pressure of oxygen. It can also be studied by extracting the nonstoichiometry dependence of entropy change associated with vacancy formation. Momentarily disregarding the entropy of gaseous oxygen released upon vacancy formation, the entropy change for the solid phase can be directly eval-

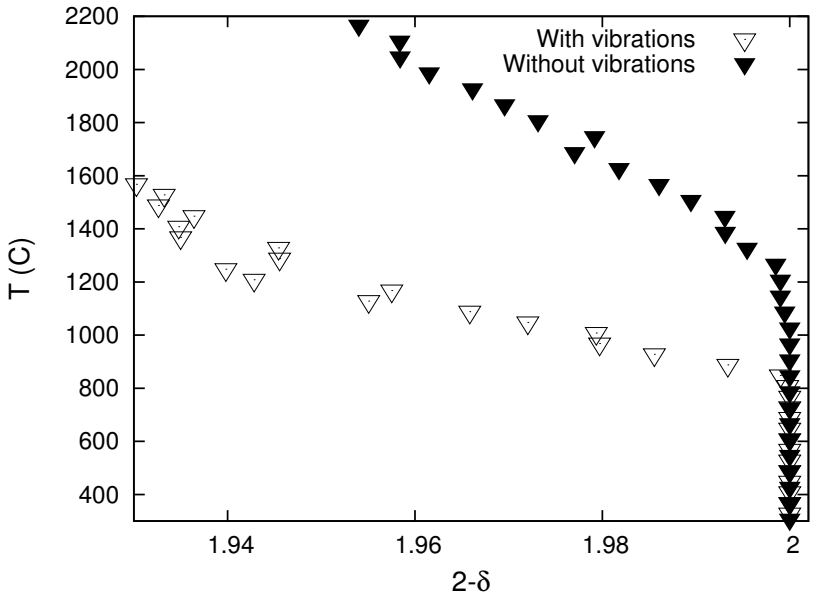

Figure 2.6: A constant μ trajectory MC simulation starting from the low temperature ground state (CeO_2) illustrating vibrational effects on the phase diagram and vacancy concentrations.

uated by converting the grand canonical output of MC simulations into canonical quantities:

$$\langle S\rangle = \frac{1}{T}(\langle E\rangle - \Phi - \sum_i \mu_i \langle n_i\rangle). \tag{2.9}$$

We fit a model which includes ideal configurational entropy with a polynomial correction term (to account for non-ideal behavior) to S(δ) evaluated per site.

$$\begin{aligned} S_{Solid}(\delta) = A\Bigg[2\left(\frac{\delta}{2}\right)\ln\left(\frac{\delta}{2}\right) + 2\left(1-\frac{\delta}{2}\right)\ln\left(1-\frac{\delta}{2}\right) \\ + (2\delta)\ln(2\delta) + (1-2\delta)\ln(1-2\delta)\Bigg] \\ + B\delta^3 + C\delta^2 + D\delta + E, \end{aligned} \tag{2.10}$$

where δ is the non-stoichiometry and A,B,C,D and E are constants (for a given T). The solid state entropy $S_{Solid}(\delta)$ per site referenced to $S_{Solid}(\delta = 0)$ is plotted in Fig. 2.8 for T=1480 K. The ideal solution entropy (the term whose coefficient is A) peaks at $\delta = 0.25$, but the actual entropy of the system plateaus much sooner. The pronounced deviation from ideal solution behavior is apparent from δ values as low

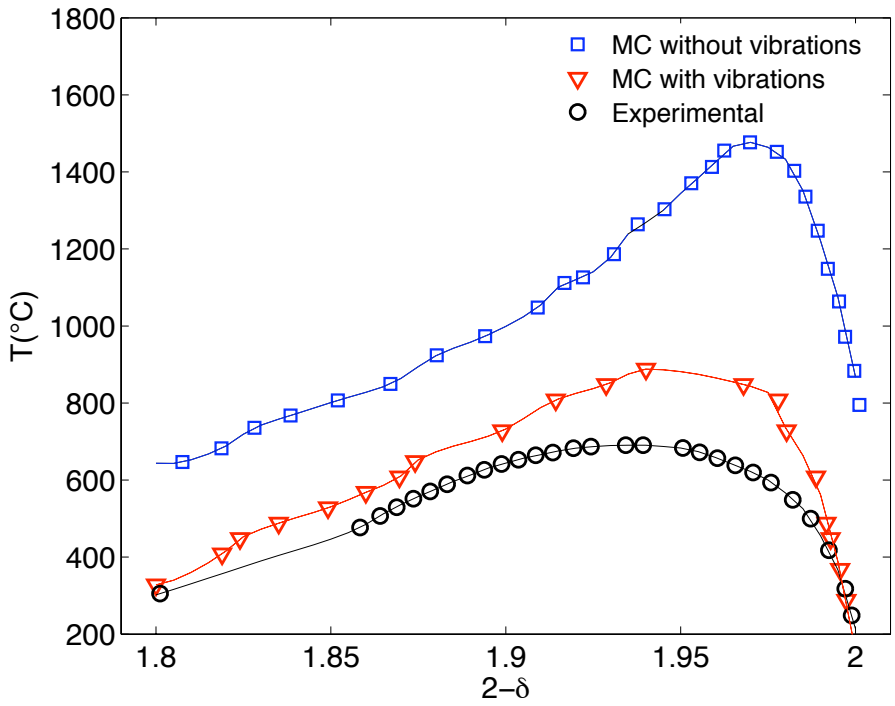

Figure 2.7: (Color online) Miscibility gap in ceria calculated from Monte Carlo simulations. The pronounced effect of vibrations is visible from the suppression of the miscibility gap to lower temperatures and enhanced vacancy solubility in non-stoichiometric ceria. The experimental phase diagram[18] has been overlaid for comparison.

as 0.01. Vibrations clearly increase the entropic advantage to having vacancies, but the strongly non ideal character persists. To compare with experimental work[1], we computed the entropy of reduction associated with forming an oxygen vacancy in the limit of infinitesimal change in nonstoichiometry.

$$\lim_{\Delta\delta\to 0} \frac{1}{\Delta\delta}\mathrm{CeO}_{2-\delta} \longrightarrow \frac{1}{\Delta\delta}\mathrm{CeO}_{2-(\delta+\Delta\delta)} + \frac{1}{2}\mathrm{O}_2 \tag{2.11}$$

$$\Delta S_{Total}(\delta) = \Delta S_{Solid}(\delta) + 0.5 * S_{O_2}(\delta) \tag{2.12}$$

$$S_{O_2}(T) = S^0_{O_2}(T, 1\ atm) - k_B \ln\left[\frac{p_{O_2}}{1\ atm}\right] \tag{2.13}$$

$$\Delta S_{Solid}(\delta) = \frac{1}{\Delta\delta}(S_{CeO_{2-\delta}} - S_{CeO_{2-\delta-\Delta\delta}}) \tag{2.14}$$

The solid state entropy is readily available from MC simulations. However, there are

difficulties associated with calculating entropy of gaseous oxygen from first principles, mainly concerned with the definition of a reference state. This can be resolved by using the standard state entropy data for molecular oxygen from thermochemical tables[54]. p_{O_2} can be obtained using Eq. 2.15:

$$\mu_O(T) = \mu_O^0(T) + k_B T \ln\left[\frac{p_{O_2}}{1\ atm}\right] \tag{2.15}$$

While the chemical potentials of the respective species from MC simulations are guaranteed to yield the right equilibrium composition and free energies, they are arbitrarily displaced from their true values by an additive constant. This prevents a straightforward application of Equation 2.15. As a workaround, we used the experimentally published nonstoichiometry vs $\ln(p_{O_2})$ data[1] to fit the chemical potential from MC and obtain the offset. $\Delta S_{Total}(\delta)$ computed using this approach at 1480 K is illustrated in Fig. 2.9. The strong deviation from ideal solution model suggests that

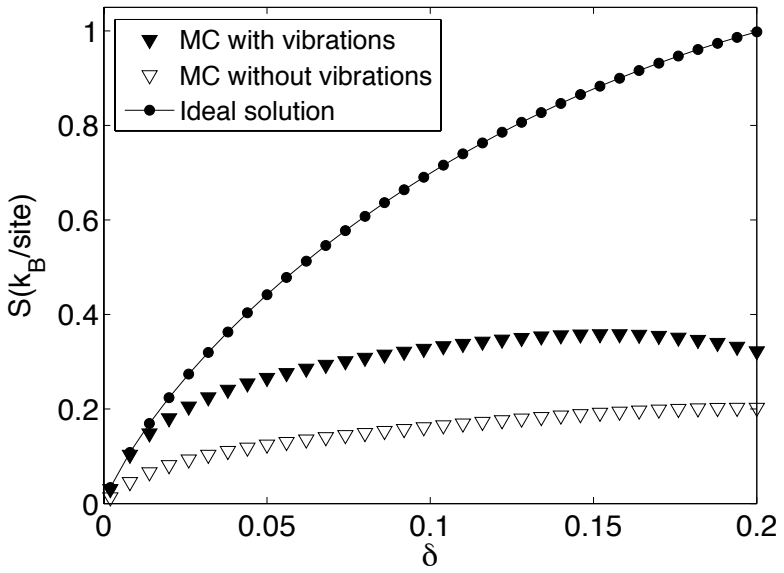

Figure 2.8: Entropy of $CeO_{2-\delta}$ referenced to CeO_2 computed from MC simulations at 1480 K. The deviation from ideal solution behavior (configurational disorder in Ce^{3+}/Ce^{4+} and O^{2-}/Vac lattice) becomes apparent even at low δ. Vibrations provide entropic benefit to forming vacancies, but the marked non-ideal behavior prevails.

the entropic benefit from vacancies is being offset by some kind of defect interactions.

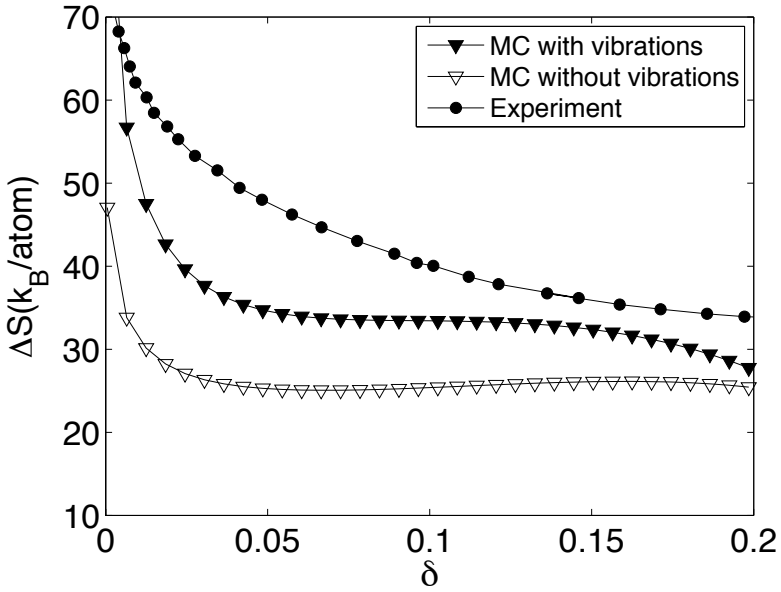

Figure 2.9: Entropy change associated with forming an oxygen vacancy (see Eqn. 2.11) as a function of nonstoichiometry compared with experiment[1].

These defect interactions could arise from stable defect complexes or vacancy ordering over short length scales. We look to characterize and quantify the short range order (SRO) by calculating the thermally averaged pair correlations for the pair clusters in real space. Formally, this idea is embodied in the Warren-Cowley parameters:

$$\alpha_{lmn}(\delta) = \frac{\langle \sigma_{000}\sigma_{lmn}\rangle - \langle \sigma_{000}\rangle^2}{1 - \langle \sigma_{000}\rangle^2}, \tag{2.16}$$

$$\langle \sigma_{000}\sigma_{lmn}\rangle = \sum_{\sigma} P(\sigma, T)\frac{1}{N}\sum_{i}\sigma_i\sigma_{i+(lmn)}. \tag{2.17}$$

For a pair {(0,0,0), (l,m,n)} in the O^{2-}/Vac sub-lattice with vacancy site fraction 's', $\hat{\sigma}_i$ is the occupation variable for site i averaged over all sites equivalent by symmetry, $\langle \hat{\sigma}_{000}\rangle^2 = (1-2s)^2$ is the MC average of the point cluster correlation and $\langle \hat{\sigma}_{000}\hat{\sigma}_{lmn}\rangle$ is the averaged correlation function of the pair cluster. P(σ,T) is the probability of configuration σ, given by

$$P(\sigma, T) = \frac{1}{Z(\{\mu_i\}, T)}\exp\left[-\beta\left(E(\sigma) - \sum_i \mu_i x_i\right)\right], \tag{2.18}$$

where $Z(\{\mu_i\}, T)$ is the semi-grand canonical partition function and $\{\mu_i\}$ is the set of chemical potentials. If vacancies behave ideally (non interacting, randomly distributed), then $\langle \hat{\sigma}_{000}\hat{\sigma}_{lmn}\rangle = \langle \hat{\sigma}_{000}\rangle \langle \hat{\sigma}_{lmn}\rangle = (1-2s)^2$ and $\alpha_{lmn}(\delta) = 0$ for any δ. Clustering of like species is given by $\alpha_{lmn} > 0$ and likewise ordering of unlike species is given by $\alpha_{lmn} < 0$.

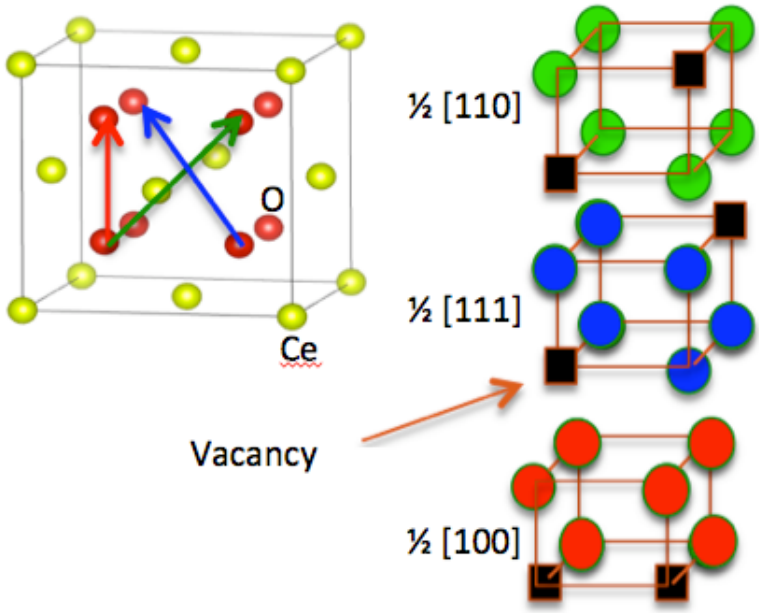

Figure 2.10: Different vacancy pairs in the anion sub-lattice of a unit cell of ceria. Black boxes denote vacancies. The color scheme for the oxygen atoms corresponds with that used for plotting SRO parameters of various vacancy pairs in Fig. 2.11.

Fig. 2.10 shows three vacancy pairs in the anion sublattice of a unit cell of ceria. There are 2 distinct 1/2[111] clusters, one within the unit cell and another extending out of the unit cell, with a face centered Ce atom halfway in between. Tab. 2.1 summarizes the coordinates and diameters of the five smallest pair clusters in the anion sublattice. In Fig. 2.11a, $\alpha(\delta)$ at 1320 K for the five clusters in Table 2.1 are plotted. Close to stoichiometry, $\alpha_{lmn} = 0$ for all (lmn), as would be expected for non interacting vacancies. However, deviations from zero become apparent even for slightly off-stoichiometric compositions. In particular, there is strong preference for vacancies to align along 1/2[110]. The negative correlation along 1/2[100] indicates that two vacancies are not thermodynamically favored at nearest neighbor sites. The

Table 2.1: Cluster type, coordinates and diameter of the first five pair clusters in the anion sublattice of ceria. There are two distinct 1/2[111] clusters, one within the unit cell (superscript 'a') and another extending out of the unit cell, with a face centered Ce atom halfway in between (superscript 'b').

Cluster type	Sites (fractional coordinates)	Diameter(Å)
1/2[100]	(0.25,0.25,0.25) (0.25,0.25,0.75)	2.74
1/2[110]	(0.25,0.25,0.25) (-0.25,0.25,0.75)	3.87
$1/2[111]^a$	(0.75,0.75,0.75) (0.25,0.25,1.25)	4.75
$1/2[111]^b$	(0.75,0.75,0.75) (0.25,0.25,0.25)	4.75
[100]	(0.75,0.75,0.75) (-0.25,0.75,0.75)	5.48

two distinct 1/2[111] pairs have nearly the same value of $\alpha > 0$ and hence are possible directions for short range clustering of vacancies. The effect of temperature is to favor disorder (Fig. 2.11b for WC parameters at 1791 K), as can be seen from the fact that $\alpha_{lmn} \approx 0$ up to larger nonstoichiometry. At still higher concentrations of vacancies, the α_{lmn} start to deviate from zero and show similar clustering/ordering tendencies along the respective directions.

There are multiple related material properties associated with vacancy formation in ceria, hence no one rule can govern the choice of dopants. While ease of vacancy formation is crucial, it is the change in nonstoichiometry between the high and low temperature steps (Eqn. 1.1) that ultimately establishes the oxygen uptake and consequently the amount of hydrogen produced. An important implication of this study is that point defect interactions markedly diminish the entropic driving force for thermochemical cycling of ceria. Doping strategies that help screen vacancies from 'seeing' each other would inhibit short range ordering/clustering, but it is important to recognize that this introduces redox inactive species in the system, which might affect the thermodynamic efficiency. The power of the electronic structure calculations lies in the ability to explore interactions at an atomistic level, which, when integrated with

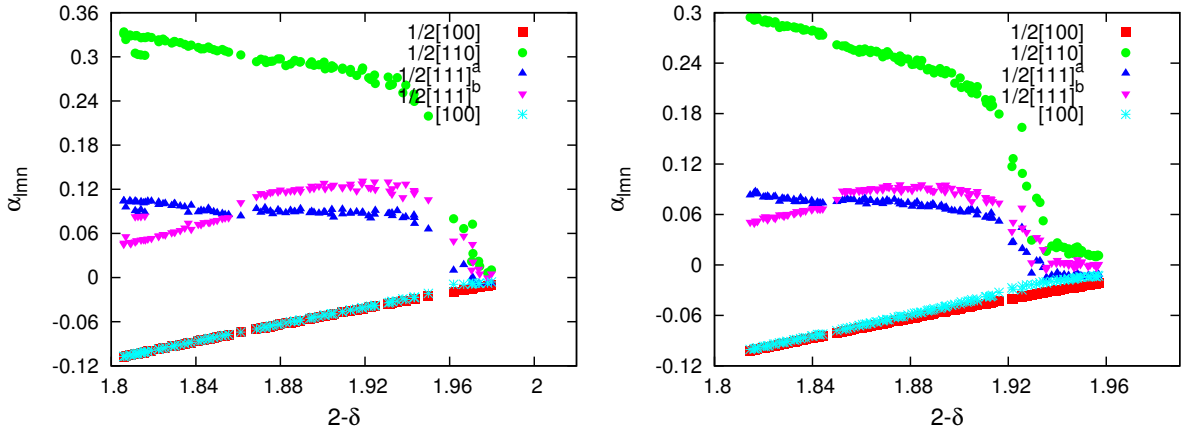

Figure 2.11: Warren-Cowley short range order parameters (α_{lmn}) as a function of nonstoichiometry for various pair clusters in the O^{2-}/Vac sublattice at (a) 1262 K and (b) 1791 K. Of note is a strong clustering tendency along 1/2[110].

larger scale Monte Carlo calculations, can explain how electronic structure manifests in the behavior of macroscopic properties such as reduction enthalpy and entropy, electrical conductivity and so on. Also, the cluster expansion formalism is best suited for the study and characterization of defect associates[55, 56], which are often used to explain deviations in the non-stoichiometry behavior (and the dependent properties thereof) from that of an ideal solution of point defects.

2.5 Conclusions

We successfully employed a cluster expansion Hamiltonian based lattice Monte Carlo simulations approach to quantitatively compute the high temperature thermodynamics of oxygen vacancies in ceria from first principles. The ground state energy and electronic structure of non-stoichiometric ceria were obtained from GGA+U supercell calculations. The database of structures and energies was used to fit a coupled cluster expansion that explicitly accounts for charge state disorder (Ce^{3+}/Ce^{4+}). Lattice vibrational free energies were calculated from first principles under the harmonic approximation and found to favor formation of vacancies. Vibrational effects were incorporated as a temperature correction to the effective cluster interactions. The phase diagram obtained from lattice Monte Carlo simulations was found to exhibit

a miscibility gap. The inclusion of vibrations resulted in quantitative corrections to the composition and temperature range of the miscibility gap, yielding excellent agreement with experiments. The solid state entropy change resulting from vacancy formation was evaluated and the deviation from ideal solution behavior illustrated through composition dependence of entropy. To further quantify the defect interactions leading to deviations from ideality, Warren Cowley short range order parameters were computed. It was found that there is a strong preference for vacancies to cluster along 1/2[110] and 1/2[111] directions, while the nearest neighbor 1/2[100] sites exhibited ordering behavior. While temperature does disorder the structure, the vacancy clustering behavior was shown to persist at temperatures as high as 1780 K.

Chapter 3

An electrical conductivity relaxation study of oxygen transport in samarium doped ceria

3.1 Introduction

The remarkable capacity of ceria to display significant oxygen nonstoichiometry (δ) at high temperatures or low oxygen activity without changing its crystal structure is essential to many of its applications in solid state electrochemistry. Beyond its widespread use as a solid-oxide fuel-cell electrolyte when doped with trivalent elements such as samarium or gadolinium, nonstoichiometric ceria ($CeO_{2-\delta}$) has recently emerged as a candidate reaction medium to facilitate two-step solar thermochemical splitting of water and/or carbon dioxide to generate hydrogen or other fuels[19, 57, 21, 22, 58]. The first of the two steps is a high temperature endothermic reaction involving bulk release of oxygen. The second step, typically performed at a lower temperature, is the oxidation of the reduced ceria by the reactant gases (H_2O and/or CO_2) that returns the oxide to a low value of oxygen nonstoichiometry.

Whereas thermodynamics governs the theoretically achievable fuel productivity from this pair of reactions, that is, the fuel produced per cycle, the rate at which fuel is produced, the other critical metric, is a function of kinetics. Two serial steps are involved: diffusion of neutral oxygen species within the bulk of the oxide, quantified in terms of the chemical diffusion coefficient D_{Chem}, and reaction at the surface of

the oxide, quantified in terms of the surface reaction rate constant k_S. In principle, D_{Chem} and k_S are embodied in the time evolution of oxygen release or fuel production in a thermochemical experiment. In practice, however, the large driving forces (*i.e.* large changes in T and $p\mathrm{O}_2$), the random porous microstructure of the materials commonly employed, and the poorly controlled gas flow dynamics of typical thermochemical reactors preclude access to these terms and impede meaningful comparisons of the kinetic responses of candidate materials. In contrast to fuel production studies, experiments aimed at directly and quantitatively revealing kinetic properties must use small perturbations from equilibrium to avoid complex, non-linear effects, must employ well-defined sample geometries, and must present well-controlled gas flow dynamics.

A variety of techniques have been employed in combination with experimental configurations that meet the above requirements for measuring D_{Chem} and k_S. These include secondary ion mass spectrometry (SIMS) to analyze isotope depth profiles[59], gravimetry relaxation[60, 61], electrochemical impedance spectroscopy[62] and electrical conductivity relaxation[63, 64, 65]. The objective of the present work is to demonstrate the versatility of this last method, electrical conductivity relaxation (ECR), to study the effect of temperature and gas atmosphere on D_{Chem} and k_S.

In a relaxation experiment, one analyzes transient behavior in the re-equilibration process following a step change in the $p\mathrm{O}_2$ of the surrounding gas. The relaxation profile, typically that of sample mass or electrical conductivity, is described by a solution to Fick's second law that takes into account the appropriate boundary conditions. A fit to the data yields values for the desired material parameters. The conductivity relaxation method is particularly attractive because of the ease with which electrical conductivity can be measured and with which reactors with small volumes, as required for rapid exchange of gases, can be constructed. The long history of the ECR method, having been practiced as early as 1934 by Dünwald and Wagner[66], renders the technique, in some sense, a 'classic' tool. Furthermore, in some quarters, the level of sophistication in its application has yielded highly compelling results[65]. In many other instances, however, the experimental and numerical requirements for the suc-

cess of the method are not fully appreciated. Indeed, it has been recently suggested that a simultaneous determination of D_{Chem} and k_S is inherently unreliable[67].

In the present study we have performed ECR measurements on bulk samples of $Sm_{0.15}Ce_{0.85}O_{1.925-\delta}$ (samaria doped ceria, SDC15) to extract both D_{Chem} and k_S with the dual objectives of demonstrating the conditions under which both parameters can be reliably determined and providing new insights into this technologically important oxide. SDC15 is an ideal material against which to validate the experimental and analytical methodologies because the bulk transport properties are well-known and, though to a lesser degree of certainty, the surface properties are also known[62]. In addition, despite significant interest in SDC, surprisingly, comprehensive studies of its surface reactivity remain to be reported. Reports to date have either encompassed a limited range of oxygen partial pressures[60] or have focused on phenomena such as the influence of bulk grain boundaries[68], thin-film thickness effects[69], or the role of metal/oxide interfaces[70], each under a narrow range of conditions.

This chapter is organized as follows. Section 3.2 will briefly review the relevant theory for relaxation experiments and oxygen transport, followed by a brief analysis of anticipated results based on literature measurements of D_{Chem} and k_S in SDC15. In Section 3.3, the experimental details will be presented, followed by our data analysis procedure and its test results. We will then discuss our results with SDC15 in Section 3.4 before concluding with Section 3.5.

3.2 Theory

3.2.1 Electrical conductivity relaxation

A detailed formulation of the diffusion model underlying the ECR method and its numerical analysis can be found in the literature[71, 72, 73]. For completeness, we provide a brief theoretical background and highlight pertinent equations along with the key assumptions.

The sample geometry employed here is that of an infinite sheet of thickness '$2a$'

along the direction, x, of oxygen transport. In response to the step change in gas phase oxygen partial pressure, the oxygen concentration varies with x and with time, t. The conductivity, taken to be directly proportional to the oxygen concentration, is measured along a direction normal to that of oxygen transport. Solving Fick's second law of diffusion in 1D under the assumption that the surface reaction is first order in concentration with rate constant k_S, *i.e.*

$$J(\pm a) = \mp k_S(c_V(\pm a, t) - c_V(\pm a, \infty)), \tag{3.1}$$

results in the following concentration profile[74]:

$$\frac{c_V(x,t) - c_V(0)}{c_V(\infty) - c_V(0)} = 1 - \sum_{m=1}^{\infty} \frac{2\tilde{L}\cos(\alpha_m x/a)}{(\alpha_m^2 + \tilde{L}^2 + \tilde{L})\cos(\alpha_m)} \exp\left(-\frac{\alpha_m^2 D_{Chem} t}{a^2}\right) \tag{3.2}$$

where $c_V(\pm a, t)$ and $c_V(\pm a, \infty)$ are, respectively, the instantaneous and final volumetric concentrations of vacancies at the sample surface, and $\{\alpha_m\}$ is the set of positive roots of

$$\alpha_m tan(\alpha_m) = \tilde{L} = \frac{a k_S}{D_{Chem}}, \tag{3.3}$$

where $\tilde{L}$ is a dimensionless length that reflects the relative roles of surface reaction and bulk diffusion in the overall relaxation rate. Under the assumption of a total conductivity that varies linearly with concentration (valid when step changes in oxygen partial pressure are sufficiently small) the spatially averaged, normalized conductivity obtained from the measurement is

$$\frac{\sigma(t) - \sigma(0)}{\sigma(\infty) - \sigma(0)} = 1 - \sum_{m=1}^{\infty} \frac{2\tilde{L}^2}{\alpha_m^2(\alpha_m^2 + \tilde{L}^2 + \tilde{L})} \exp\left(-\frac{\alpha_m^2 D_{Chem} t}{a^2}\right) \tag{3.4}$$

where, $\sigma(0)$ and $\sigma(\infty)$ are, respectively, the initial and final equilibrated conductivities of the sample.

The form of the dimensionless conductivity is simplified under conditions in which only one process dominates. When the surface reaction step is much slower than bulk

diffusion, *i.e.*, $k_S \ll D_{Chem}/a$ and $\tilde{L} \ll 1$, Equation 3.3 becomes

$$\tilde{L} = \alpha_1 \tan(\alpha_1) \approx \alpha_1^2 \tag{3.5}$$

with

$$\alpha_m \approx m\pi \text{ (m} \geq 2) \tag{3.6}$$

This causes all but the first exponential in Equation 3.4 to reduce to zero, such that

$$\frac{\sigma(t) - \sigma(0)}{\sigma(\infty) - \sigma(0)} = 1 - \exp\left(\frac{k_S t}{a}\right). \tag{3.7}$$

At the other extreme of bulk diffusion limited transport, *i.e.*, $k_S \gg D_{Chem}/a$ and thus $\tilde{L} \gg 1$, the roots to Equation 3.3 are

$$\alpha_m = \frac{(2m-1)\pi}{2}, \tag{3.8}$$

and Equation 3.4 becomes

$$\frac{\sigma(t) - \sigma(0)}{\sigma(\infty) - \sigma(0)} = 1 - \frac{64}{\pi^2} \sum_{m=1}^{\infty} \frac{1}{(2m-1)^2} \exp\left(-\frac{(2m-1)^2 \pi^2 D_{Chem} t}{4a^2}\right). \tag{3.9}$$

The challenges associated with attempting to fit Equation 3.4 to experimental data so as to determine the kinetic parameters have been addressed by many authors[65, 73, 75]. Because $\tilde{L}$ is not known *a priori*, any one of Equations 3.4, 3.7 or 3.9 could potentially describe the relaxation profile. This necessitates a data analysis procedure that can reliably extract the parameters without under or over fitting.

Experimentally, success of the ECR method requires that several conditions be met. First, there must be no open porosity (which would allow gas phase access to the interior and greatly speed the relaxation process) and minimal closed porosity (which would slightly retard the process by limiting bulk diffusion). Second, the reactor flush time (t_0) must be much smaller than the material response time (τ), where τ is $\approx a/k_S$ in the surface reaction limited regime and $\approx a^2/4D_{Chem}$ in the diffusion

limited regime. Third, the grain sizes must be large (on the order of microns) so as to minimize grain boundary contributions to the measured electrical resistance and also to eliminate possibilities of a grain-boundary mediated relaxation process. The latter, while certainly of significant scientific interest, would render Equation 3.4 inapplicable. Finally, the step changes must be made small to validate the assumption of first order surface reaction kinetics and constant D_{Chem} and k_S between the initial and final $p\mathrm{O}_2$ values. This also guarantees that the magnitude of the thermodynamic driving force is the same regardless of the direction of $p\mathrm{O}_2$ change and justifies the assumption that conductivity varies linearly with oxygen content. Exactly how small the step change must be depends on the details of the system under investigation and has been discussed at length by Jacobson and co-workers[76]. In the present study, $\Delta \ln(p\mathrm{O}_2)$ was restricted to a value of < 0.5, and the sufficiency of this choice was evaluated by comparing results for the forward and backward step changes.

A fourth requirement, specific to the geometry described here, is that the width $2a$ of the sample along the direction of interest must be much smaller than those of the other two directions to justify the 1D solution. In principle, solutions that treat the 2D and 3D cases are available[74], and even in these cases only two free parameters are obtained from the fit. In practice, however, ensuring that a global minimum is obtained is much more challenging. In this work some measurements were carried out using samples that, in fact, necessitated analysis according to the 2-D solution, as discussed at the end of Section 3.3.2.

3.2.2 Defect chemistry and conductivity of SDC15

The defect chemical origins of $p\mathrm{O}_2$-dependent conductivity in rare-earth doped ceria are well established[17] and are briefly reviewed here for completeness. When the dopant concentration is high relative to the intrinsic defect concentrations, global electroneutrality reduces to

$$[\mathrm{Sm}'_{\mathrm{Ce}}] = 2[\mathrm{V}_{\mathrm{O}}^{\bullet\bullet}] \tag{3.10}$$

where Kröger-Vink notation[77] has been employed, and $[\mathrm{Sm}'_{\mathrm{Ce}}]$ and $[\mathrm{V}^{\bullet\bullet}_{\mathrm{O}}]$ are, respectively, the fractional dopant and oxygen vacancy concentrations. Despite an approximately fixed vacancy concentration, the mobile electron concentration in ceria varies with oxygen chemical potential, *i.e.*, $p\mathrm{O}_2$, as a result of the reduction reaction.

$$\mathrm{O}^{\mathrm{x}}_{\mathrm{O}} \longleftrightarrow \frac{1}{2}\mathrm{O}_2(g) + \mathrm{V}^{\bullet\bullet}_{\mathrm{O}} + 2e' \tag{3.11}$$

with an equilibrium constant $K_R(T)$,

$$K_R(T) \approx [\mathrm{V}^{\bullet\bullet}_{\mathrm{O}}]n^2 p\mathrm{O}_2^{1/2} \approx 1/2[\mathrm{Sm}'_{\mathrm{Ce}}]n^2 p\mathrm{O}_2^{1/2} \tag{3.12}$$

where n represents the fractional concentration of mobile electrons and describes equally well the Ce^{3+} concentration. In addition, thermal excitation generates electrons (equivalently, Ce^{3+}) and holes (equivalently, O^-) from Ce^{4+} and O^{2-} species [78], the concentrations of which can be expected to obey the relationship

$$np = K_{np}(T) \tag{3.13}$$

These expressions, in combination with the much higher mobility of electronic defects than ionic defects, give rise in principle to a $p\mathrm{O}_2$-dependent conductivity of the form

$$\sigma_{tot} = \sigma_n + \sigma_{ion} + \sigma_p = \sigma_n^0 p\mathrm{O}_2^{-1/4} + \sigma_{ion} + \sigma_p^0 p\mathrm{O}_2^{1/4} \tag{3.14}$$

where σ_n^0 and σ_p^0 are constants that depend on the dopant concentration, the reduction equilibrium constant, the electronic defect equilibrium constant and the respective electronic defect mobilities. This relationship implies a double-logarithmic plot of σ_{tot} vs $p\mathrm{O}_2$ will display a flat region, reflecting the electrolytic domain, which is flanked by regions at low and high $p\mathrm{O}_2$ with slopes of -1/4 and 1/4, respectively, corresponding to the n-type and p-type regimes.

Numerous experimental measurements of total conductivity have revealed the existence of the electrolytic and ideal n-type domains in doped ceria[79, 62]. In contrast,

the p-type conductivity, which is generally lower than the n-type conductivity over accessible pO_2 ranges due to the much lower concentration of holes, has been reported only on the basis of partial conductivity measurements[80, 81, 82]. The question naturally arises, then, whether the variation in conductivity under oxidizing conditions ($pO_2 > 10^{-5}$ atm) is sufficient to permit a meaningful ECR measurement. Based on the p-type conductivity measured by Xiong *et al.*[81] for SDC20 at 800 °C and the ionic conductivity of SDC20 reported by Yahiro *et al.*[83] at the same temperature, one can estimate that the relative change in conductivity on changing the gas atmosphere from 1 to 0.1 atm pO_2 will be on the order of 0.3% (with an absolute conductivity on the order of 0.032 S/cm). Achieving sensitivity at this level, though requiring care, is not prohibitive. Accordingly, and because the surface reaction properties of doped ceria under oxidizing conditions are as important for thermochemical cycling as are the properties under reducing conditions, measurements were made under a wide pO_2 range, including the oxidizing regime.

3.2.3 Chemical diffusion coefficient

When both ions and electrons are mobile in an oxide, the chemical diffusion coefficient (also referred to as the ambipolar diffusion coefficient) relates the flux of neutral oxygen to the oxygen chemical potential gradient. D_{Chem} can be derived by simplifying the fundamental transport equations governing ion and electron transport in the presence of a chemical and an electrical potential gradient (Nernst - Planck equation). For 1D transport, it has the form

$$\begin{aligned} J_{ion}^{charge}(x) &= -\sigma_{ion}(x)\left(\frac{1}{z_{ion}e}\nabla\mu_{ion}(x) + \nabla\phi(x)\right) \\ J_{eon}^{charge}(x) &= -\sigma_{eon}(x)\left(\frac{1}{z_{ion}e}\nabla\mu_{eon}(x) + \nabla\phi(x)\right) \end{aligned} \tag{3.15}$$

where x is the position, J is the flux, σ is the conductivity, ze is the charge, μ is the chemical potential, ϕ is the internal electrical potential and subscripts *eon* and *ion* denote electronic and ionic species. In the absence of an externally applied electrical

potential gradient, the net charge flux must be zero, i.e.,

$$J_{ion}^{charge}(x) + J_{eon}^{charge}(x) = 0 \tag{3.16}$$

Combining Eqs. 3.15 and 3.16, we get

$$J_{ion}^{charge}(x) = -\frac{\sigma_{ion}(x)\sigma_{eon}(x)}{\sigma_{ion}(x) + \sigma_{eon}(x)} \left[\frac{1}{z_{ion}e} \nabla \mu_{ion}(x) - \frac{1}{z_{eon}e} \nabla \mu_{eon}(x) \right] \tag{3.17}$$

Noting that concentration changes and flux of oxygen vacancies must be balanced by that of neutral oxygen, i.e

$$\frac{1}{z_{ion}e} J_{ion}^{mass}(x) + J_{O}^{mass} = 0 \tag{3.18}$$

$$dc_{ion}(x) + dc_{O}(x) = 0 \tag{3.19}$$

and expressing $\nabla \mu(x)$ in terms of $\nabla c(x)$, Eq. 3.17 becomes

$$J_{O}^{mass}(x) = -\frac{1}{e^2} \frac{\sigma_{ion}(x)\sigma_{eon}(x)}{\sigma_{ion}(x) + \sigma_{eon}(x)} \left[\frac{1}{z_{ion}^2} \frac{\partial \mu_{ion}(x)}{\partial c_{ion}(x)} + \frac{1}{z_{eon}^2} \frac{\partial \mu_{eon}(x)}{\partial c_{eon}(x)} \right] \nabla c_{ion}(x) \tag{3.20}$$

For ceria, $z_{ion} = 2$, $z_{eon} = -1$, $dc_O = -dc_{ion} = -dc_{eon}/2$ and the chemical potential of neutral oxygen is related to that of vacancies and electrons by $\mu_O = -\mu_{ion} - 2\mu_{eon}$. Using these relations and considering small driving forces such that the position dependence of material parameters can be dropped, Eq. 3.20 becomes

$$J_{O}^{mass} = -\left[\frac{1}{4e^2} \frac{\sigma_{ion}\sigma_{eon}}{\sigma_{ion} + \sigma_{eon}} \frac{\partial \mu_O}{\partial c_O} \right] \frac{\partial c_O(x)}{\partial x} \tag{3.21}$$

The constant of proportionality between the concentration gradient and flux,

$$D_{Chem} = \frac{1}{4e^2} \frac{\sigma_{ion}\sigma_{eon}}{\sigma_{ion} + \sigma_{eon}} \left[\frac{\partial \mu_O}{\partial c_O} \right] \tag{3.22}$$

is called the ambipolar or chemical diffusion coefficient of oxygen. The term in square brackets is a thermodynamic factor that relates chemical potential changes in the

surrounding gas atmosphere to concentration changes within the oxide. It describes an important influence of thermodynamics - the relative ease of reducing the oxide - on D_{Chem}.

In the dilute limit, the relation $\mu_i = \mu_i^0 + RT \ln c_i$, can be used in Eq. 3.20 to express D_{Chem} as a function of the ionic conductivity, σ_{ion}, the electronic conductivity, σ_e, and the corresponding volumetric defect concentrations, c_{ion} and c_e:

$$D_{Chem} = \frac{RT}{4F^2} \frac{\sigma_{ion}\sigma_e}{\sigma_{ion} + \sigma_e} \left[\frac{1}{c_{ion}} + \frac{4}{c_e} \right], \tag{3.23}$$

where F and R are Faraday's constant and the universal gas constant, respectively. In a material such as SDC15, oxygen vacancies are unquestionably the relevant ionic defects ($c_{ion} = c_V$), whereas under conditions of negligible hole conductivity, the electronic defects of relevance are the mobile electrons ($\sigma_e = \sigma_n$ and $c_e = c_n$). Thus, with knowledge of the conductivities and concentrations of these two types of carriers, the ambipolar diffusion coefficient can be computed.

As already discussed in the context of the defect chemistry, conductivity is often directly measured, and for SDC15 both σ_{ion} and σ_n are readily available in the literature as functions of temperature and, in the latter case, of $p\mathrm{O}_2$ as well. The remaining unknowns, the defect concentrations, are obtained by noting that, within the electroneutrality regime defined by Equation 3.10, the vacancy concentration is, by definition, fixed by the dopant concentration. The electron concentration is implied by Equation 3.12, which on rearrangement and combination with Equation 3.10, becomes[17]

$$n = \left(\frac{2K_R(T)}{[\mathrm{Sm}'_{\mathrm{Ce}}]} \right)^{1/2} p\mathrm{O}_2^{-1/4} \tag{3.24}$$

The equilibrium reduction constant for SDC15 has been reported in the literature, and the individual thermodynamic terms, the entropy, ΔS_O, and enthalpy, ΔH_O, of reduction, which give K_R according to

$$K_R(T) = \exp\left(\frac{\Delta S_O}{k_B} \right) \exp\left(\frac{-\Delta H_O}{k_B T} \right) \tag{3.25}$$

are available[62]. Thus, using literature values for σ_{ion}, σ_n, ΔH_O, ΔS_O, and the molar volume to convert from fractional to volumetric defect concentrations, it is possible to compute D_{Chem}, against which experimental results for D_{Chem} can be compared. Indeed, directly measured values of D_{Chem} have generally shown good agreement with those computed according to Equation 3.23[61].

3.2.4 Surface reaction rate constant

Turning to surface transport across the gas-solid interface, in the diffusion model used to fit ECR profiles, the surface reaction rate constant, k_S , is a phenomenological quantity introduced in the boundary condition. It is a first order rate constant relating the surface flux to the concentration difference between the instantaneous and thermally equilibrated values,

$$J(t) = k_S(c_O(t) - c_O(\infty)) \tag{3.26}$$

However, in a relaxation experiment, the flux of oxygen is driven by the chemical potential gradient, i.e.

$$J_t = k'_S(\mu_O(t) - \mu_O(\infty)) \tag{3.27}$$

Comparing Eqs. 3.26 and 3.27, we have the relation

$$k_S = k'_S \frac{\partial \mu_O}{\partial c_O} \tag{3.28}$$

Thus, much like the chemical diffusion coefficient, D_{Chem} the surface reaction rate constant, k_S obtained through ECR incorporates the thermodynamic factor(Eq. 3.22) to relate the chemical potential gradient to concentration gradient[84, 85].

The surface reaction rate constant in doped ceria has been evaluated in the literature, not only using relaxation methods[61, 60], but also using A.C. impedance spectroscopy (ACIS)[62] and oxygen isotope exchange measurements[61, 86]. In an impedance measurement, one typically obtains an area-normalized electrode resistance term, $\rho_{electrode}$, often referred to simply as the 'area-specific-resistance' or ASR.

For a surface active oxide (in contrast to one that is electrochemically active only at the triple phase boundaries formed between the oxide, metal and gas phase) this resistance implies a surface reaction constant defined according to [62]

$$k_S = \frac{k_B T}{(ze)^2 \rho_{electrode} c_V}, \tag{3.29}$$

where e is the elementary charge, z is the valence of the species (2 for oxygen vacancies) and k_B is Boltzmann's constant. Formally, the vacancy concentration in Equation 3.29 is that at the surface, but in the absence of detailed knowledge of the surface characteristics, c_V can be 'reasonably' approximated by the bulk value[87]. Furthermore, because of the equivalence between charge and mass transport across the interface, this electrochemically determined reaction constant is identical to the surface reaction constant obtained from ECR measurements[88]. In light of the many methods available for determining the surface reaction constant, it is not surprising then that there are several experimental reports[59, 60, 62] against which the values measured here can be compared.

In addition to method validation, approximate values of D_{Chem} and k_S from the literature permit a preliminary identification of the rate-limiting step for a given sample thickness. Specifically, the critical thickness, $L_c = D_{Chem}/k_S$, delineates the surface and bulk limited regimes in that samples with $a < L_c$ are largely surface reaction limited and conversely those with $a > L_c$ are largely bulk diffusion limited[74]. For 10-20 mol % rare-earth doped ceria, reported D_{Chem} values range from 2×10^{-5} to 1×10^{-4} cm^2/s at temperatures from 750 to 850 °C and oxygen partial pressures from 10^{-24} atm to 10^{-3} atm. Typical values of k_S from ECR and impedance measurements under similar conditions are on the order of 5×10^{-6} cm/s to 1×10^{-5} cm/s[60, 62]. Taking $D_{Chem} \approx 1 \times 10^{-5}$ cm^2/s and $k_S \approx 1 \times 10^{-5}$ cm/s yields $L_c \approx 1$ cm. Thus, a typical sample of thickness 0.8 mm as used in these experiments can be expected to be well within the surface-reaction-limited regime.

3.3 Experimental and analytical procedure

3.3.1 Experimental methods

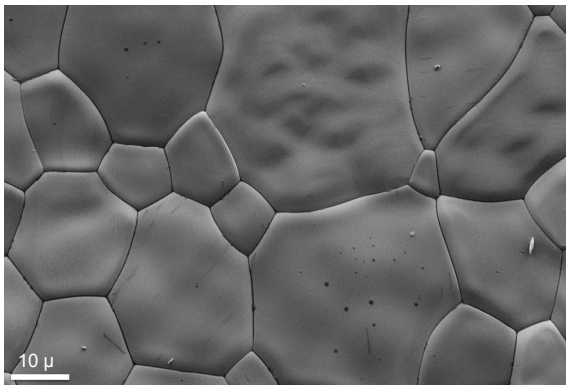

Figure 3.1: Scanning electron micrograph of a sintered SDC15 pellet (unpolished) showing average grain size of 3 microns and minimal porosity.

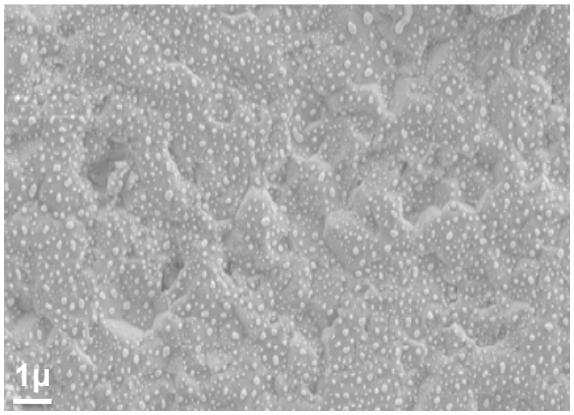

Figure 3.2: Scanning electron micrograph showing isolated but well dispersed Pt catalyst particles sputtered on an SDC15 sample and annealed at 950 °C for an hour. The average particle size was close to 100 nm, with an interparticle spacing of 400 nm.

Polycrystalline compacts of SDC15 were prepared from commercial powders of the target composition $Ce_{0.85}Sm_{0.15}O_{1.925}$ (Fuel Cell Materials Inc., Lot #247-085, surface area=8 m^2/g). The powder was subjected to uni-axial pressing at 160 MPa, cold isostatic pressing at 300 MPa, followed by sintering at 1500 °C for 8 h under stagnant air. Resulting samples had densities $> 95\%$ of theoretical values and mean grain sizes of $\sim$3 microns, Figure 3.1. Dimensions were typically 25 $\times$ 5.5$\times$ (0.2-

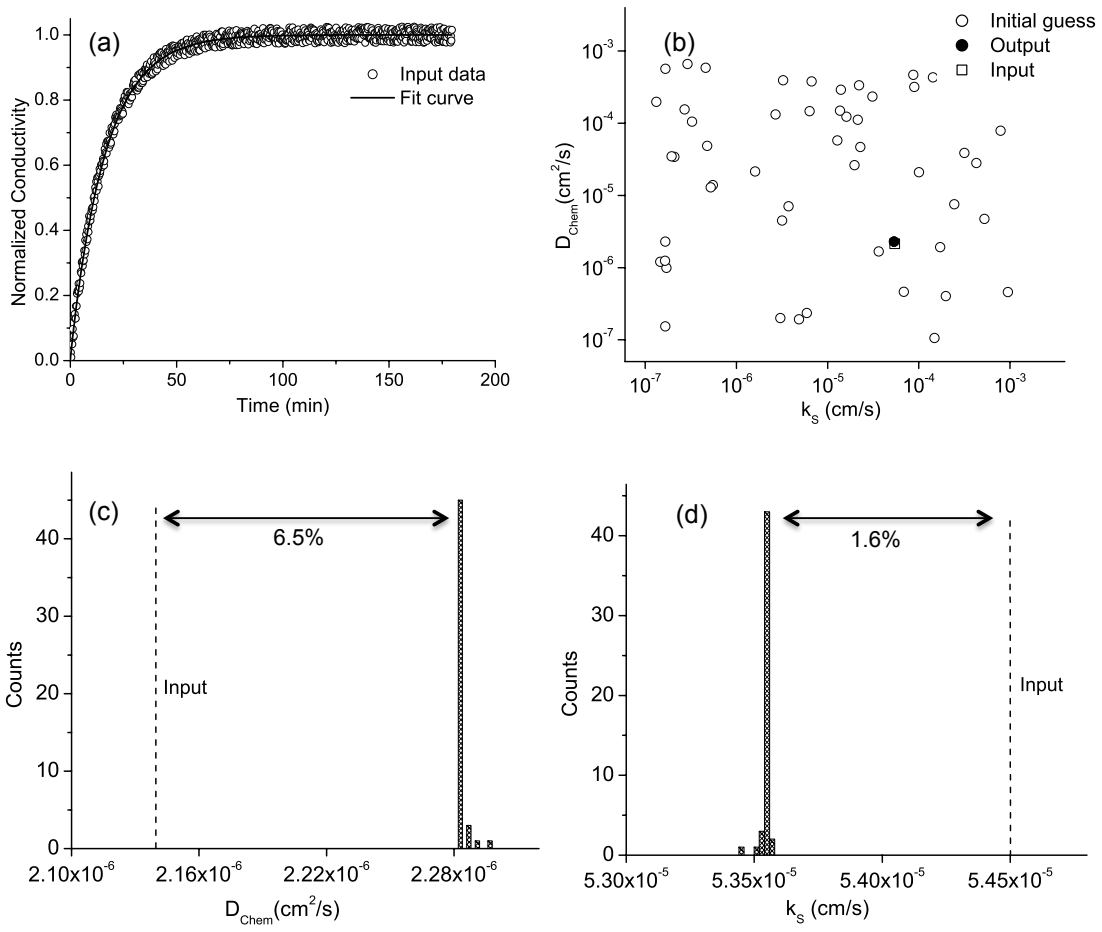

Figure 3.3: Illustration of procedures employed to extract D_{Chem} and k_S from ECR data. (a) Fit to relaxation data generated using $D_{Chem} = 2.14 \times 10^{-6}$ cm^2/s, $k_S = 5.45 \times 10^{-5}$ cm/s and sample thickness = 0.1 cm. (b) A map of D_{Chem}, k_S used as initial guess values (open circles) and the output optimized set of values (closed circles). (c) Histogram of D_{Chem} and (d) k_S showing the respective mode values, 2.28×10^{-6} cm^2/s and 5.36×10^{-5} cm/s, agree well with the input values used to generate the dataset.

2)mm^3. In order to ensure reproducibility of the surface characteristics, samples were polished to a final roughness of 3 μm. The composition of the polished samples was confirmed by electron probe microanalysis (EPMA) (JEOL JXA-8200, carbon coated samples, $CePO_4$ and $SmPO_4$ used as reference standards). Measurements at three different positions on a representative sample yielded absolute CeO_2 and Sm_2O_3 molar contents of 83.6% $\pm$ 0.7% and 15.3% $\pm$ 0.9% respectively.

Table 3.1: Representative results from testing the data analysis routine on datasets generated with known values of sample thickness ($2a$ = 0.1 cm), chemical diffusion coefficient (D_{Chem} cm^2/s) and surface reaction rate constant (k_S cm/s). Superscript 'only' indicates fits performed using the relevant one-parameter model.

Input			Output				
$\tilde{L}$	k_S	D_{Chem}	$\tilde{L}$	k_S	D_{Chem}	k_S^{only}	D_{Chem}^{only}
0.01	1.15×10^{-5}	4.14×10^{-5}	0.34	1.27×10^{-5}	1.49×10^{-6}	1.16×10^{-5}	1.60×10^{-7}
0.11	1.15×10^{-5}	4.14×10^{-6}	0.35	1.24×10^{-5}	1.38×10^{-6}	1.10×10^{-5}	1.57×10^{-7}
1.02	5.45×10^{-5}	2.14×10^{-6}	0.94	5.36×10^{-5}	2.28×10^{-6}	4.10×10^{-5}	5.70×10^{-7}
10.14	1.05×10^{-4}	4.14×10^{-7}	10.09	1.04×10^{-4}	4.14×10^{-7}	2.42×10^{-5}	3.30×10^{-7}
99.00	5.05×10^{-4}	2.04×10^{-7}	89.78	4.59×10^{-4}	2.04×10^{-7}	1.52×10^{-5}	2.00×10^{-7}

To eliminate electrode contributions to the measured resistance, the conductivity was measured in a four-probe configuration. Gold electrodes were employed. Integrity of the contacts was assured by sputtering a 100 nm layer of gold at the four contact regions (208HR, Cressington, UK) and then applying an additional layer of gold by brush painting (Fuel Cell Materials, Lot #5C149). The sample was then annealed under stagnant air at 900 °C for an hour, ultimately creating porous and interconnected electrodes, as verified by SEM imaging. Gold wires were then securely wrapped around these contact points. The magnitude of the surface reaction rate constant was enhanced in some instances (to improve the accuracy of the measurement of the diffusion coefficient) by application of a layer of Pt nanoparticles to the sample surface. This was achieved by sputtering a 10 nm layer of Pt, which was then annealed for two hours at 900 °C under stagnant air. This procedure yielded a monolayer of uniformly distributed, isolated Pt particles with average size of approximately 100 nm and average inter-particle distance of 400 nm, Figure 3.2.

Measurements were made in an in-house constructed ECR reactor with a sample chamber approximately 1.27 cc in volume. The small size ensured rapid changes in gas-phase $p\mathrm{O}_2$, whereas the use of computer controlled solenoid valves ensured plug flow behavior. For measurements under relatively oxidizing conditions (10^{-5} to 1 atm in $p\mathrm{O}_2$) dry O_2 and Ar mixtures were used. To attain target $p\mathrm{O}_2$ values in the reducing regime ($p\mathrm{O}_2 < 10^{-14}$ atm), mixtures of $\mathrm{H}_2/\mathrm{H}_2\mathrm{O}/\mathrm{Ar}$ or $\mathrm{CO}/\mathrm{CO}_2/\mathrm{Ar}$ were employed. In the former case, the $\mathrm{pH}_2\mathrm{O}$ was set, in all cases, at 0.023 atm by passing pre-

mixed Ar and H_2 gases through a water bubbler held at 23 °C. Equilibrium values of conductivity were first measured using a yttria-stabilized zirconia based oxygen sensor with an integrated s-type thermocouple for monitoring the pO_2 and temperature inside the reactor. For subsequent ECR measurements, only the temperature was directly monitored and the sample conductivity was used to indicate the oxygen partial pressure, a procedure that circumvented calibration difficulties encountered during prolonged use of the sensor.

At each T and pO_2, ECR measurements were repeated two to four times. Step changes were applied in both the oxidation and reduction directions (and equivalence between the two directions confirmed). The average between the initial and final pO_2 values is reported as the measurement pO_2. A Keithley 2420 sourcemeter was used to measure I-V characteristics every second, from which the DC resistance was obtained. The supplied current was adjusted to vary between 1 μA and 50 μA, ensuring that the potential drop across the length of the specimen was under 100 mV. Measurements were made at 750 °C, 800 °C and 850 °C. From an extrapolation of previously reported[89] grain boundary and bulk properties of SDC15 from the same supplier, the present samples with $\sim$3 μm grains are expected to have a maximum grain boundary contribution to the total resistance of no more than 3%. Thus, the relaxation behavior is justifiably taken to reflect the bulk response. Moreover, for the temperature and oxygen partial pressure regimes examined here, the concentration of defects generated in accordance with Equations 3.11 and 3.13 are indeed generally small in concentration relative to the dopant concentration[62]. Specifically, under the most reducing conditions examined, $n = 0.3[Sm'_{Ce}]$. At conditions of enhanced electron concentration, the expressions for computing the defect concentrations (and hence D_{Chem}) from the thermodynamic reduction data change, but analysis of the relaxation data is unmodified.

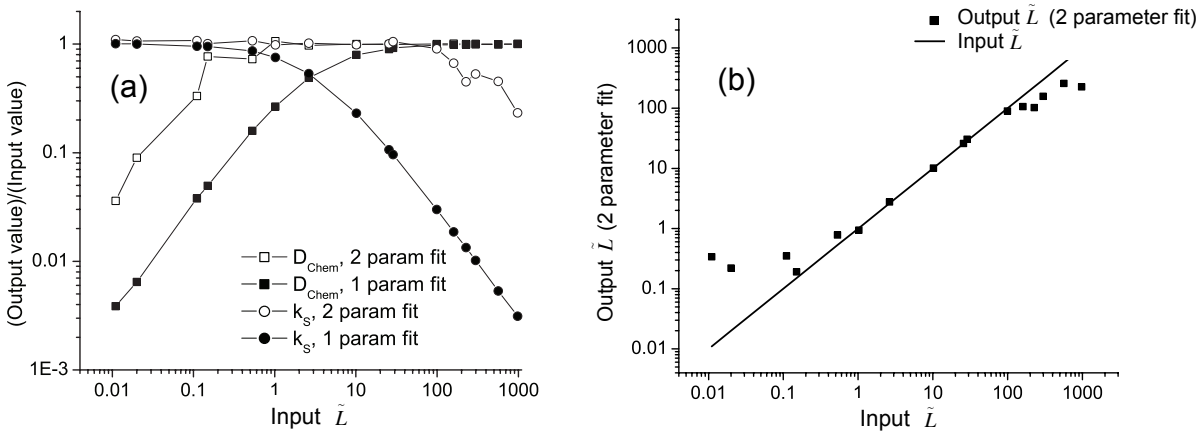

Figure 3.4: Evaluation of numerical procedures developed for analyzing ECR data. (a) Ratio of output to input values of D_{Chem} and k_S as a function of input $\tilde{L}$ for the two parameter and one parameter fits, and (b) output $\tilde{L}$ from the two parameter fit plotted against input values.

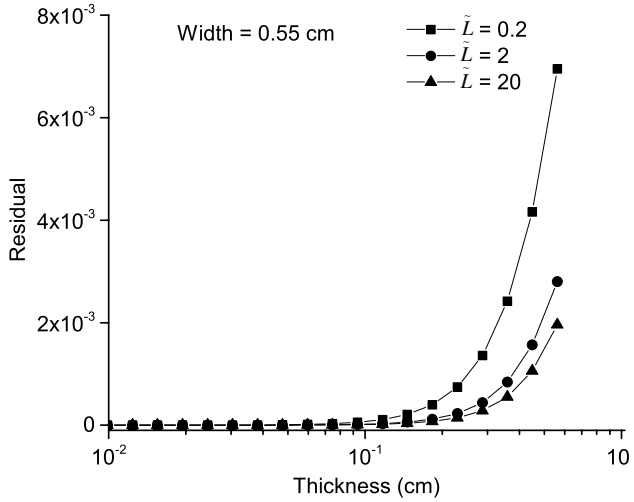

Figure 3.5: The normalized sum of squared deviation of the 1D relaxation model from the 2D relaxation model as a function of sample thickness plotted for $\tilde{L}$ values of 0.2, 2 and 20, keeping the sample width fixed at 0.55 cm. Beyond a sample thickness of 0.15 cm, the assumption of 1D relaxation is no longer valid.

3.3.2 Analysis of relaxation data

The general form of the relaxation profile, Equation 3.4, can be expressed in terms of the α_m and D_{Chem} using Equation 3.3,

$$\frac{\sigma_t - \sigma_0}{\sigma_\infty - \sigma_0} = 1 - \sum_{n=1}^{\infty} \frac{2\ \tan^2(\alpha_m)}{(\alpha_m^2 + \alpha_m^2\ \tan^2(\alpha_m) + \alpha_m\ \tan(\alpha_m))} \exp\left(-\frac{D_{chem}\alpha_m^2 t}{a^2}\right). \qquad (3.30)$$

With this formulation it is evident that there are just 2 independent parameters: D_{Chem} and α_1. The remaining α_m are constrained according to Equation 3.3. Guess values for D_{Chem} and k_S were used to obtain an initial estimate for $\tilde{L}$ and, consequently, via Equation 3.3, the set of α_m. A Matlab routine was developed for then performing a constrained nonlinear fit (Equation 3.30) to the experimental data and obtaining optimized values for D_{Chem} and k_S. To avoid the possibility of converging to an incorrect local minimum, the procedure was repeated numerous times using randomized initial values for D_{Chem} and k_S, each varied over 5 orders of magnitude. In the absence of significant spread, the mode of the distribution of converged estimates is reported as the experimentally derived value. It is to be emphasized that unique values for D_{Chem} and k_S do not necessarily imply accuracy, especially when $\tilde{L} \ll 1$ or $\tilde{L} \gg 1$. In these limiting cases, the same dataset was also analyzed within the framework of the simpler solutions for either surface or bulk diffusion limited processes. In all cases, it was found that the solutions converged with 3 to 4 terms included in the summation.

Prior to analysis of experimental data, the methodology was validated by fitting to numerically synthesized relaxation profiles, generated using given values of D_{Chem} and k_S. For simplicity, but without any lack of generality, the sample thickness, $2a$ was fixed at 0.1 cm. Random noise with amplitude as high as 15% was added to the generated data to simulate experimental noise. This procedure was carried out for 16 datasets, spanning $\tilde{L}$ values from $\approx 10^{-2}$ to 10^3. A comparison between input and output D_{Chem} and k_S values provides an estimate of the errors and guidance on the preferred analysis approach, a two parameter or a single parameter fit. An example fit to simulated data is presented in Figure 3.3a, generated using input D_{Chem} and k_S values of 2.14×10^{-6} cm^2/s and 5.45×10^{-5} cm/s respectively, implying $\tilde{L} = 1.02$. When both diffusion and surface reaction control the relaxation rate, as in this case, the code accurately extracts both D_{Chem} and k_S from the data. The output of fitting using 60 different pairs of initial values for the material parameters converges towards final values that match the original input ones, Figure 3.3b. The histograms of output values of D_{Chem} and k_S, Figures 3.3c and 3.3d, show clear peaks

and minimal scatter. Furthermore, the visual quality of the fit is excellent. In this particular case, the differences between input and output values of D_{Chem} and k_S are 6.5% and 1.6%, respectively, implying that the material properties can be extracted with good accuracy.

Assessing, in a general manner, the confidence level that can be assigned to fit parameters is an important part of any analytical procedure. It can be readily surmised for a conductivity relaxation study that the difference between true (input) and fit (output) D_{Chem} and k_S values will depend on $\tilde{L}$. Specifically, when $\tilde{L}$ is large, the surface reaction step is very fast, implying it has negligible impact on the profile and errors on k_S can be expected to be large. Conversely, when $\tilde{L}$ is small, the fast diffusion process has negligible impact on the profile, and errors on D_{Chem} can be expected to be large. Selected results for a range of input $\tilde{L}$ are highlighted in Table 3.1, and the entire set of the results is represented in Figure 3.4. Figure 3.4a presents the ratio of output to input values of the two material parameters, and Figure 3.4b, a comparison between input and output values of $\tilde{L}$. The fitting is carried out using both the two-parameter and single-parameter models (Equations 3.4, 3.7 and 3.9).

In general, the expectations of accuracy relative to the magnitude of the input $\tilde{L}$ are borne out, Figure 3.4a. When the input $\tilde{L}$ is $\sim$100 or greater, the output k_S is several times smaller than the input value. Similarly, when the input $\tilde{L}$ is 0.15 or less, the output D_{Chem} is many times smaller than the input D_{Chem}. In the high $\tilde{L}$ regions at which diffusion dominates the relaxation process, fits using the single parameter expression (Equation 3.9) and those using the complete expression (Equation 3.4) give virtually indistinguishable values of D_{Chem}. Evidently, little error is introduced into D_{Chem} despite the risk of overfitting of the data using the two-parameter expression. In contrast, in the low $\tilde{L}$ regions the difference between the k_S values obtained from the two-parameter and the single-parameter fits is non-negligible. In the specific range examined of $\tilde{L} = 0.01$ to 0.1, the two-parameter fit gives errors of 7-10% for k_S, whereas the single-parameter fit gives errors of 0-4%. In this case, there is clear benefit, beyond computational efficiency, in selecting the simpler solution for analysis. Based on these results, one can conclude that a single parameter fit for only D_{Chem}

is appropriate when $\tilde{L}$ is 100 or greater, a two-parameter fit for both D_{Chem} and k_S is appropriate when $\tilde{L}$ lies between 100 and 0.15, and that a single parameter fit is appropriate when $\tilde{L}$ is 0.15 or smaller. In general, high accuracy in k_S is obtained over a wider range of $\tilde{L}$ than is the case for D_{Chem}.

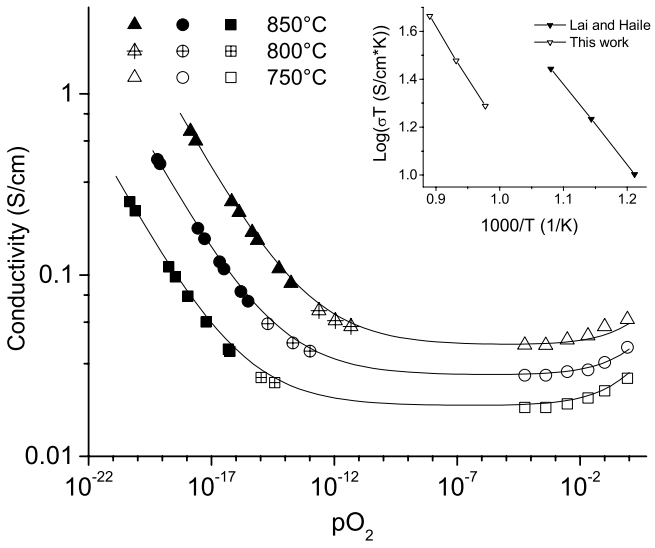

Figure 3.6: Log-log plot of electrical conductivity of SDC15 vs pO_2. Solid, cross-hair inscribed and open symbols respectively indicate data points obtained using H_2/H_2O, CO/CO_2 and dry O_2/Ar mixtures. Solid lines show fit to Equation 3.31. Inset is an Arrhenius plot of the ionic conductivity compared with the work of Lai and Haile[62].

The discussion above is framed in terms of the actual (or input) $\tilde{L}$. However, what one obtains from an analysis of experimental data is the output $\tilde{L}$. From Figure 3.4b, it can be seen that these two quantities are almost identical when $\tilde{L}$ lies between 0.15 and 100, consistent with the appropriateness of a two-parameter fit in this region. At the extrema, however, $\tilde{L}$ appears to plateau at ∼0.15 and ∼100. Because the D_{Chem} value obtained at high $\tilde{L}$ is insensitive to whether a two- or single-parameter fit is selected, accurate knowledge of $\tilde{L}$ is not required for accurate determination of the diffusivity. In the case of k_S, however, enhanced accuracy when using the single parameter fit at small $\tilde{L}$ motivates identification of the appropriate formalism. From the data in Figure 3.4a, it is apparent that k_S from the two parameter fit is always greater than that from the single parameter fit. However, the difference between

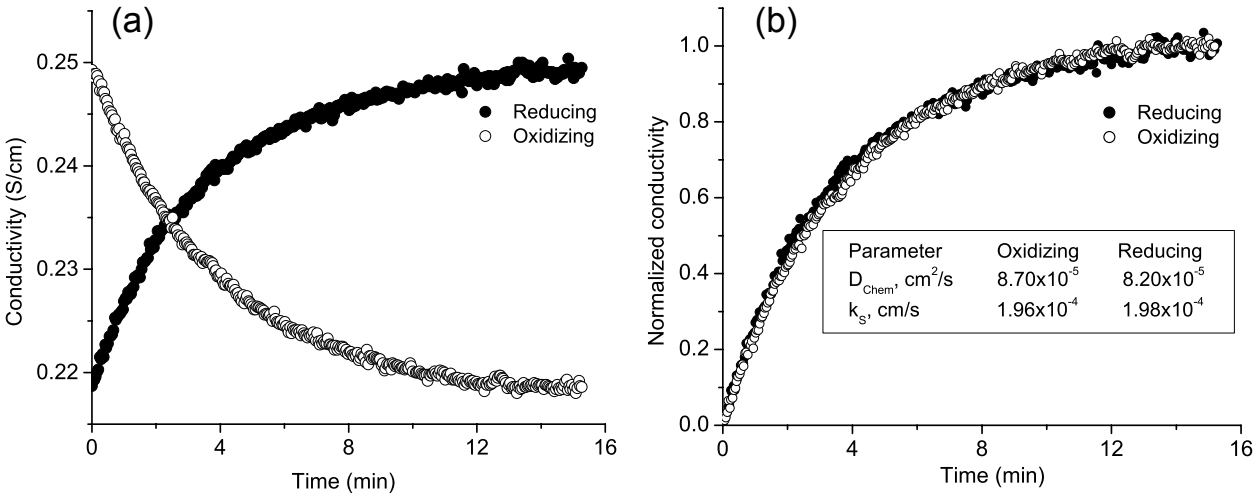

Figure 3.7: (a) Raw conductivity relaxation profiles along reducing and oxidizing directions for a pO_2 switch between between 6.60×10^{-17} atm and 1.33×10^{-16} atm at 850 °C. The 0.8 mm sample was sputtered with Pt catalyst particles. (b) The normalized conductivity relaxation profiles are statistically identical, confirming that the ΔpO_2 is small enough to ensure the driving force, D_{Chem} and k_S are the same along both directions and that the system response is linear.

the two drops to about 5% when the input $\tilde{L}$ is less than 0.15. This observation provides the final guidance on how to select the fitting procedure in the absence of *a priori* knowledge of the true $\tilde{L}$. Specifically, if k_S (2-parameter) differs from k_S (1-parameter) by less than 5%, the latter is likely closer to the 'true' value.

The analysis performed on this broad set of simulated data provides universal guidance on the most suitable analysis procedures for extracting D_{Chem} and k_S from conductivity relaxation profiles. The results in Figure 3.4 furthermore provide an estimate of the uncertainties in the derived values when the optimal fitting procedure has been employed. It is to be emphasized, however, that if the wrong single-parameter fitting procedure is utilized, the output parameters will be almost valueless. For example, for an input $\tilde{L}$ of 0.11, a fit using only D_{Chem} gives a diffusivity that is almost 30 times larger than the true value. Unless one also analyzes the data using the two-parameter methodology or can visually recognize a poor fit, the factor of 30 error could be easily overlooked. The analogous situation holds for an evaluation of k_S

from a single-parameter fit at large $\tilde{L}$. Accordingly we conclude that, in the absence of *a priori* knowledge of (approximate) material properties, any analysis of ECR profiles must include two-parameter fits as well as selected use of single-parameter fits in order to ensure accuracy of the output parameters.

An assessment of the validity of a 1D solution for the samples fabricated here was carried out by computing the difference between relaxation profiles generated using Equation 3.4 and those generated using the analogous 2D expression[74]. The difference is defined as

$$\sum_{n=1}^{N} \frac{(\tilde{\sigma}_{1\mathrm{D}}(n\Delta t) - \tilde{\sigma}_{2\mathrm{D}}(n\Delta t))^2}{N},$$

where $\tilde{\sigma}_{1\mathrm{D}}$ and $\tilde{\sigma}_{2\mathrm{D}}$ are the relaxation profiles generated using the 1D and 2D models respectively, Δt is the simulation time step and N is the total number of time steps. The calculation was performed for samples with thicknesses varying from 0.01 to 0.55 cm at selected (fixed) values of $\tilde{L}$. For generation of the profile from the 2D sample, the width was set to 0.55 cm. This brief analysis, presented in Figure 3.5, indicates that the errors in k_S and D_{Chem} will exceed $\sim 15\%$ when $2a$ reaches 20% of the next largest dimension. Accordingly, samples with thicknesses greater than 0.11 cm were analyzed using the 2D solution to the diffusion equation. The 2D analysis yielded broad histograms in the output k_S and D_{Chem} values, and in contrast to the 1D analysis, the modes of these distributions did not correspond to the solution with the minimum least squared error. For these cases, the latter are reported as the experimentally derived values.

3.4 Results and discussion

3.4.1 Equilibrium conductivity

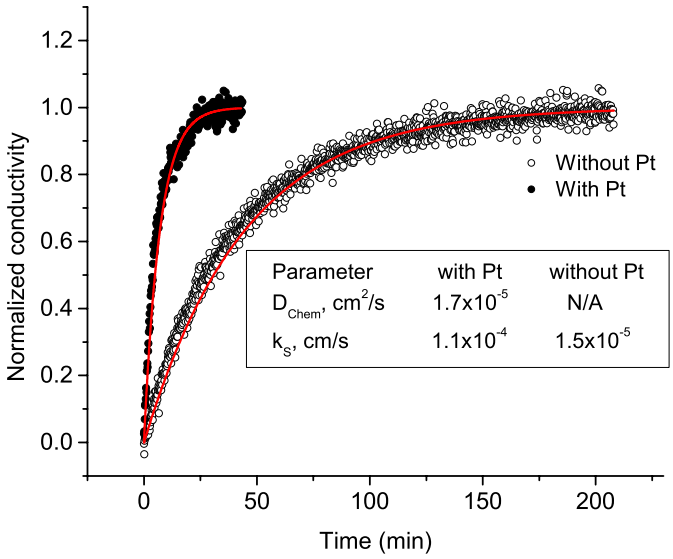

Figure 3.8: Relaxation profile of 0.8 mm thick SDC 15 sample with and without Pt catalyst on the surface for identical measurement conditions. $T = 750$ °C, $p\mathrm{H}_2 = 0.1$ atm, $p\mathrm{H}_2\mathrm{O} = 0.023$ atm, balance Ar. $\Delta p\mathrm{O}_2 = 6.0 \times 10^{-21}$atm to 2.0×10^{-21}atm. The solid red lines are fit profiles. Without Pt, only the slow surface reaction step could be measured.

Figure 3.6 shows the $p\mathrm{O}_2$ dependence of the total electrical conductivity of SDC15 at 750, 800 and 850 °C, with relevant transport parameters summarized in Table 3.2. Under reducing conditions (low $p\mathrm{O}_2$), the total conductivity is predominantly electronic, showing the expected n-type behavior with a -0.25 power law dependence on $p\mathrm{O}_2$. Morever, the value of the n-type conductivity is in excellent agreement with earlier results from Lai [62] and from Chueh[90] reported from similar starting materials. With increasing $p\mathrm{O}_2$, the conductivity plateaus to a constant value, reflecting the occurrence of the electrolytic regime. At the highest values of $p\mathrm{O}_2$, the total conductivity increases, indicating the onset of p-type conductivity. However, the power law dependence is found to be best described with an exponent of 0.35 rather than

the expected value of 0.25. The solid lines in the figure reflect a fit to the expression

$$\sigma_{tot} = \sigma_n^0 p\mathrm{O}_2^{-0.25} + \sigma_{ion} + \sigma_p^0 p\mathrm{O}_2^{0.35} \tag{3.31}$$

rather than to Equation 3.14, and it is evident the data are well-represented by this expression. The ionic conductivity derived from the fit is shown in the inset of Figure 3.6.

Table 3.2: Parameters describing the conductivity of SDC15, based on a fit of the expression in Equation 3.31 to determine the ionic, n-type, and p-type conductivities, as well as fit to an Arrhenius expression ($\sigma T = A\exp(-E_a/k_bT)$).

	E_a, eV	A, S/cm K	σ (800 °C) S/cm
Ionic	0.85	2.95×10^5	0.029
n-type	2.35	7.6×10^8	0.222 ($p\mathrm{O}_2 = 10^{-18}$ atm)
p-type	0.22	2.18×10^2	0.051 ($p\mathrm{O}_2 = 1$ atm)

In contrast to the n-type conductivity, the ionic conductivity measured here is lower, by about a factor of three, than that obtained earlier by Lai for SDC15 [62] (see inset). The activation energy for ionic transport obtained here is, however, consistent with typical bulk values[91], supporting the statement that grain boundary influences on the relaxation behavior are negligible. The difference between previous and present measurements is tentatively attributed to the differences in source materials (although the powders were from the same supplier, they were of different types, nanocrystalline versus microcrystalline), as well as slightly different pellet fabrication procedures, with a more aggressive sintering protocol having been employed here in order to obtain large grains. A comparable level of scatter in the literature has been noted by Mogensen et al. for 20 mol% Sm and Gd doped ceria [17]. In that case, the scatter was hypothesized to originate from differences in grain boundary contributions to the total resistance. The microstructure of the present samples renders such an explanation unlikely to be applicable in this work (as the grains are large enough to render the grain boundary contribution negligible, as discussed above). Nevertheless, the low number density of grain boundaries in the materials studied here can be conceived to influence the impurity levels in the bulk and, through that avenue, plausibly influence

the bulk ionic conductivity. It is to be emphasized that the EPMA results show the Sm doping level to match the nominal value of 15 mol%, and thus a reduced dopant level cannot be responsible for the reduced ionic conductivity.

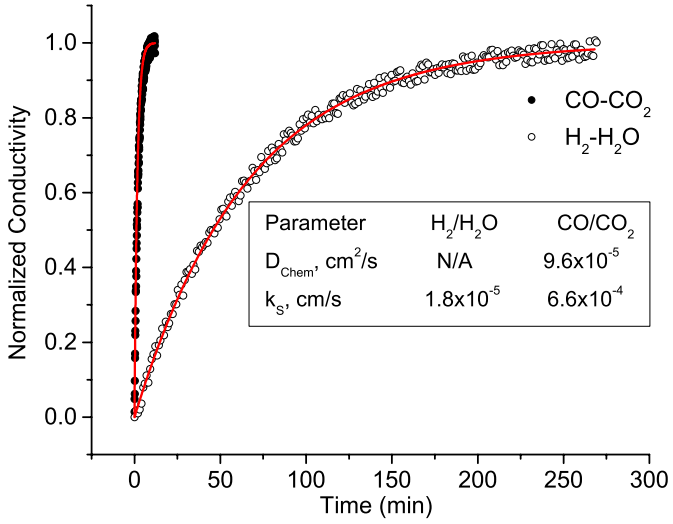

Figure 3.9: Relaxation profiles of a 1.72 mm thick SDC 15 sample at 800 °C, $pO_2 = 2.3 \times 10^{-15}$ atm using H_2/H_2O ($\Delta pO_2 = 3.0 \times 10^{-15}$ atm to 1.7×10^{-15} atm) and $pO_2 = 2.2 \times 10^{-13}$ using CO/CO_2 ($\Delta pO_2 = 3.4 \times 10^{-13}$ atm to 1.0×10^{-13} atm) mixtures. The solid red lines are fit profiles. Although D_{Chem} is slightly higher under the more oxidizing conditions of the CO/CO_2 experiment, the dramatically enhanced relaxation rate is largely a result of the differences in k_S.

3.4.2 Relaxation behavior

Example relaxation profiles are presented in Figure 3.7 for a measurement carried out under reducing conditions in an H_2-H_2O-Ar mixture at 850 °C using a Pt-catalyzed sample 0.8 mm in thickness ($a = 0.4$ mm), in both the oxidizing and reducing directions. It is apparent that the forward and reverse directions yield normalized conductivity profiles that are statistically identical, confirming that the step change between 6.6×10^{-17} and 1.3×10^{-16} atm was small enough to justify the assumptions of the analytical procedure.

The dramatic influence of Pt nanoparticles alluded to above on the relaxation process is evident in Figure 3.8. In the absence of Pt, the relaxation time for the step

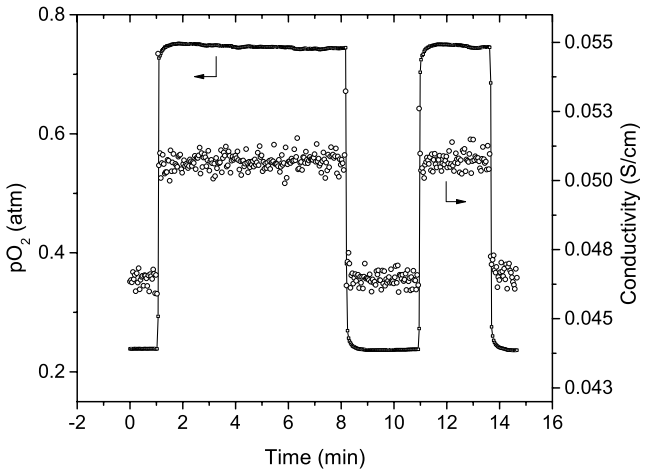

Figure 3.10: Electrical conductivity and pO_2 as a function of time for a step change ΔpO_2: 2.6×10^{-1} atm and 7.9×10^{-1} atm (p type behavior) at 850 °C. A 0.8 mm thick sample without Pt catalyst on the surface shows dramatically fast re-equilibration times, less than 5 seconds. Also, note the pO_2 switch times of 1 to 2 seconds.

change reflected in Figure 3.7 increased from ∼20 to ∼200 min, and $\tilde{L}$ decreased from 0.28 to a value less than 0.1, motivating an analysis according to Eq. 3.7 for a process entirely limited by the surface reaction step. As described above, it was anticipated, based on the reported values of D_{Chem} and k_S under H_2/H_2O/Ar mixtures, that SDC samples of the dimensions utilized here would be surface reaction limited. That Pt, which can only influence k_S, enhances the relaxation rate directly confirms the expectation of a surface reaction limited process. A consequence of the relatively slow surface reaction kinetics on bare SDC15 is the inaccessibility of D_{Chem} from samples thin enough to retain the validity of the 1D approximation. Rather than increase a to achieve $\tilde{L} \geq 0.15$, an adjustment which would have dramatically increased the measurement time, all measurements of D_{Chem} under H_2-H_2O-Ar mixtures were carried out using Pt catalyzed samples. While elucidation of the mechanisms by which Pt catalyzes the dissociation/formation of H_2O on the surface of doped ceria is beyond the scope of this study, we note that Wang et al. have recently reported a similar enhancement in conductivity relaxation rates in doped ceria in the presence of Pt nanoparticles[70]. More generally, it is widely recognized that precious metal particles on ceria supports form a highly active combination for catalyzing a broad

range of chemical reactions[92]. The ECR method provides a rigorous approach for studying these phenomena.

Additional evidence for the major role of surface reaction kinetics in the relaxation behavior of SDC15 samples of moderate thickness (specifically 1.72 mm) under reducing conditions is presented in Figure 3.9, in which the profiles of the bare oxide under H_2-H_2O-Ar and CO-CO_2-Ar at 800 °C are compared. Although D_{Chem} is slightly larger under the more oxidizing conditions of the CO-CO_2-Ar experiment, $pO_2 = 2.2 \times 10^{-13}$ vs $pO_2 = 2.3 \times 10^{-15}$ atm, the observed 10-fold reduction in relaxation time is, by far, a result of the increased surface reaction rate. A fit to the relaxation data reveals that the k_S in the CO-CO_2-Ar mixture is a remarkable ∼40 times greater than it is in the H_2-H_2O-Ar mixture (an order of magnitude greater than it is on Pt-catalyzed SDC15 in H_2-H_2O-Ar). Again, studying the catalytic behavior of SDC is beyond the scope of this paper, but these preliminary data immediately suggest that thermochemical production of CO will be kinetically favorable over H_2 production. Furthermore, from the perspective of ECR experimental design, the rapid surface exchange enables ready measurement of D_{Chem} in the intermediate pO_2 region accessible using CO-CO_2-Ar mixtures without the need for a catalyst. Conversely, whereas an initial evaluation of literature values of k_S and D_{Chem} indicated these experiments would be well within the surface reaction limited regime, a co-limited process is clearly encountered under CO/CO_2 mixtures. This result highlights the importance of evaluating the data in an unbiased manner, without presupposing the nature of the experimental regime.

An example relaxation profile under oxidizing conditions is presented in Figure 3.10 for a sample 0.8 mm in thickness as measured at 850 °C. At the outset it was anticipated, as discussed above, that measurements under these conditions would be difficult due to the low sensitivity of total conductivity to pO_2 in this regime. However, changes in conductivity between the start and finish of the relaxation of ∼3% are evident and readily recorded, consistent with the enhanced electronic transference numbers of the SDC15 employed here. At a pO_2 of 0.5 atm, the electronic contribution to the transport is p-type, as evidenced by the increase in conductivity with

increasing pO_2 and also directly indicated by the equilibrium conductivity results, Figure 3.6. A striking feature of these profiles is the exceptionally fast response time of 10 s, approaching the reactor flush time of 1 to 2 s and precluding the extraction of meaningful kinetic parameters. The sample thickness had to be increased to 1.72 mm to sufficiently slow the relaxation kinetics and enable acquisition of useful data (not shown). Although these thicker samples required analysis according to the 2-dimensional solution (Figure 3.5) and accordingly substantially longer computing times, both k_S and D_{Chem} could be reasonably determined.

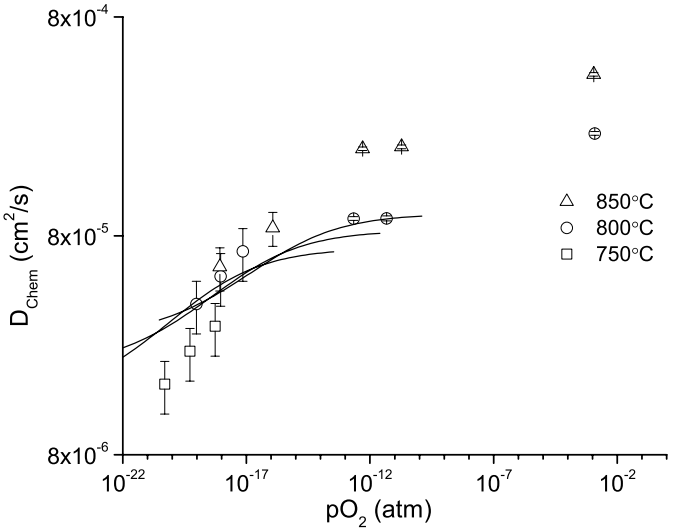

Figure 3.11: D_{Chem} as a function of pO_2 at 750 °C, 800 °C and 850 °C from this study overlaid on approximate analytical values computed assuming an ideal solution model (computed values based on extrapolations of defect concentrations and mobilities measured at lower temperatures[62]).

The diffusivity results obtained from these experiments are summarized in Figure 3.11 with errors, which represent the minimum fitting errors, estimated from the analysis presented in Fig. 3.4. The directly measured values are compared to those computed using the conductivities presented in Figure 6 and thermodynamic properties reported by Lai and Haile[62]. Overall, the agreement is satisfactory, validating the methodology. Under the most reducing conditions of this study, at which the defect concentrations are dominated by the Brouwer approximation of Equation 3.10, but conductivity is n-type, $\sigma_{ion} < \sigma_n$ and $c_{ion} > c_n$, leading to a D_{Chem} that is

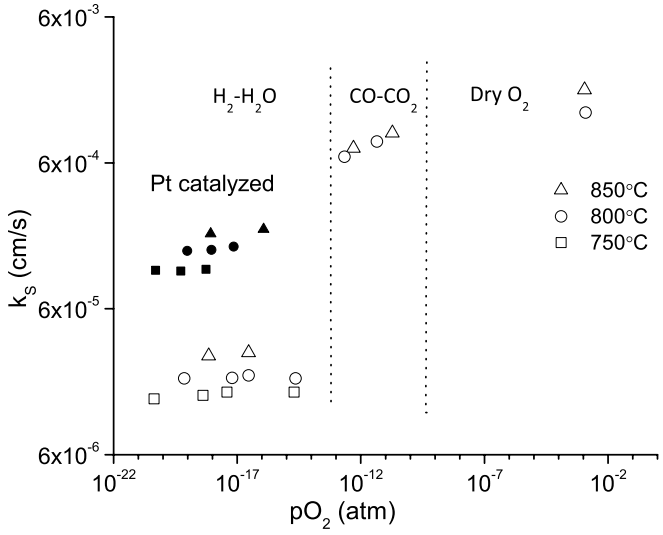

Figure 3.12: k_S as a function of $p\mathrm{O}_2$ at 750 °C, 800 °C and 850 °C from this study. The abrupt jump in k_S at intermediate $p\mathrm{O}_2$ corresponds to a change in the gas mix from $\mathrm{H}_2/\mathrm{H}_2\mathrm{O}$ to $\mathrm{CO}/\mathrm{CO}_2$. While D_{Chem} is dependent only on $p\mathrm{O}_2$, k_S shows a much stronger dependence on the gas species.

inversely proportional to c_n and hence decreases with decreasing $p\mathrm{O}_2$. Under moderately oxidizing conditions (*i.e.*, the electrolytic regime), although D_{Chem} becomes difficult to measure by ECR, its behavior can be described. In this region, $\sigma_{ion} > \sigma_n$ and $c_{ion} \gg c_n$, and thus D_{Chem} asymptotes to $D_n = \frac{RT}{F^2}\frac{\sigma_n}{c_n}$. Under these conditions the minority carrier dominates the ambipolar diffusion process. The slight deviation between experiment and calculation under moderate to low $p\mathrm{O}_2$ may be the result of a small dependence of the electronic mobility on oxygen partial pressure, as suggested elsewhere[21]. The very weak dependence of D_{Chem} on temperature is a direct result of the competing temperature dependences of mobility and defect concentrations. A significant feature of Figure 10 is the very large D_{Chem} measured when the electronic conductivity is p-type, about a factor of 3 larger than when it is n-type. When holes become the dominant minority carrier, D_{Chem} can be expected to approach D_p rather than D_n, implying that the higher chemical diffusivity is a result of the higher mobility of holes over electrons. The hole mobility can be roughly estimated using the expression

$$\mu_p = \frac{eD_p}{k_B T}, \tag{3.32}$$

which yields a value of $\sim 2 \times 10^{-3}$ $cm^2V^{-1}s^{-1}$ at 800 °C, approximately 50% greater that the electron mobility (obtained from an extrapolation of the data published by Lai and Haile[62]). Reliable values of hole mobility in rare-earth doped ceria are unavailable from the literature due to the difficulty of accurately of determining the hole concentration (the latter is required for determining mobility from a measurement of hole conductivity). We suggest that the hole mobility exceeds that of the electrons because of the delocalized nature of the O 2p band (the origin of the holes). In contrast, the electrons are localized in the Ce 4f states[28], effectively behaving as polarons, and hence are less mobile. Using the estimated mobility and the measured conductivity, the hole concentration can further be estimated, and the resulting value is 4.2×10^{19} cm^{-3} at 800 °C and 1 atm oxygen partial pressure. This concentration is equal to the electron concentration that appears at the same temperature and an oxygen partial pressure of 1.2×10^{-14} atm. This rough analysis indicates that the mobilities and concentrations of holes required for explaining the high diffusivities and observed p-type conductivity are reasonable.

The surface reaction rate data, summarized in Figure 3.12, are striking. As already noted, the overall magnitude of k_S obtained under H_2-H_2O-Ar mixtures is generally consistent with what has been observed in the literature. However, k_S decreases slightly with decreasing pO_2. Our results thus not only contradict the results obtained from electrochemical measurements carried out at slightly lower temperatures, but also the general expectation that surface reaction rates increase with increasing vacancy concentration. On the other hand, the data seem to obey the often noted correlation between D_{Chem} and k_S[59]. Most significantly, the surface reaction constant is more than two orders of magnitude higher under CO-CO_2-Ar and O_2-Ar than it is when H_2O is present. Again, there is some precedence for such a result, with Yashiro and coworkers also having seen a higher k_S for ECR measurements under CO-CO_2-Ar than under H_2-H_2O-Ar[61], however, the underlying mechanisms that lead to this behavior remain to be elucidated. It is further noteworthy that k_S values under CO-CO_2-Ar and under O_2-Ar mixtures are very similar, despite the dominance

of electrons as the minority carriers in the former case and holes in the latter. Another surprising result is the very weak temperature dependence of k_S, irrespective of gas atmosphere. Overall, this rich set of behaviors sets the stage for employing ECR methods to fully explore and understand the catalytic properties of ceria and its derivatives.

3.5 Conclusions

We have evaluated the oxygen transport properties of bulk samples of SDC15 over a wide range of pO_2 at 750 °C, 800 °C and 850°C using electrical conductivity relaxation. SDC was chosen as a benchmarking material to demonstrate the versatility and robustness of numerical procedures developed to directly extract both bulk chemical diffusivity and surface reaction rate constant. The methodology is proven to be sound, provided the sample geometry and microstructure are tailored to justify the approximations of the analytical approach.

Beyond method validation, several new insights are afforded by this study of SDC. The slightly enhanced p-type conductivity of the SDC15 employed here enables ECR measurements under oxidizing conditions, and we find that D_{Chem} is substantially higher in the p-type region than it is in the n-type. Both results, the high p-type conductivity and the high D_{Chem}, point towards much higher hole than electron mobility. The surface reaction constant in SDC is highly dependent on the nature of the gaseous species. Relative to CO-CO_2-Ar mixtures, H_2-H_2O-Ar mixtures appear to have a poisoning effect on the surface of SDC. The rate constants on bare SDC15 in the presence of H_2O are nearly 40 times lower than they are in its absence. The rapid surface reaction kinetics under CO-CO_2-Ar mixtures suggests kinetic advantages for the production of CO rather than H_2 in a two-step thermochemical process. The combination of extremely high D_{Chem} and extremely high k_S under relatively oxidizing conditions (leading to extremely short relaxation times) suggests the possibility of using SDC as a pO_2 sensor in oxygen-rich environments.

For all cases examined in this study (samples several hundred μm in thickness)

the relaxation was either largely or entirely surface reaction limited. In both thermochemical and fuel cell electrode applications, SDC is employed in a morphology with short diffusion distances, several to several tens of microns, suggesting that surface reaction limitations will dominate the performance of real devices. Accordingly, efforts at understanding and enhancing surface reaction kinetics will be essential for advancing these technologies.

Chapter 4

Effect of Zr addition on transport properties of ceria : an electrical conductivity relaxation study

4.1 Background

Ceria-zirconia solid solutions find widespread use as catalysts in 3-way catalytic converters in automobiles and steam reforming of methane[92, 93] owing to their ability to act as an excellent oxygen buffer. Though Zr^{4+} is isovalent with Ce^{4+}, its addition to ceria has been shown to facilitate $Ce^{4+} \rightarrow Ce^{3+}$ reduction at lower temperatures[3,4]. This has been attributed to the preference of the smaller Zr^{4+} to exist in seven-fold coordination, favoring oxygen vacancies in its nearest-neighbor shell[94]. Indeed, first principles calculations based on density functional theory have shown a marked reduction in the vacancy formation energy in the presence of Zr^{4+}[95]. The enhanced reducibility of zirconia doped ceria (ZDC) also makes it a potential candidate for use as a reaction intermediate in solar driven thermochemical cycles to split water[19, 21, 22].

Despite the widespread applications of zirconia doped ceria that utilize its enhanced reducibility, not much work has been done to understand the fundamental thermodynamic and kinetic properties. The enthalpy and entropy of reduction and the oxygen non-stoichiometry variation with temperature and oxygen partial pressure have only recently been determined[96, 97]. Addition of up to 50 mol % Zr has been

reported to increase the electrical conductivity of ceria within the framework of cubic fluorite structure[98, 99]. Chiodelli et al.[98] showed that the conductivity is n type and predominantly electronic above 600°C from thermoelectric power measurements. However, in the absence of non-stoichiometry data, they ruled out an enhancement in carrier concentration and attributed the increase in conductivity to higher electron mobility in ZDC. Recent thermogravimetric studies[97] have shown that Zr, in fact, lowers the reduction enthalpy by as much as 40% and consequently increases the carrier concentration. Hence, a clear picture of electrical conductivity of ZDC over a wide range of oxygen partial pressures has still not emerged. Further, the $p\mathrm{O}_2$ dependence of electrical conductivity, chemical diffusion coefficient, and surface reaction rate constant have not been reported.

In case of undoped ceria, the redox thermodynamics and defect chemistry are well established[1, 2] and several authors have reported the electrical conductivity over a wide range of temperatures and oxygen partial pressures[100, 101, 2]. Panhans and Blumenthal[2] showed that the impurity content in ceria strongly influences its defect structure and electrical properties close to stoichiometry. By systematically varying the purity level between 99.9999% and 99.5%, they were able to observe p type, n type and electrolytic behavior at high $p\mathrm{O}_2$, between 600°C and 1000°C. The conductivity of reduced ceria is n type and predominantly electronic, showing deviations from ideal solution behavior[101] and a $p\mathrm{O}_2$ dependent enthalpy of migration[100]. However, the $p\mathrm{O}_2$ dependence of the oxygen transport properties, D_{Chem} and k_S, have not yet been studied. Knowledge of the transport parameters of both ceria and ZDC is essential to systematically assess the effect of Zr doping on the kinetics of two-step water splitting thermochemical cycles.

We have investigated the effect of 20 mol% Zr doping on the electrical conductivity and oxygen transport properties of $\mathrm{CeO}_{2-\delta}$ using electrical conductivity relaxation (ECR). Aside from retaining the cubic fluorite structure of ceria[102], 20% Zr doped ceria (ZDC20) also has favorable thermodynamics for two step thermochemical cycles, making it an ideal composition to perform kinetic studies on. In ECR, a step change in the oxygen activity of the surrounding gas phase causes the non-stoichiometry

of the oxide to re-equilibrate. For small step changes, the non-stoichiometry can be linearly related to electrical conductivity, whose time evolution is measured and described using solutions to Fick's second law under appropriate boundary conditions to extract the kinetic parameters. While the sample conductivity is a measure of the mobility of the majority carrier, the chemical diffusion coefficient obtained from fits to the relaxation profiles is determined by the slower moving species.

Relaxation methods have been employed to study the oxygen transport properties of rare earth (Sm, Gd) doped ceria in bulk[60, 61, 103] and thin film geometry[69]. In these oxides, the vacancy concentration is fixed by the dopant in the temperature and oxygen partial pressure range of measurements and ideal solution behavior is observed up to δ values as high as 0.05[87, 62]. These two factors greatly simplify the thermodynamic treatment of defect chemistry and allow approximations for D_{Chem} (and to a lesser degree, k_S) as a function of T and $p\mathrm{O}_2$. Undoped ceria, on the other hand, is known to display non-ideal behavior for δ values as low as 0.007[1, 104, 55, 105], rendering such approximations invalid. Electrical conductivity relaxation is advantageous for such oxides, since the kinetic parameters are determined from the transients without resorting to any defect chemical relations.

4.2 Defect chemistry of undoped ceria

The defect chemistry of undoped ceria has been extensively studied[1, 2, 17] and it is widely established that the predominant defects in ceria are oxygen vacancies and electrons localized on Ce sites (called small polarons). The reduction reaction can be expressed as

$$2\mathrm{Ce}_{\mathrm{Ce}}^{\times} + \mathrm{O}_{\mathrm{O}}^{\times} \longleftrightarrow \mathrm{V}_{\mathrm{O}}^{\bullet\bullet} + 2\mathrm{Ce}_{\mathrm{Ce}}^{\prime} + \frac{1}{2}\mathrm{O}_2, \tag{4.1}$$

where $\mathrm{Ce}_{\mathrm{Ce}}^{\times}$, $\mathrm{O}_{\mathrm{O}}^{\times}$, $\mathrm{V}_{\mathrm{O}}^{\bullet\bullet}$ and $\mathrm{Ce}_{\mathrm{Ce}}^{\prime}$, written in Kröger-Vink notation[77], denote Ce^{4+}, O^{2-}, oxygen vacancy and Ce^{3+} (equivalently, electrons) respectively. In the dilute

limit, the defect reaction leads to the law of mass action :

$$K_R = \frac{[\mathrm{Ce}'_{\mathrm{Ce}}]^2[\mathrm{V}_{\mathrm{O}}^{\bullet\bullet}]}{[\mathrm{Ce}^{\times}_{\mathrm{Ce}}]^2[\mathrm{O}^{\times}_{\mathrm{O}}]} p\mathrm{O}_2^{1/2}, \tag{4.2}$$

where K_R is the reduction equilibrium constant and terms in [ ] are fractional concentrations. Residual impurities - typically lower valence cations - are inherent in most samples. Previous investigations have reported that Ca is the dominant impurity, with concentrations ranging from 200 to 900 ppm[1, 106, 2]. The substitution of Ce by Ca results in two excess electrons, which is compensated by creation of an oxygen vacancy:

$$\mathrm{CaO} \longleftrightarrow \mathrm{Ca}''_{\mathrm{Ce}} + \mathrm{V}_{\mathrm{O}}^{\bullet\bullet} + \mathrm{O}^{\times}_{\mathrm{O}}, \tag{4.3}$$

where $\mathrm{Ca}''_{\mathrm{Ce}}$ denotes Ca on a Ce site. In the ensuing analysis, $[\mathrm{Ca}''_{\mathrm{Ce}}]$, represented by y, is used to denote an 'effective Ca concentration' equaling the charge sum of all lower valence cation impurities. The total vacancy concentration is the sum of impurity generated extrinsic vacancy concentration, $[\mathrm{V}_{\mathrm{O}}^{\bullet\bullet}]^{ext} = y/2$, and the intrinsic vacancy concentration (following Eq. 4.1), $[\mathrm{V}_{\mathrm{O}}^{\bullet\bullet}]^{int} = \delta/2$,

$$[\mathrm{V}_{\mathrm{O}}^{\bullet\bullet}] = [\mathrm{V}_{\mathrm{O}}^{\bullet\bullet}]^{ext} + [\mathrm{V}_{\mathrm{O}}^{\bullet\bullet}]^{int} = \frac{y}{2} + \frac{\delta}{2} \tag{4.4}$$

Through the requirement of site and charge balance, it can be shown that $[\mathrm{Ce}'_{\mathrm{Ce}}] = 2\delta$, $[\mathrm{Ce}^{\times}_{\mathrm{Ce}}] = 1-2\delta-y$ and $[\mathrm{O}^{\times}_{\mathrm{O}}] = 1-\delta/2$. Using these expressions, Eq. 4.2 can be recast as

$$K_R = \frac{(2\delta)^2\left(\frac{\delta}{2} + \frac{y}{2}\right)}{(1-2\delta-y)^2\left(1-\frac{\delta}{2}\right)} p\mathrm{O}_2^{1/2} \tag{4.5}$$

Since y is typically < 1000 ppm, its effect on $[\mathrm{Ce}^{\times}_{\mathrm{Ce}}]$ can be assumed to be insignificant. Under oxidizing conditions, where the concentration of intrinsic vacancies is much smaller than that of impurity generated vacancies, i.e. , $\delta \ll y$, $[V_O^{\bullet\bullet}] \approx y/2$ and the

denominator in Eq. 4.2 is taken to be unity, giving

$$n = \left(\frac{2K_R}{y}\right)^{1/2} p\mathrm{O}_2^{-1/4} \tag{4.6}$$

Under reducing conditions, $\delta \gg y$, $[V_O^{\bullet\bullet}] \approx \delta/2$ and Eq. 4.2 yields

$$K_R = \frac{(2\delta)^2\left(\frac{\delta}{2}\right)}{(1-2\delta)^2\left(1-\frac{\delta}{2}\right)} p\mathrm{O}_2^{1/2} \tag{4.7}$$

If $\delta \ll 1$, Eq. 4.7 can be re-arranged to derive the well known $p\mathrm{O}_2^{-1/6}$ power law behavior of δ,

$$\delta = \left(\frac{K_R}{2}\right)^{1/3} p\mathrm{O}_2^{-1/6}. \tag{4.8}$$

The power law expressions in Eqs. 4.6 and 4.7 hold if K_R does not vary with δ, which requires the standard reduction enthalpy, ΔH_R^0 and entropy, ΔS_R^0 to be independent of vacancy concentration. Independent of a defect model, the reduction of ceria can also be described by the following chemical reaction:

$$\lim_{\Delta\delta\to 0} \frac{1}{\Delta\delta}\mathrm{CeO}_{2-\delta} \longleftrightarrow \frac{1}{\Delta\delta}\mathrm{CeO}_{2-\delta-\Delta\delta} + \frac{1}{2}\mathrm{O}_2 \tag{4.9}$$

The standard free energy change for this reaction, equivalent to the partial molar free energy of oxygen in $\mathrm{CeO}_{2-\delta}$, can be related to $p\mathrm{O}_2$ as

$$\Delta G_O^0(\delta) = -RT\ln(p\mathrm{O}_2) = \Delta H_O^0(\delta) - T\Delta S_O^0(\delta) \tag{4.10}$$

$\Delta H_O^0(\delta)$ and $\Delta S_O^0(\delta)$ are respectively the standard partial molar enthalpy and entropy per mole of neutral oxygen atoms. The defect chemical reaction in Eq. 4.1 and the partial molar reaction in Eq. 4.9 are formally identical – both represent an infinitesimal change in the non-stoichiometry from δ to $\delta + \Delta\delta$. However, their energetics are

subtly different. Substituting for K_R from Eq. 4.5 in

$$\Delta G_R^0 = -RT\ln(K_R) \tag{4.11}$$

we get

$$\Delta G_R^0 = -RT\ln\left(\frac{[Ce'_{Ce}]^2[V_O^{\bullet\bullet}]}{[Ce_{Ce}^{\times}]^2[O_O^{\times}]}\right) - \frac{1}{2}RT\ln(p\mathrm{O}_2). \tag{4.12}$$

Combining Eqs. 4.10 and 4.12, we have

$$\Delta H_R^0 - T\Delta S_R^0 = -RT\ln\left(\frac{[Ce'_{Ce}]^2[V_O^{\bullet\bullet}]}{[Ce_{Ce}^{\times}]^2[O_O^{\times}]}\right) + \Delta H_O^0 - T\Delta S_O^0, \tag{4.13}$$

from which we obtain

$$\Delta H_R^0 = \Delta H_O^0 \tag{4.14}$$

$$\Delta S_R^0 = R\ln\left(\frac{[Ce'_{Ce}]^2[V_O^{\bullet\bullet}]}{[Ce_{Ce}^{\times}]^2[O_O^{\times}]}\right) + \Delta S_O^0 \tag{4.15}$$

Thus, the standard enthalpies of the two reactions are equal. Recognizing that

$$\Delta S_{config} = -R\ln\left(\frac{[Ce'_{Ce}]^2[V_O^{\bullet\bullet}]}{[Ce_{Ce}^{\times}]^2[O_O^{\times}]}\right) \tag{4.16}$$

it is observed that the standard reduction enthalpy, ΔS_R^0 does not include the configurational entropy contribution, i.e.

$$\Delta S_R^0 = \Delta S_O^0 - \Delta S_{config} \tag{4.17}$$

The difference arises from the fact that the defect chemical notation only incorporates sites that actively participate in the redox reaction. Creating 1 oxygen vacancy in N units of ceria involves only 1 out of 2N oxygen sites and 2 out of N Ce sites. Thus, independent of the initial and final non-stoichiometry, the reaction describes a transformation from an ordered lattice of $\mathrm{O}_\mathrm{O}^{\times}$ and $\mathrm{Ce}_\mathrm{Ce}^{\times}$ to an ordered lattice of $\mathrm{V}_\mathrm{O}^{\bullet\bullet}$ and Ce'_Ce, resulting in zero configurational entropy change. In contrast, the partial molar reaction treats the system as a whole – including sites that are not actively involved

in the reduction reaction. It describes a chemical change from one non-stoichiometric structure to another infinitesimally different non-stoichiometric structure, and hence embodies the configurational entropy change. This distinction becomes important when the partial molar quantities are used in conjunction with Eq. 4.5 to re-calculate the isotherms in the presence of impurities.

4.3 Experimental procedure

Powders of ZDC20 were prepared by chemical synthesis route to achieve a homogenous distribution of cations in the resulting material. Stoichiometric amounts of $Ce(NO_3)_3.6H_2O$ (Sigma-Aldrich, St Louis, MO) and $ZrO(NO_3)_2.2.5H_2O$ (Alfa Aesar, Ward Hill, MA) dissolved in dilute HNO_3 were added to distilled water. EDTA and citric acid were added as chelating agents, followed by ammonium hydroxide to bring the pH of the mixture to $\sim$10. The mixture was heated at 80°C under constant stirring till the liquid content was significantly reduced and a thick polymeric precursor remained. After further drying at 120°C, the mixture was heated to 300°C in the presence of air to burn out the organic content and then calcined for 5 h at 600°C to produce ZDC20 powder. For undoped ceria, commercially available powder (99.99%, Sigma-Aldrich, St Louis, MO) was used for further processing. Details of fabrication of dense, rectangular bar-shaped samples and experimental set-up for conductivity measurements can be found in Sec. 3.3.1.

4.4 Results and discussion

4.4.1 Equilibrium conductivity

Isothermal plots of conductivity vs pO_2 are shown in Fig. 4.1 for ceria and ZDC20. For comparison, conductivity reported at 800 °C by previous studies on single crystal[101] and polycrystalline ceria[2] have been overlaid. The agreement with our work is excellent.

Under oxidizing conditions, both oxides show n type conductivity, with that of ZDC20 being nearly two orders of magnitude higher, in agreement with literature[98]. The power law dependence of conductivity on pO_2 changes from -1/5 at 750 °C to -1/6 at 850 °C. This decrease in slope is indicative of a transition from an impurity dominated extrinsic regime (Eq. 4.6) to intrinsic defect regime(Eq. 4.7). To get approximate transference numbers in this pO_2 region, we presume that the vacancy concentration is approximately fixed by impurities and the electron concentration follows from Eq. 4.6. The total conductivity then takes the form

$$\sigma_{tot} = \sigma_i + \sigma_e^0 pO_2^{-1/4}, \tag{4.18}$$

where σ_i, the fixed ionic conductivity and σ_e^0, a constant related to the reduction equilibrium constant, electronic defect equilibrium constant, impurity concentration and electron mobility, are taken to be pO_2 independent. A plot of σ_t vs $pO_2^{-1/4}$ (Fig. 4.2a) can be used to extract σ_e^0 and σ_i, and subsequently, the ionic transference number as a function of pO_2. A plot of pO_2 dependence of t_i under oxidizing conditions for ceria and ZDC20 is shown in Fig. 4.2b. Both systems show mixed conduction, with t_i ranging between 0.15 and 0.25 at 10^{-3} atm. With decreasing pO_2, the reduction of ceria causes the electronic contribution to increase and become dominant below 10^{-6} atm. ZDC20 shows lower ionic transference number compared to ceria.

Under reducing conditions, the conductivity of both ceria and ZDC is dominated by electrons. The conductivity of ceria continues to increase with decreasing pO_2, showing a marked increase in slope (from -1/5 to over -1/4) around 10^{-19} atm . This behavior has been observed previously[101] and can be correlated to a corresponding change in the non-stoichiometry[2, 1]. Duncan and co-workers have shown that beyond $\delta \sim 0.01$, associated defects such as $(Ce'_{Ce}V_O^{\bullet\bullet}Ce'_{Ce})^{\times}$ need to be considered in addition to isolated defects to understand the defect chemical origins of the pO_2 dependence of conductivity[55]. Overall, the magnitude and variation of electrical conductivity of ceria with oxygen partial pressure and temperature are consistent with literature[101, 2]. The conductivity of ZDC20 increases with decreasing pO_2

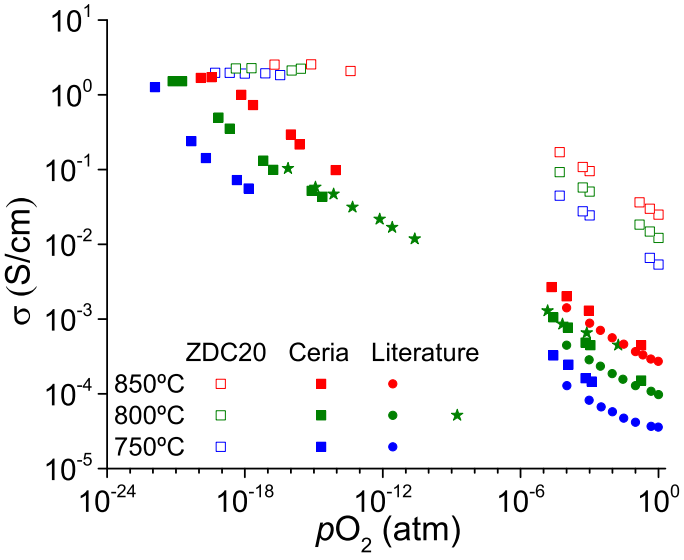

Figure 4.1: Total electrical conductivity vs pO_2 plotted on a log-log scale for ceria and ZDC20. Solid and open symbols respectively denote ceria and ZDC20. Conductivity of undoped ceria from the work of Panhans and Blumethal[2](solid circles) and Tuller and Nowick[101](stars) have been overlaid for comparison.

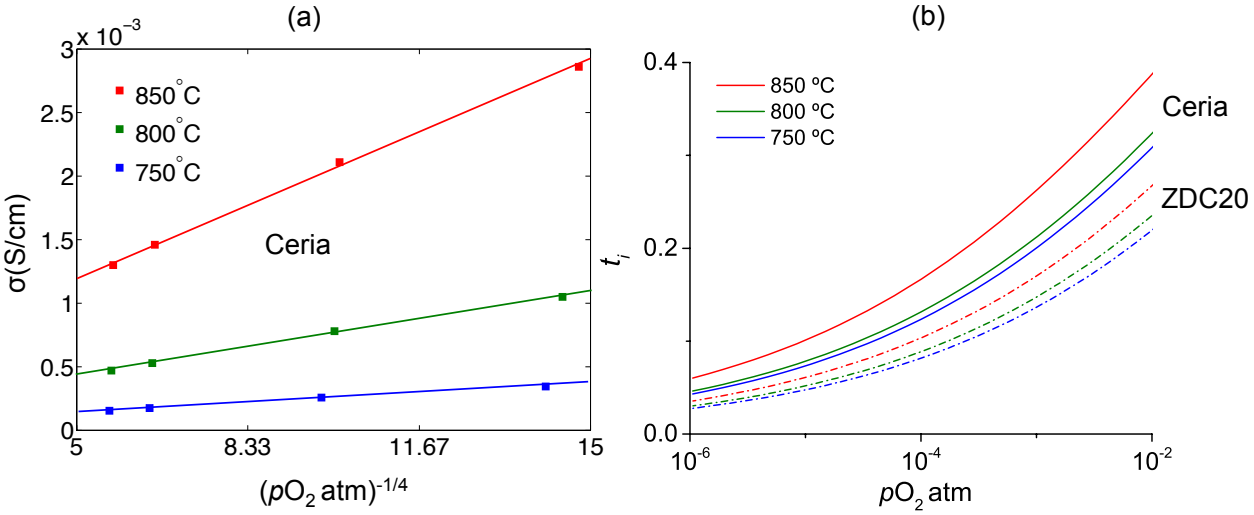

Figure 4.2: (a) Linear fits to total conductivity vs $pO_2^{-1/4}$ under oxidizing conditions were used to extract the fixed partial ionic and electronic conductivity. (b) Ionic transference numbers of undoped ceria and ZDC20 under oxidizing conditions calculated using the conductivity model described in Eq. 4.18. Both oxides are mixed conducting above 10^{-4} atm, transitioning to being completely electronic below 10^{-6} atm.

Table 4.1: Electronic mobility (u_e) of $Zr_{0.2}Ce_{0.8}O_{2-\delta}$ and $CeO_{2-\delta}$ estimated using total conductivity measured in this work, Fig. 4.1, and published non-stoichiometry data[1, 97].

$Zr_{0.2}Ce_{0.8}O_{2-\delta}$				$CeO_{2-\delta}$		
pO_2 (atm)	σ_e (S/cm)	δ	u_e (cm^2/V/s)	σ_e (S/cm)	δ	u_e (cm^2/V/s)
4.96E-04	7.20E-02	1.66E-03	5.18E-03			
9.36E-16	2.10E+00	5.00E-02	5.03E-03	5.13E-02	1.36E-03	4.90E-03
1.54E-17	2.11E+00	9.20E-02	2.74E-03	1.00E-01	2.50E-03	4.93E-03
3.45E-19	2.11E+00	1.20E-01	2.10E-03	3.49E-01	8.00E-03	5.38E-03

and plateaus at a broad maximum. Further decrease in pO_2 leads to a decrease in conductivity. Measurements were made along both oxidizing and reducing directions across the maximum to ascertain that the physical process behind the behaviour was reversible.

The conductivity values were used in conjunction with published non-stoichiometry data for undoped ceria and ZDC20 [1, 97] to estimate the electronic mobility, u_e, of ceria and ZDC at 800 °C. The results are tabulated in Table. 4.1 and schematically depicted in Fig. 4.3. Factoring in experimental measurement errors and data analytical errors, we find that the electronic mobility of ZDC20 and ceria are within 10% of each other up to $\delta < 0.01$. This is shown by a slight difference in the slopes of σ of ZDC20 and ceria vs δ. Therefore, the enhancement in electrical conductivity due to Zr addition under oxidizing conditions results from a large increase in the concentration of charge carriers relative to ceria, not from higher mobility, as has been previously reported[98]. Between 4.96×10^{-4} atm and 9.36×10^{-16} atm, the non-stoichiometry of ZDC20 changes from 1.66×10^{-3} to 5×10^{-2}, and the conductivity increases proportionally, implying that the mobility remains constant. However, with further decrease in pO_2 from 9.36×10^{-16} to 3.45×10^{-19}, the conductivity stays constant in spite of increasing non-stoichiometry, and the mobility is diminished commensurately (by a factor of 2.5).

To explain this roll-over in conductivity from n to p type, we recall that electronic conduction in ceria occurs through small polaron hopping from filled 4f states in Ce^{3+} to empty 4f states in Ce^{4+}. The concentration is proportional to $[Ce'_{Ce}]$, while the mobility varies as $[Ce^{\times}_{Ce}]$, both of which are related to the vacancy concentration,

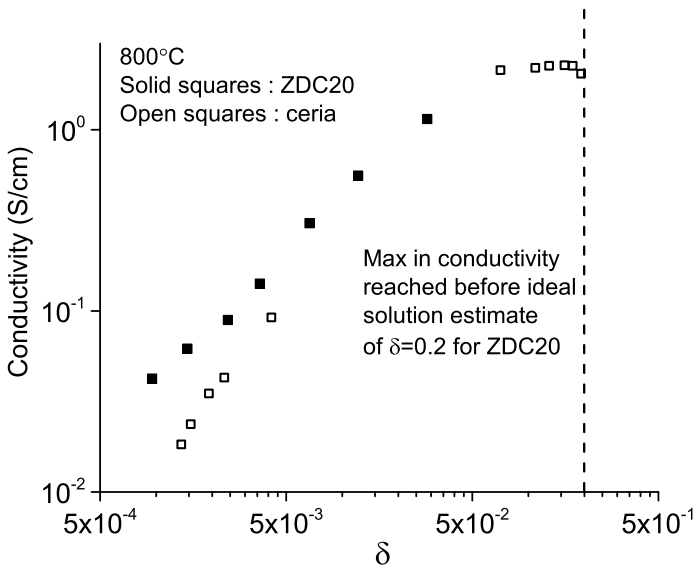

Figure 4.3: Electrical conductivity of ceria and ZDC20 vs non-stoichiometry at 800°C. For $\delta < 0.01$, the conductivity of both oxides varies linearly, implying concentration independent mobilities. Close to $\delta \sim 0.1$, the conductivity of ZDC20 reaches a broad maximum.

$[V_O^{\bullet\bullet}]$. This gives rise to a parabolic dependence of electronic conductivity on the vacancy concentration,

$$\sigma_e \propto [V_O^{\bullet\bullet}](1 - [Zr_{Ce}^{\times}] - 2[V_O^{\bullet\bullet}]). \tag{4.19}$$

The roll-over from n to p type conductivity is essentially a mobility effect, as the fraction of Ce^{3+} surpasses that of Ce^{4+}. Being redox inactive, Zr^{4+} decreases the fraction of Ce^{4+} sites available for electrons to hop to. While this does not significantly impact electron migration at low δ, its effect becomes more pronounced at higher δ. If the defects were truly isolated, the maximum σ_e would be observed at $\delta = 0.2$ for ZDC20. However, from Fig. 4.3, it is apparent that the value is reached at approximately $\delta = 0.1$, 50% of the theoretically expected value. This is an indirect, but strong evidence for defect interactions in ZDC20, which significantly decrease the mobility of electrons (equivalently, the fraction of mobile electrons) in its reduced state. Further, the shallow temperature dependence of the conductivity under

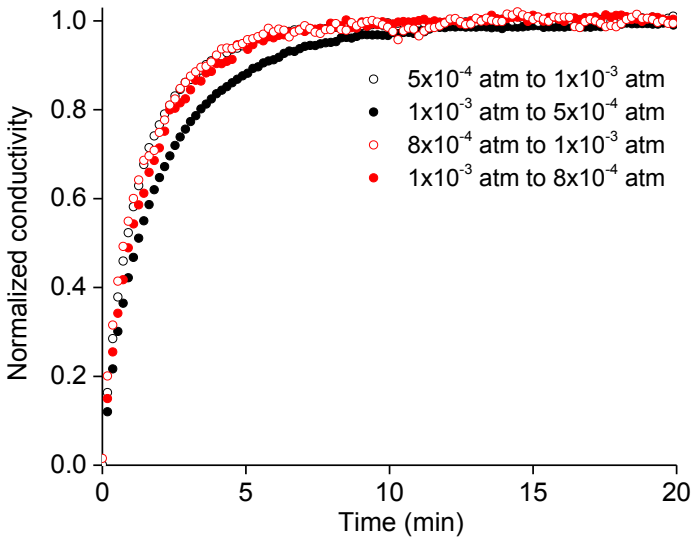

Figure 4.4: Normalized conductivity relaxation profiles for a 0.3 mm ZDC20 sample at 800 °C along oxidizing (open circles) and reducing directions (solid circles). For $\Delta pO_2 = 5 \times 10^{-4}$ atm and 1×10^{-3} atm, i.e. step change by a factor of 2 (black), the oxidizing direction is noticeably faster, while for $\Delta pO_2 : 8 \times 10^{-4}$ atm and 1×10^{-3} atm, i.e. step change by a factor of 1.25 (red), the two directions are statistically identical.

reducing conditions is yet another indication of decreasing electronic mobility with inreasing electron concentration.

4.4.2 Oxygen transport

The notion of a small step change in pO_2 depends on the sensitivity of the kinetic parameters and conductivity to pO_2. To reliably ascertain if the step is small enough, the relaxation profiles along oxidizing and reducing directions between the initial and final pO_2 must look statistically identical, as illustrated in Fig. 4.4 for a 0.3 mm thick ZDC20 sample. Between $5{\times}10^{-4}$ atm and $1{\times}10^{-5}$ atm (factor of 2), the relaxation proceeds significantly faster along the oxidizing switch compared to the reducing switch D_{Chem}, whereas the two look almost identical when the initial and final pO_2 are $8{\times}10^{-4}$ atm and $1{\times}10^{-3}$ atm (factor of 1.25). The same was observed for ceria as well. As such, pO_2 change by a factor of 2 (i.e. $\Delta \log(pO_2) = 0.3$) is insufficient to ensure

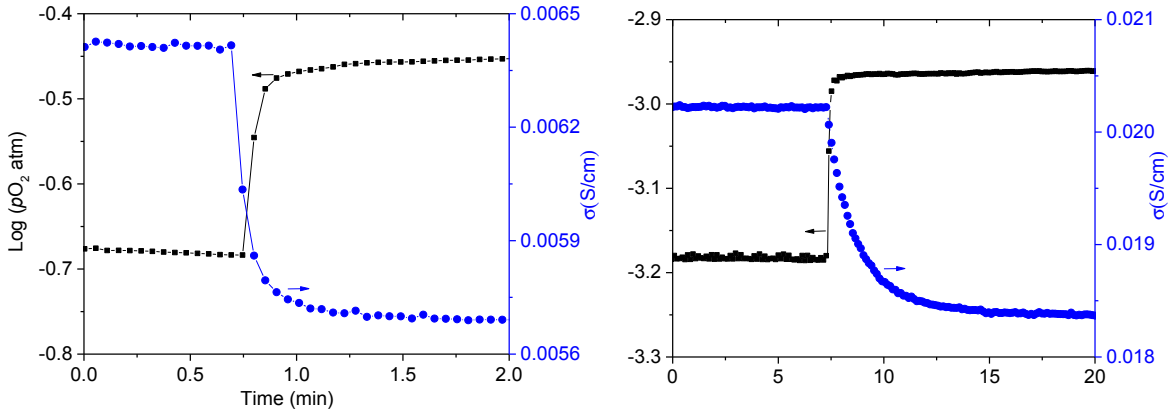

Figure 4.5: Electrical conductivity and pO_2 as a function of time for a 0.3 mm thick ZDC20 sample at 800°C. (Left) For $\Delta pO_2 = 0.21$ atm to 0.35 atm, the relaxation is complete in under 5 seconds, comparable to reactor flush times of 2-3 seconds. (Right) For $\Delta pO_2 = 6 \times 10^{-4}$ atm and 1×10^{-3} atm, the process takes 8 minutes, about 100 times longer.

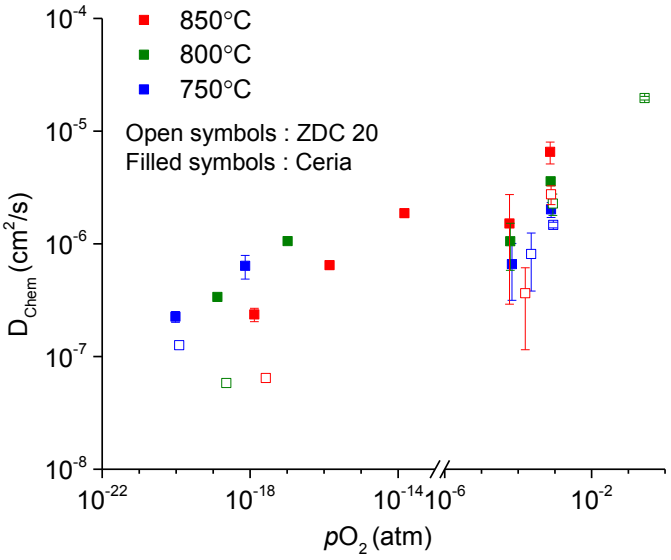

Figure 4.6: D_{Chem} vs pO_2 at 750°C, 800°C and 850°C for undoped ceria (solid squares) and ZDC20 (open squares). ZDC20 shows dramatically lower D_{Chem} compared to undoped ceria under reducing conditions. Under oxidizing conditions, the effect is less pronounced. The D_{Chem} for both the oxides show a strong dependence on pO_2 under oxidizing conditions.

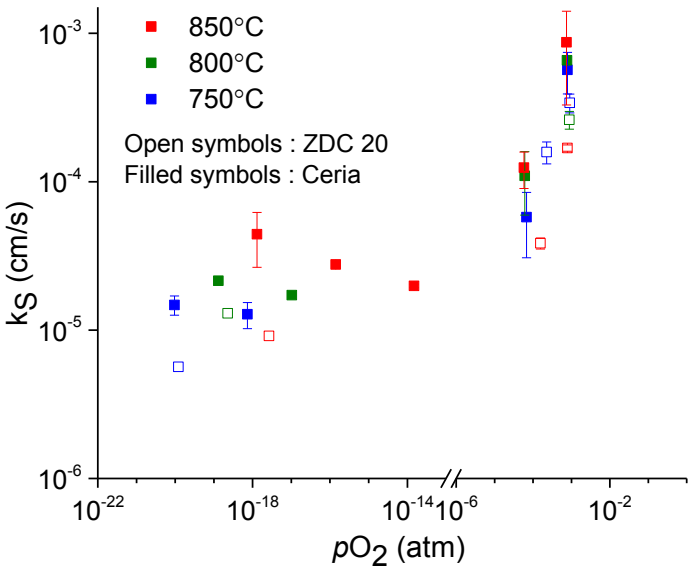

Figure 4.7: k_S vs pO_2 at 750°C, 800°C and 850°C for undoped ceria (solid squares) and ZDC20 (open squares). Again, ZDC20 shows lower k_S compared to undoped ceria under reducing conditions. Under oxidizing conditions, the effect is less pronounced. As with D_{Chem}, the k_S of both the oxides show a strong dependence on pO_2 under oxidizing conditions.

that D_{Chem} and k_S for 20 % Zr doped ceria are constant in this range, emphasizing the need to verify the equivalence between oxidizing and reducing directions uniquely for each material under study and establish the maximum allowable step size in pO_2. As a further proof of the strong dependence of D_{Chem} and k_S on pO_2 under oxidizing conditions, relaxation profiles about mean pO_2 of 10^{-1} and 10^{-3} atm are shown in Fig. 4.5. The conductivity relaxation profile at 10^{-1} atm nearly follows the pO_2 change, re-equilibrating in under 5 seconds, while the process takes about 10 min at 10^{-3} atm - a nearly 100 fold increase. In fact, D_{Chem} and k_S , plotted in Figs. 4.6 and 4.7, display nearly identical dependence on pO_2, decreasing by an order of magnitude between 10^{-1} and 10^{-6} atm. For the chemical diffusion coefficient, this could be attributed to the conductivity term or/and the thermodynamic factor, based on Eq. 3.22. The conductivity term can be readily computed as a function of pO_2 using the partial electronic conductivity and ionic transference numbers estimated in

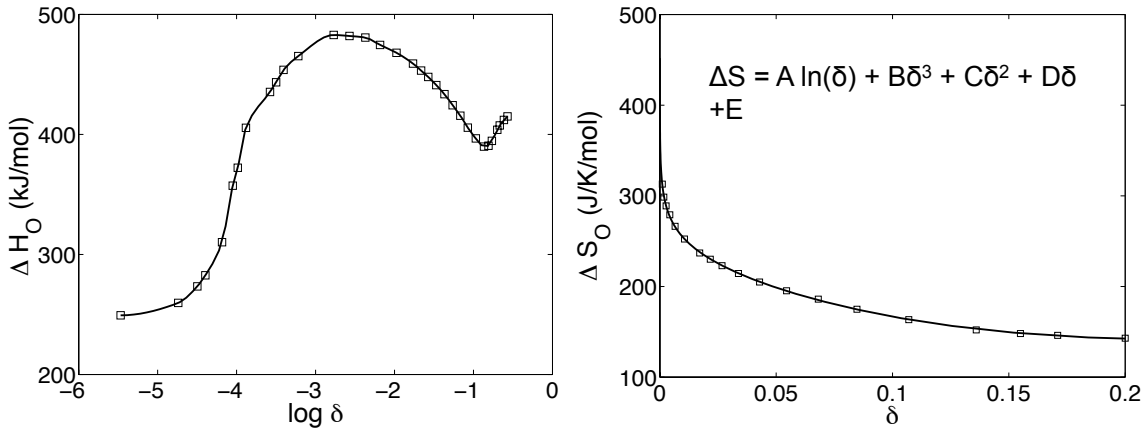

Figure 4.8: (Left) ΔH_O (per mole of oxygen atoms) vs δ from the work of Panhans and Blumenthal.[2]. Interpolation based on a cubic hermite polynomial was used to capture the functional form (line). (Right) ΔS_O vs δ from Panlener et al[1] and the fit (line) using a configurational entropy term and a cubic polynomial correction.

Sec. 4.4.1. It shows the opposite trend to that of D_{Chem}, increasing by a factor of two as $p\mathrm{O}_2$ decreases from 10^{-1} to 10^{-6} atm. This leaves the thermodynamic factor, Γ,

$$\Gamma = \frac{1}{4F^2}\frac{\partial \mu_O}{\partial c_O} \tag{4.20}$$

which explicitly appears in the expression for k_S (Eq. 3.28) as well, as the likely cause. The thermodynamic factor can be explictly related to the oxyen partial pressure by recalling that $\mu_O = 1/2(\mu_O^0 + RT\ln(p\mathrm{O}_2))$ and $dc_O = -d\delta/V_m$, yielding

$$\Gamma = -\frac{V_m RT}{8F^2}\frac{\partial \ln p\mathrm{O}_2}{\partial \delta} \tag{4.21}$$

Quantification of Γ requires knowledge of the non-stoichiometry as a function of oxygen partial pressure. For undoped ceria, the standard partial molar oxygen enthalpy (per mole of O_2) is available for a range of δ between 10^{-5} and 10^{-1}[2]. In practice, a physical defect model is proposed to explain the observed depedence of non-stoichiometry on $p\mathrm{O}_2$, which is then used to fit the δ dependence of enthalpy and entropy. The goal of our analysis is to verify that the observed trend in the transport parameters are consistent with the behavior of the thermodynamic factor. To this

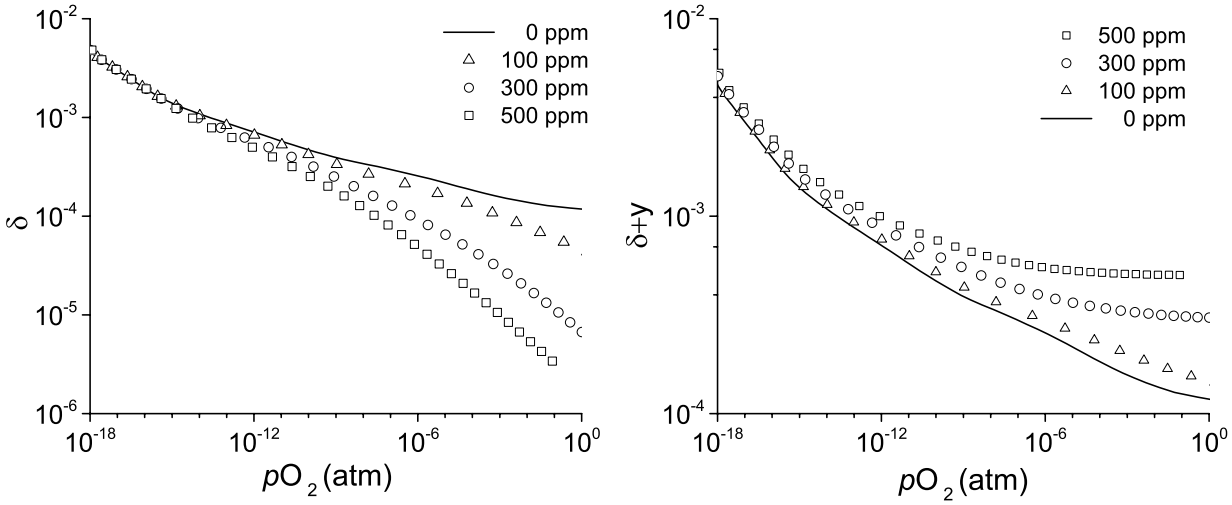

Figure 4.9: (Left) Re-calculated δ-$p\mathrm{O}_2$ isotherms at 800°C for undoped ceria in the presence of varying impurity levels (Eq. 4.5). The effect is most significant under oxidizing conditions, where the impurity generated vacancies suppress the dissociation of ceria and lower the non-stoichiometry. With decreasing $p\mathrm{O}_2$, the isotherms start to converge and eventually become indistinguishable below 10^{-14} atm. (Right) The extrinsic vacancy fraction, y, has been added to the non-stoichiometry to show the total vacancy fraction and the occurrence of an impurity dominated regime at high $p\mathrm{O}_2$.

end, a piecewise cubic Hermite polynomial was used to interpolate the functional dependence of ΔH_O^0 on δ.

The standard partial molar oxygen entropy has been reported down to $\delta \approx 10^{-3}$[1]. It is the sum of configurational and non-configurational contributions (vibrational, electronic etc) from the solid phase and the entropy of gaseous oxygen. Under oxidizing conditions, the non-stoichiometry is small (< 0.001) and the configurational entropy change becomes the dominant contribution to the total entropy. With this knowledge, the standard partial molar entropy was modeled as follows:

$$\Delta S_O^0 = A \ln \delta + B\delta^3 + C\delta^2 + D\delta + E, \tag{4.22}$$

where A, B, C, D and E are fitting constants. The first term is the configurational entropy change and the rest is a cubic polynomial correction to account for other contributions. Based on the proposed models, the fits to the partial molar enthalpy

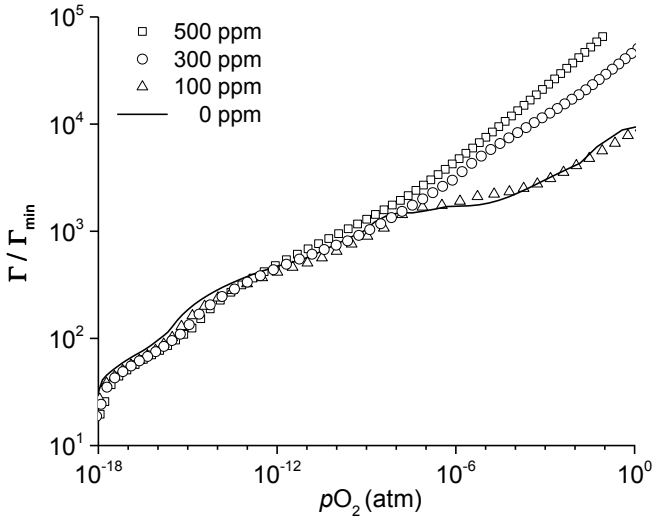

Figure 4.10: The thermodynamic factor, Γ (Eq. 4.20), at 800 °C for undoped ceria in the presence of varying impurity content. Each isotherm has been normalized by its minimum value. Under oxidizing conditions, the presence of 300 ppm impurities gives rise to an order of magnitude increase in the thermodynamic factor between 10^{-5} atm and 10^{-1} atm, which subsequently effects a similar trend in D_{Chem} and k_S vs $p\mathrm{O}_2$.

and entropy, Fig. 4.8, are excellent. Appendix A contains the tabulated data of ΔH_O and ΔS_O obtained from the literature and the fit parameters. By combining Eqs. 4.11 and 4.14, the partial molar quantities were used to obtain the reduction equilibrium constant, K_R, as a function of δ, which was then used to re-calculate the δ-$p\mathrm{O}_2$ isotherms. As discussed in Sec. 4.4.1, the presence of impurities becomes an important factor at high $p\mathrm{O}_2$. At a given non-stoichiometry, the presence of impurity-controlled extrinsic vacancies shifts the reduction equilibrium (Eq. 4.1) to the left, in accordance with the Le Chatelier principle, necessitating a lower oxygen partial pressure to achieve the same equilibrium non-stoichiometry as the impurity free oxide. By treating the impurity generated vacancy concentration, y, as a perturbation to the equilibrium, the new $p\mathrm{O}_2$ necessary to restore the original non-stoichiometry can be calculated by a simple re-arrangement of Eq. 4.5. Fig. 4.9a shows the re-calculated δ -$p\mathrm{O}_2$ isotherms at 800 °C for ceria in the presence of 0, 100, 300 and 500 ppm extrinsic vacancies. It is clear that even a 300 ppm extrinsic vacancy concentration causes the intrinsic non-stoichiometry to be suppressed by over an order of magnitude between 10^{-3} and 1 atm. Decreasing $p\mathrm{O}_2$ drives the reduction reaction forward, gradually increasing δ and offsetting the effect of impurities. Ultimately, the isotherms become indistinguishable below 10^{-12} atm. The corresponding total vacancy fractions $(y+\delta)$ are plotted in Fig. 4.9b to show the impurity dominated non-stoichiometry region.

The $p\mathrm{O}_2$ dependence of the thermodynamic factor is plotted in Fig. 4.10. Each isotherm has been normalized by its minimum, Γ_{min}, to obtain a dimensionless number. The presence of impurity generated extrinsic vacancies has two important effects on the Γ-$p\mathrm{O}_2$ isotherms at high $p\mathrm{O}_2$. First, at a given $p\mathrm{O}_2$, Γ increases with impurity content. This is understandable, since the thermodynamic factor provides a measure of the relative difficulty of reducing ceria. Second, and more important, is the result that the isotherms become markedly steeper with increasing impurity content. Between 10^{-6} and 10^{-1} atm, the thermodynamic factor increases 3 fold for the pure sample, but 10 and 20 fold in the samples with 300 ppm and 500 ppm impurities. This presents a strong case for the effect of thermodynamic factor on the $p\mathrm{O}_2$ dependence of D_{Chem} and k_S in undoped ceria. Even trace quantities of impurities, if present,

could have a strong influence on the transport properties close to stoichiometry. The chemical diffusivity transitions from a high value of electronic diffusivity, D_e, where electrons are minority charge carriers, to a much lower value of vacancy diffusivity, D_v, where ions are the minority charge carriers with decreasing $p\mathrm{O}_2$ under oxidizing conditions. Lack of meaningful thermodynamic data at high $p\mathrm{O}_2$ precludes a similar analysis for ZDC20. However, we speculate that the explanation can be extended to ZDC20 in light of the qualitative similarity between the δ -$p\mathrm{O}_2$ isotherms of the two oxides[97].

Under reducing conditions, the conduction in ceria and ZDC20 is dominated by electrons. Thus, analysis of the bulk conductivity, which is determined by the majority carrier, provides insights into electronic transport. In contrast, the chemical diffusion coefficient, which is determined by the slower moving species, provides a direct measure of the self diffusivity of vacancies, or equivalently, the vacancy mobility. For ceria, the D_{Chem} obtained from fits to ECR data decreases with $p\mathrm{O}_2$, confirming the dependence of mobility on non-stoichiometry. That D_{Chem} decreases slightly with increasing temperature can be ascribed to the convolution of thermodynamic factor and conductivity. For ZDC20, the existence of a broad plateau in the plot of conductivity vs oxygen partial pressure rendered ECR less effective in this region.

Overall, the addition of Zr leads to a decrease in the magnitude of chemical diffusivity and surface reaction rate constant of ceria. The decrease inD_{Chem} and k_S is only three-fold at worst, but its implications for fuel production rates in an actual thermochemical cycling experiment can be significant. The ECR samples are over 95% dense, with diffusion length scales of the order of hundreds of microns and relatively flat surfaces. Under such conditions, bulk diffusion is an important consideration. In contrast, samples used in the actual thermochemical cycle are highly porous (as much as 70%[21]) and possess diffusion lengths of the order of a few microns to maximize fuel production kinetics. For a = 1 micron, even if the hydrolysis and oxygen release steps were diffusion limited, a 3x decrease in D_{Chem} from 10^{-6} cm^2/s would cause the diffusion time constant, $\tau_D = a^2/D_{Chem}$ to change from 0.01 to 0.03 seconds, both of which are well below the instrumental time resolution. So, the decrease in

D_{Chem} of ceria due to Zr substitution is not expected to be detrimental to the fuel production kinetics. Indeed, for undoped ceria, the kinetics have been found to be limited by the surface reaction rates[21]. In contrast, a 3x decrease in k_S from 10^{-5} cm/s would cause the surface reaction time constant $\tau_k = a/k_S$ to change from 10 seconds to 30 seconds - a more discernible operational penalty. The ceria and ZDC20 samples used in this study have nominally identical surface areas. This effect could be exacerbated or ameliorated depending on how Zr affects the coarsening kinetics of the porous samples of ceria at high temperatures. This motivates the need for performing both small and large step change ECR tests at temperatures close to that of the oxygen release step to explore the role of surface kinetics and the effect of small vs large driving forces on the relaxation profiles.

4.5 Conclusions

We investigated the effect of 20% Zr doping on the electrical conductivity and oxygen transport properties of ceria using electrical conductivity relaxation. Measurements were performed at 750°C, 800° and 850°C over a range of oxygen partial pressures. Under oxidizing conditions, both ceria and ZDC20 showed n-type, mixed conduction, with ionic transference numbers decreasing from 0.4 to less than 0.1 between 10^{-2} to 10^{-5} atm $p\mathrm{O}_2$. The conductivity of ZDC20 was two orders of magnitude higher than undoped ceria in this region. However, the enhancement in conductivity arises from higher vacancy concentration in ZDC20 under identical conditions. Contrary to previous studies, we found that Zr addition does not influence the electronic mobility at low non-stoichiometry (high $p\mathrm{O}_2$). Under reducing conditions, while the n type conductivity of ceria continued to increase with decreasing $p\mathrm{O}_2$, that of ZDC20 reached a broad maximum, eventually decreasing with $p\mathrm{O}_2$ (p type). Using recently published non-stoichiometry data for ZDC20, it was found that the electronic mobility is constant up to $\delta \sim 0.05$ and markedly decreases with further increase in δ, which explains the roll over from an n to p type conductivity. The chemical diffusion coefficient and surface reaction rate constant showed strong dependence on $p\mathrm{O}_2$ under

oxidizing conditions, varying by nearly an order of magnitude between 10^{-5} and 10^{-2} atm. The high sensitivity to $p\mathrm{O}_2$ was ascribed to the effect of extrinsic vacancies generated by lower valence cation impurities (100 - 500 ppm), that dramatically increase both the absolute value of the thermodynamic factor and its sensitivity to $p\mathrm{O}_2$ close to stoichiometry. Overall, the addition of Zr lowers the D_{Chem} and k_S of ceria in the temperature and oxygen partial pressure range of this study, the effect being more pronounced under reducing conditions. It is expected that the lowering of k_S with Zr addition would present a more significant detriment to the fuel production rates in a thermochemical cycle than the lowering of D_{Chem}.

Chapter 5

Eletrochemical determination of oxygen non-stoichiometry in mixed conducting oxide thin films

5.1 Background

Mixed ion and electron conductors (MIECs) constitute the functional components of many solid state energy conversion devices such as solid oxide fuel cells and electrolyzers[13, 14], oxygen storage catalysts[92] and reaction media in thermochemical water splitting cycles[21, 58]. The fundamental thermodynamic property that underlies these applications is the oxygen non-stoichiometry (δ) and its variation with temperature and oxygen partial pressure. Aside from defect chemistry, deviations from stoichiometry have profound effects on ion and electron transport in MIECs.

The majority of studies aimed at determining non-stoichiometry as a function of oxygen partial pressure and temperature have been performed using thermogravimetric analysis (TGA) and coulometric titration. While such measurements directly yield stoichiometry changes reliably, the long times required for sample equilibration at new measurement conditions inherently increase the chances of error due to instrument drift. Furthermore, measurements are generally limited to large samples for which weight changes are sufficiently large to be detectable. This precludes the extension of conventional 'bulk' measurement techniques to thin film geometries, which are of significant interest for many device configurations.

A few studies in the recent literature have advanced the use of AC impedance spectroscopy (ACIS) to determine the non-stoichiometry of MIECs electrochemically[107, 108, 109]. In this technique, the impedance response of the oxide is analyzed to extract a quantity called the chemical capacitance (C_{chem})[110], which is subsequently related to the oxygen non-stoichiometry. ACIS can be performed on samples in the form of dense bulk monoliths or thin films deposited on an ionically conducting substrate. In particular, the use of thin films with well defined and reproducible microstructure, volume and surface area enable faster measurements and more controlled investigation of thermodynamic properties. The greater sensitivity of electrochemical measurements compared to gravimetric methods result in better resolved data. Impedance spectroscopy also yields a wealth of time-resolved information about transport processes. On the other hand, the non-stoichiometry determined using this technique does not always agree with each other, or with those reported by TGA or coulometric titration. Some studies have found lower oxygen vacancy content in thin films of $La_{1-x}Sr_xCoO_{3-\delta}$ - a mixed conducting perovskite perovskite - than in the bulk[111, 112], while others have published essentially opposite findings[113]. It has been speculated[107] that reactivity between the film and the substrate or surface segregation of Sr could be responsible for the observed discrepancy, but a clear understanding is yet to emerge. On the other hand, the non-stoichiometry data from electrochemical measurements on thin films of $Sm_{0.15}Ce_{0.85}O_{1.925-\delta}$ [109] (SDC15) and $Pr_{0.1}Ce_{0.9}O_{2-\delta}$[107] (PDC10) compare well with the bulk values.

The area specific chemical capacitance of a bulk sample is many orders of magnitude larger than interfacial contributions to the measured capacitance. For thin films, the interfacial capacitance (C_{int}) becomes significant and its effect can be isolated from the bulk contribution by varying the film thickness or oxygen activity. Based on this, Chueh and Haile[109] reported a temperature and oxygen partial pressure independent $C_{int} = 0.0014 \mathrm{F/cm^2}$ for SDC15 thin films. For PDC10, Chen and co-authors[107] reported the absence of interfacial capacitance under oxidizing conditions (achieved using dry O_2/Ar mixtures), where Pr is redox active. Under reducing conditions (achieved using H_2/Ar/H_2O mixtures), where Ce is redox active, they

observed an interfacial contribution, $C_{int} = 3 \times 10^{-4}\mathrm{F/cm^2}$[108].

Previous chemical capacitance studies on SDC15 and PDC10 had been restricted to temperature and oxygen partial pressure regimes in which the dilute solution approximation holds (up to $\delta = 0.05$ for SDC15[87, 62]). This simplifies the analytical treatment of chemical capacitance by relating it directly to the defect concentration. However such simplifications are not always accurate because the assumption of a dilute solution breaks down at a certain value of δ, beyond which the strongly ionic character of MIECs leads to the onset of defect interactions and deviations from ideality. So far, there has been no investigation relating C_{chem}, in its most general form, to δ. Given the versatility of the electrochemical method for determining non-stoichiometry, demonstrating its efficacy for a non-ideally behaved oxide would be a logical and important step forward. In this work, we determine the non-stoichiometry of cerium oxide thin films deposited on 8 mol% yttria stabilized zirconia substrates (YSZ) using AC impedance spectroscopy. Ceria was chosen as the benchmark material, since it displays both ideal and non-ideal behavior under different environmental conditions, and its redox thermodynamics are well studied[1, 2]. To probe potential grain boundary effects on the measured chemical capacitance, we studied thin films of ceria deposited under identical conditions on (001) oriented single crystal and polycrystalline YSZ substrates. A numerical procedure was developed to model the measured C_{chem} in terms of $p\mathrm{O_2}$ and integrate it to obtain δ.

5.2 Theory

The defect chemistry of undoped ceria relevant to this chapter is reviewed in Sec. 4.2. In this section, the concept of chemical capacitance and its relationship to non-stoichiometry is presented.

5.2.1 Derivation of chemical capacitance

To understand the physical origins of chemical capacitance, it is helpful to start with conventional dielectric capacitance, given by

$$C_{diel} = \frac{\partial q}{\partial E} \tag{5.1}$$

where Q is the total charge and E is the applied electric potential. In the case of a non-stoichiometric oxide, which undergoes a change in oxygen content in response to a change in oxygen chemical potential, the electrical equivalent of the chemical potential can be expressed as $E_k = \mu_k/(z_k F)$, where μ_k is the chemical potential, F is Faraday's constant and z_k denotes the charge on species k. For a sample with volume V, the total charge due to species k is given by $Q_k = z_k F V c_k$, where c_k is the volumetric concentration of species k. Using these expressions in Eq. 5.1, we get

$$C_{chem,k} = (F z_k)^2 V \frac{\partial c_k}{\partial \mu_k} \tag{5.2}$$

The total chemical capacitance is obtained by summing the contributions of the individual capacitors in series, i.e.

$$C_{chem} = \left(\frac{1}{C_{chem,ion}} + \frac{1}{C_{chem,eon}} \right)^{-1} = F^2 V \left(\frac{1}{z_{ion}^2} \frac{\partial \mu_{ion}}{\partial c_{ion}} + \frac{1}{z_e on^2} \frac{\partial \mu_{eon}}{\partial c_{eon}} \right)^{-1} \tag{5.3}$$

Subscripts *ion* and *eon* denote ionic and electronic carriers, respectively. For ceria, oxygen vacancies and electrons are the dominant ionic and electronic carriers. Under the assumption of local equilibrium, the chemical potential of a neutral oxygen, μ_O, and that of the oxygen vacancy and two electrons must be zero :

$$\mu_O + \mu_{ion} + 2\mu_{eon} = 0 \tag{5.4}$$

Simultaneously, the chemical potential of neutral oxygen in the solid and gas phase must be equal at equilibrium:

$$\mu_O(T, p\mathrm{O}_2) = \frac{1}{2}(\mu^0_{O_2}(T) + RT\ln(p\mathrm{O}_2)) \tag{5.5}$$

where $\mu^0_{O_2}$ is the chemical potential of gaseous oxygen standard state (taken to be 1 atm) at temperature T, and R is the gas constant. Using Eq. 5.4 and 5.5 and the fact that $2dc_{ion} = dc_{eon} = -2dc_O$ (electroneutrality) in Eq. 5.3, the total chemical capacitance can be expressed in terms of the oxygen content and oxygen partial pressure of the surrounding gas:

$$C_{chem} = \frac{8F^2V}{RT}\left(\frac{\partial c_O}{\partial \ln(p\mathrm{O}_2)}\right) \tag{5.6}$$

Finally, expressing the volumetric oxygen concentration in terms of the non-stoichiometry, $c_O = (2-\delta)/V_m$, Eq. 5.6 becomes

$$C_{chem} = -\frac{8F^2V\delta}{RTV_m}\left(\frac{\partial \ln \delta}{\partial \ln(p\mathrm{O}_2)}\right) \tag{5.7}$$

where V_m is the molar volume of ceria. Unlike dielectric capacitance, which scales with the area of the capacitor plates, chemical capacitance is a bulk quantity, scaling with volume. The term enclosed within brackets can be recognized as the inverse of the thermodynamic factor[88]. Physically, the chemical capacitance is a measure of the ease of reducibility of an oxide at a given non-stoichiometry. The larger the C_{chem}, the larger the change in δ in response to an electrochemical driving force.

5.2.2 From chemical capacitance to non-stoichiometry

With C_{chem} data at hand, the $p\mathrm{O}_2$ dependent oxygen non-stoichiometry in a film can be obtained by integration of Eq. 5.7 with respect to $p\mathrm{O}_2$:

$$\delta = \frac{RTV_m}{8F^2V}\int_{p\mathrm{O}_2^{ref}}^{p\mathrm{O}_2} C_{chem}\, d(\ln p\mathrm{O}_2) + \delta^{ref} \tag{5.8}$$

$p\mathrm{O}_2^{ref}$ is a reference oxygen partial pressure at which the the non-stoichiometry, δ^{ref}, is known. Thus, much like thermogravimetric analysis, impedance measurements can be used to obtain non-stoichiometry under all conditions if a reference is available for each temperature. A rigorous derivation of the impedance response of an MIEC starting with the fundamental transport equations and its relationship to C_{chem} has been dealt with elsewhere[110, 62, 114].

In the limit of ideal solution behavior, the law of mass action can be used to relate the non-stoichiometry of ceria to oxygen partial pressure (refer Eq. 4.5) :

$$\delta = \left(\frac{K_R}{2}\right)^{1/3} p\mathrm{O}_2^{-1/6} \tag{5.9}$$

which, together with Eq. 5.7, yields

$$C_{chem} = \frac{4F^2V}{3RTV_m}\delta \tag{5.10}$$

Thus, if the experimentally derived C_{chem} follows a -1/6 power law behavior with $p\mathrm{O}_2$, it can be assumed that the ideal solution approximation is valid. Together with appropriate defect chemical relations (i.e. $[\mathrm{Ce}'_{\mathrm{Ce}}] = 2[\mathrm{V}^{\bullet\bullet}_{\mathrm{O}}]$), the non-stoichiometry can be directly extracted from chemical capacitance without resorting to integration of Eq. 5.8, circumventing the reference state issue.

In the general case, integration of Eq. 5.8 is facilitated by the fact that C_{chem} typically obeys a power-law depedence on $p\mathrm{O}_2$:

$$C_{chem} = \sum_i A_i p\mathrm{O}_2^{m_i} \tag{5.11}$$

The use of multiple exponentials accommodates changes in the functional form of the dependence of C_{chem} on $p\mathrm{O}_2$ when there are multiple defect species involved, each being dominant over a certain range of $p\mathrm{O}_2$. From Eqs. 5.8 and 5.11, it follows that

$$\delta = -\frac{RTV_m}{8F^2V}\left(\sum_i \frac{A_i}{m_i} p\mathrm{O}_2^{m_i}\right) + \delta^{ref} \tag{5.12}$$

As a benchmarking step, the general model in Eq. 5.11 was used to fit published C_{chem} values for SDC15[109], which obeys the ideal solution model. The -1/4 power law depedence of both C_{chem} and δ on $p\mathrm{O}_2$ were accurately reproduced.

5.2.3 AC impedance spectroscopy

A detailed account of the fundamentals of AC impedance spectroscopy and its usefulness as an electrochemical characerization tool can be found elsewhere[115, 116]. A brief review of the operating principles and salient features of the technique is presented here.

AC impedance spectroscopy is an experimental technique for measurement of impedance response of a material. The frequency dependent impedance is obtained by sourcing a sinusoidal voltage, $V(t) = V_0 \sin(\omega t)$, and measuring the phase-shifted current response, $I(t) = I_0 \sin(\omega t + \phi)$. In most instance, the amplitude of the voltage perturbation, V_0, is kept small such that the response is linear. The phase shift is zero for a pure resistor and $-\pi/2$ radians for a pure capacitor. The complex impedance of the respective elements is given by

$$\text{Resistor} : Z_R = R \tag{5.13}$$

$$\text{Capacitor} : Z_C = \frac{1}{j\omega C} \tag{5.14}$$

where $j = \sqrt{-1}$, C is the capacitance and R is the resistance. For a simple transport process with resistance, R, and capacitance, C, in parallel, the impedance response can be shown to be

$$Z(\omega) = \frac{R}{1 + \omega^2 R^2 C^2}(1 - j\omega RC). \tag{5.15}$$

$Z(\omega)$ is commonly visualized in the form of a Nyquist plot, with the real part of the impedance ($\mathrm{Re}(Z)$) along the x-axis and the imaginary part ($\mathrm{Im}(Z)$) along the y-axis. For a parallel RC circuit, this gives rise to a semicircular arc, where the low frequency intercept on the x-axis is R and the capacitance is obtained from the frequency at maximum -$\mathrm{Im}(Z)$, $\omega_{max} = (RC)^{-1}$, also referred to as the characteristic frequency

(ω_0).

Impedance spectroscopy is commonly used to deconvolve individual contributions to charge transport in an oxide by resolving them in the frequency domain. For instance, in a polycrystalline sample, charge transport involves migration of carriers through the bulk of a grain and across grain boundaries. Typically, the latter has a larger resistance and capacitance and hence a smaller time constant ($\tau = \omega_0^{-1}$) compared to the former. As a result, grain boundary arcs manifest in the lower frequency portion of the complex impedance plot. If metal electrodes are used as current collectors, a third arc shows up at even lower frequencies, representing the electrochemical reaction at the gas-solid interface. These features are illustrated in Fig. 5.1. The difference in magnitude of the time constants dictates the extent of overlap between the semicircles. The measured Nyquist spectra can be described using equivalent circuits to extract the corresponding R and C[116, 115]. Often, the capacitors do not behave ideally and the arcs tend to be depressed semicircles. In such cases, constant phase elements are used, with an effective impedance given by:

$$Z_{CPE} = \frac{1}{(j\omega)^{\alpha} Y_0} \tag{5.16}$$

where α is an exponent and Y_0 is a constant obtained from the fit. $\alpha = 1$ for an ideal capacitor. CPE parameters are thought to arise from a distribution in time constants due to spatial inhomogeneties in real materials. For an unknown material, the suitability of the equivalent circuit model can be evaluated by varying parameters such as geometry, grain size or electrode compostion and analyzing the resulting impedance spectrum.

5.3 Experimental methods

5.3.1 Sample preparation and characterization

Thin films of ceria were deposited on both sides of $Y_{0.16}Zr_{0.84}O_{1.92}$ (YSZ16) (001) oriented single crystal and polycrystalline substrates ($10\times10\times0.5$ mm^3, MTI Corpo-

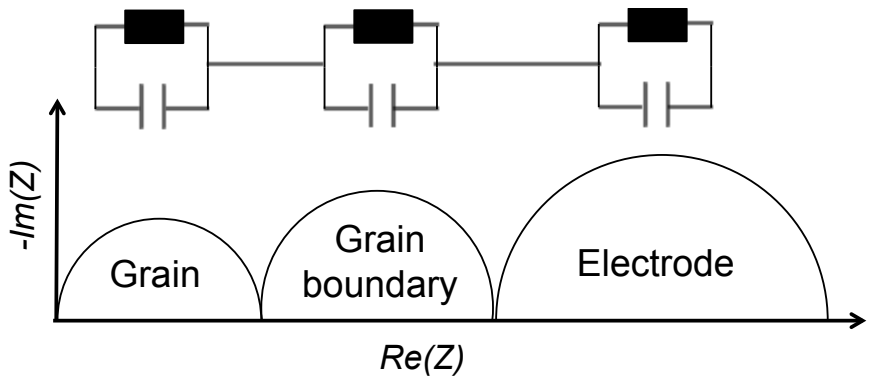

Figure 5.1: Nyquist plot for charge transport involving conduction through the grains and grain boundaries and an electrochemical reaction at the electrode

ration, Richmond, CA) using pulsed laser deposition (PLD). The target was prepared by pressing commercial ceria powder (Inframat Lot#IAM4051CEON) uniaxially at 160 MPa, then isostatically at 300 MPa and sintering at 1400 °C for 10 hours. The thin film depositions were carried out at 20 mTorr pO_2 1and a substrate temperature of $\sim$ 650 °C using a Neocera PLD system (248 nm KrF laser, 300 mJ/pulse, 20 Hz). Three different thickness on single crystal substrates were prepared - 100, 500 and 1000 nm ($\pm$5%) - whereas, only 500 nm polycrystalline films were fabricated. Some of the films were deposited through an 8 mm $\times$ 8 mm mask, while the rest of the films were deposited on the entire substrate.

Coupled $2\theta - \omega$ X-ray diffraction scans showed only (001) oriented peaks of the YSZ16 substrate and ceria (Fig. 5.2). The peak positions were perfectly matched with powder diffraction reference data. Pole figure measurements about the (200) and (220) peaks, Fig. 5.3 were used to verify alignment registry between the film and substrate and the absence of tilt boundaries. A reciprocal space map of the 200 reflection showed a slight spread along the Ω direction, possibly due to misfit dislocations in the first few nanometers of the film. The full width half maximum $\sim$ 0.8°, typical for epitaxially grown single crystal oxides of good quality. Cross section scanning electron micrographs were used to verify film thickness (Fig. 5.4a). The grain size of the poly-crystalline films were measured to be of the order of 10 microns using scanning electron backscatter micrographs (Fig. 5.4b).

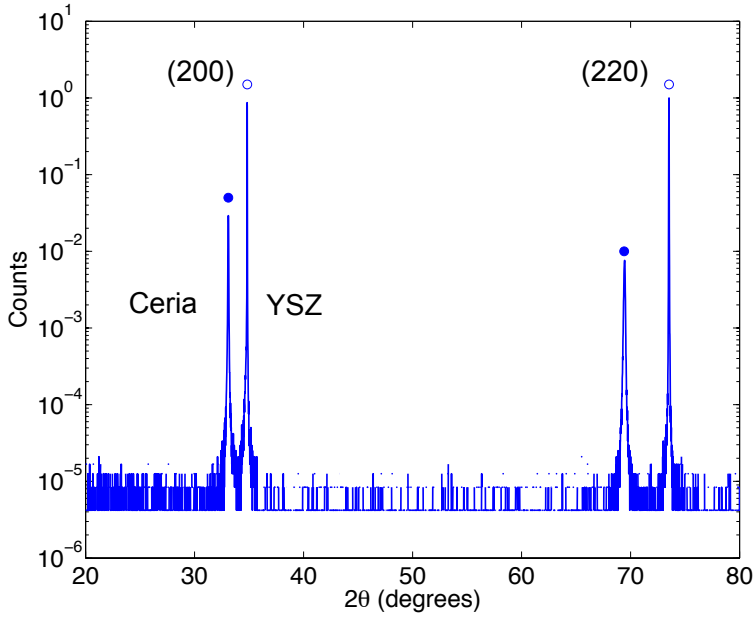

Figure 5.2: $2\theta - \omega$ coupled scan of a 500 nm film of ceria deposited on a (001) oriented YSZ substrate.

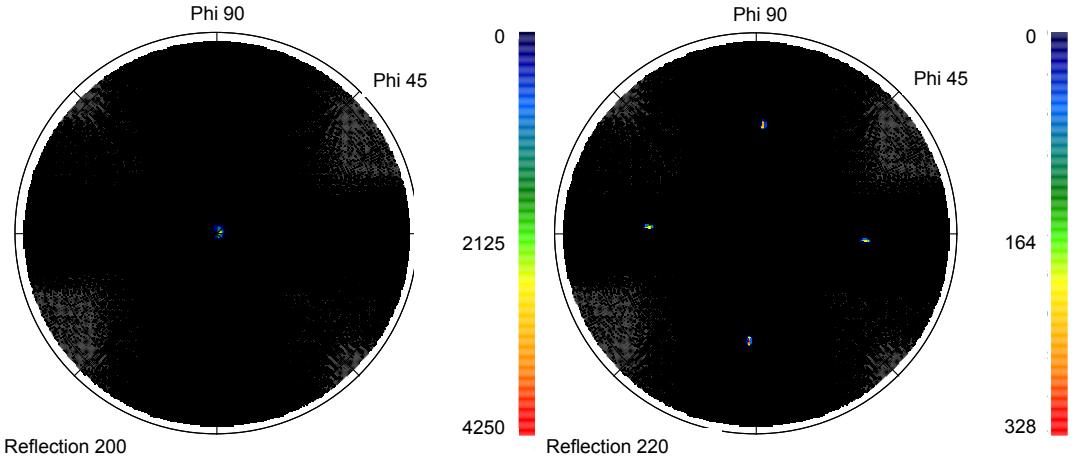

Figure 5.3: Pole figure measurements of 200 and 220 reflections of a 500 nm ceria thin film illustrating alignment registry with the (001) single crystal YSZ substrate.

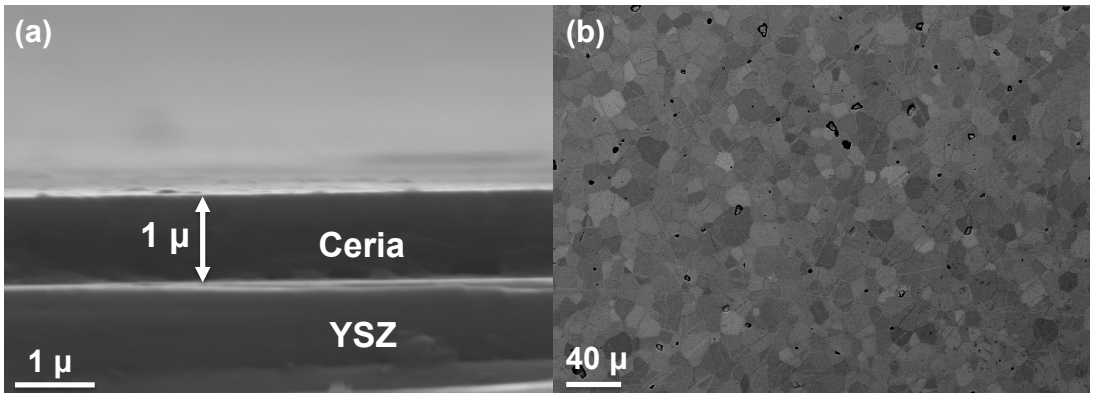

Figure 5.4: Scanning electron micrograph showing (a) the cross-section view of a 1 micron thin film of ceria on (001) YSZ single crystal. (b) the top view of a 500 nm film of ceria deposited on polycrystalline YSZ substrate.

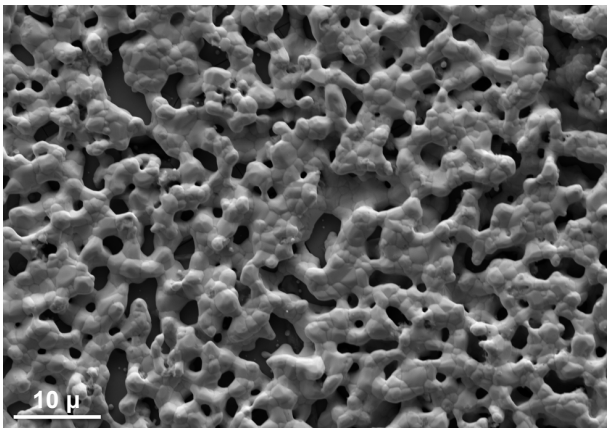

Figure 5.5: Scanning electron micrograph showing porous, interconnected Pt current collector on top of the ceria film after a 1 hr annealing step at 950 °C.

5.3.2 Electrochemical measurements

Pt (Heraeus, Item# CL11-5349)was brush painted on both sides of the ceria|YSZ|ceria symmetric cell and cured for 1 hr at 950 °C to obtain a porous, interconnected current collector, Fig. 5.5. The sample was mechanically contacted by Pt clips and placed in a gas-tight quartz reactor through which gas was supplied at a flow rate of ~ 0.7 cm/s. Dry O_2-Ar gas mixture was used to achieve pO_2 in the range of 10^{-4} to 1 atm (oxidizing conditions). Under reducing conditions, pO_2 was controlled using an H_2-H_2O-Ar buffer. The humidity was set by maintaining the water bubbler at 12 °C, while the pH_2 at the inlet was varied between 0.001 to 0.1 atm. The pO_2 in the reactor was monitored in-situ using a YSZ based oxygen sensor (Setnag MicroPoas). The AC impedance response of the cells was measured at 750°C , 800°C , 850°C and 900°C using a Solartron 1260 frequency response analyzer at frequencies between 10 mHz and 10 MHz and at 50 mV perturbations. The sample was equilibrated for 60 min at each pO_2 under reducing conditions and for 30 min at each pO_2 under oxidizing conditions prior to data collection. Equilibration was confirmed by performing two frequency sweeps in succession under each condition and ascertaining that the Nyquist spectra looked statistically identical. Equivalent circuit fits to the Nyquist spectra were performed using ZView (Scribner Associates).

5.4 Results and discussion

5.4.1 Impedance spectra and equivalent circuit modeling

The charge transport in this symmetric cell geometry involves surface reaction at the ceria|gas interface, oxygen ion transfer at the ceria|YSZ interfaces and bulk diffusion of oxygen ions through the ceria film and YSZ substrate. Fig. 5.6 shows the typical impedance response obtained under reducing conditions for the single crystalline film. There is one pO_2 dependent semi-circle with an offset from the origin. Such an impedance response can be mapped to a transport process dominated by the electrochemical reaction resistance at the surface and has been derived in detail

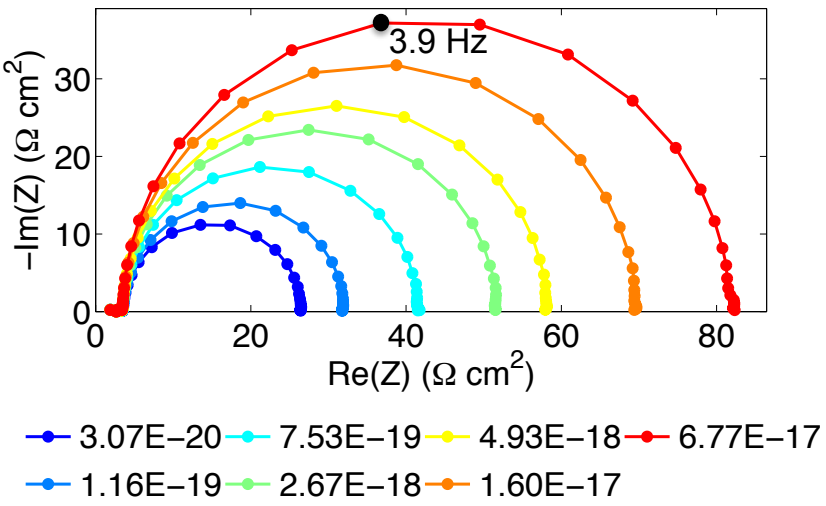

Figure 5.6: Typical impedance spectra under reducing conditions. Sample: 100 nm ceria on (001) YSZ substrate, T = 800 °C The legend denotes pO2 (in atm) corresponding to each arc.

elsewhere[114]. The offset resistance is independent of pO_2 and decreases with increasing temperature, Fig. 5.7. Since it occurs at the high frequency portion of the impedance response, the process must correspond to a bulk response. By estimating the conductivity from the resistance and its activation energy, the offset was ascribed to ion transport through the YSZ substrate, Fig. 5.8. The dielectric response of the YSZ substrate does not show up as an arc since the characteristic frequencies are beyond the instrumental limit. The diameter of the semi-circle in Fig. 5.6, corresponding to the area normalized electrochemical reaction resistance, decreases with increasing temperature and decreasing pO_2 (Fig. 5.9), consistent with the expected trend. The impedance spectra of the polycrystalline films were qualitatively identical (a quantitative comparison of the area normalized surface reaction resistance is precluded by the porous nature of the Pt current collector). The spectra were modelled using a resistor in series with an R-Q circuit. The fits to measured data had less than 1% fitting errors and α (Eq. 5.16) was in the range of 0.95-0.98, indicating near ideal capacitance. The magnitude of the capacitance was in the range of 1 - 100 mF/cm^2, typical of the values reported for C_{chem}.

The impedance response under oxidizing conditions, Fig. 5.10a contains two over-

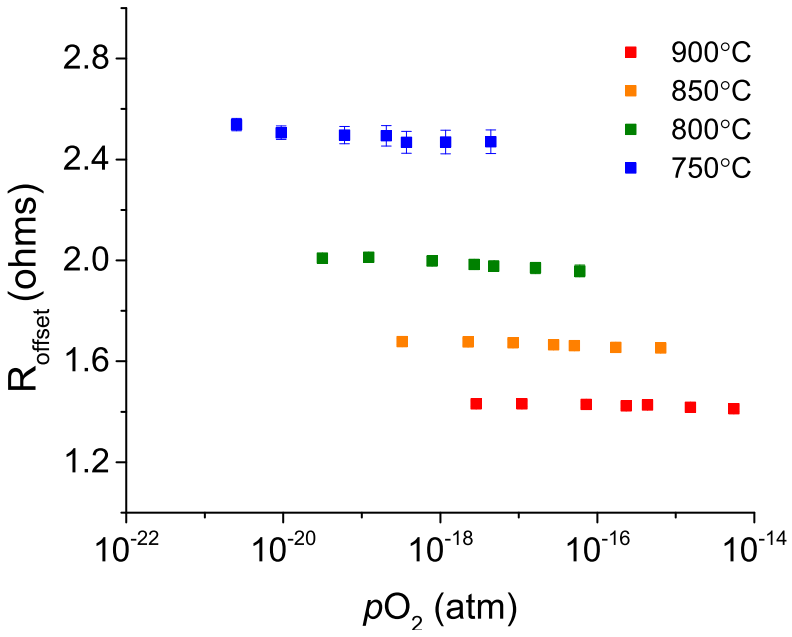

Figure 5.7: The offset resistance decreases with temperature and does not change with oxygen partial pressure.

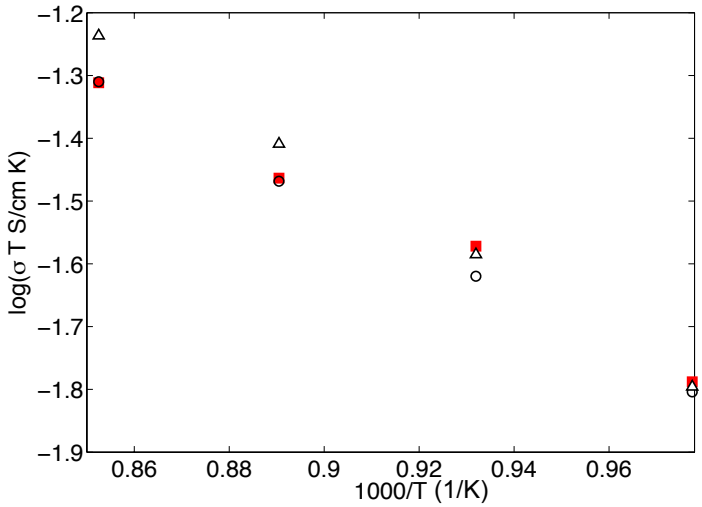

Figure 5.8: Arrhenius plot of the conductivity extracted from the offset resistance (red squares) compared with: 8 mol% (triangles)[117] and 9.5 mol% (circles)[118] YSZ.

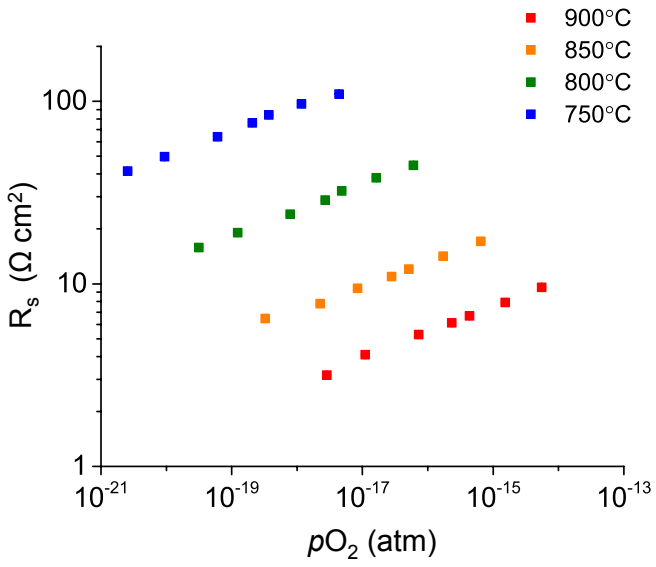

Figure 5.9: The diameter of the semicircle decreases with pO_2 and increasing temperature, consistent with the behavior of the eletrochemical reaction resistance at the gas solid interface.

lapping semi-circular arcs with a horizontal offset that increases with pO_2. It was modelled using a resistor in series with two RQ circuits. The offset resistance (Fig. 5.10b), after subtracting out the pO_2 independent contribution due to the YSZ substrate (obtained under reducing conditions), was found to correspond to the ohmic resistance of the ceria film. Under these conditions, the ionic conductivity of ceria is expected to be less than 10^{-4} S/cm, which results in a non-negligible transport resistance. This was confirmed by increasing the temperature and observing that contribution from the ceria film was diminished. The low frequency arc, once again, varied strongly with pO_2 and was hence attributed to the surface reaction. The features of the smaller, high frequency arc were found to be indepedent of pO2. Further, the arc was absent in films that were deposited on the entire YSZ substrate (without the mask). This points to the surface reaction on the exposed YSZ substrate as being the likely cause.

Over the course of the measurements, the resistance of the electrode arc was found to increase with time. Data collection under identical testing conditions, but after a 30 hour exposure to temperatures > 750°C showed that the arc nearly doubled in

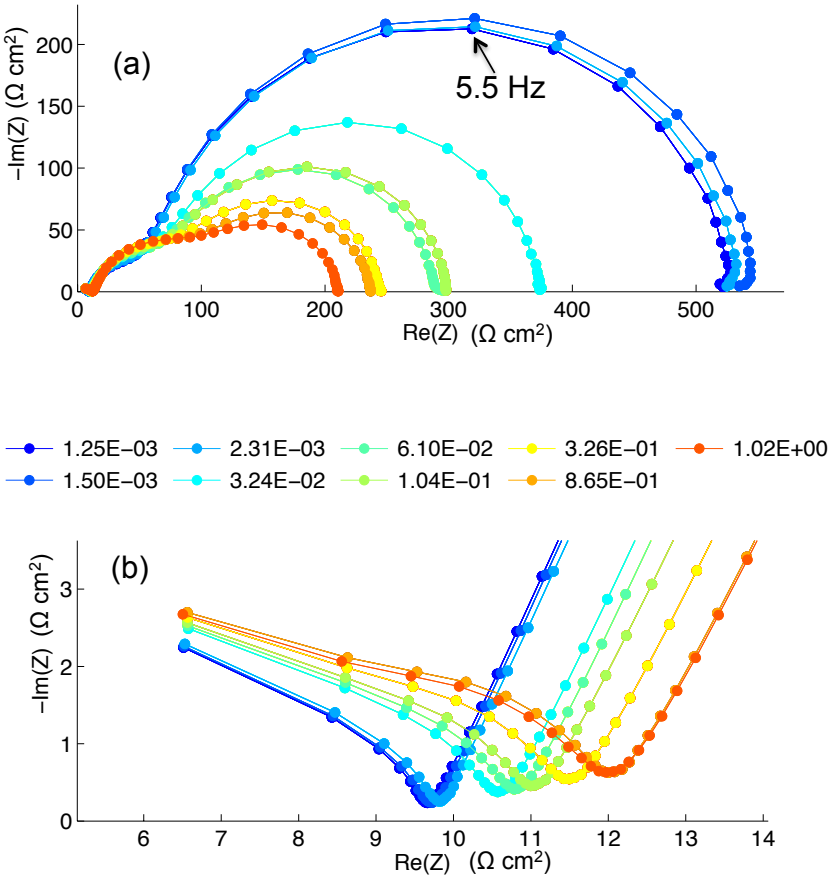

Figure 5.10: (a)Typical impedance spectra under oxidizing conditions. Sample : 500 nm ceria film deposited on a (001) YSZ substrate, T = 800 ° C. The legend denotes pO2 (in atm) corresponding to each arc. (b) Zoomed in image of the Nyquist spectra showing the pO2 dependent offset.

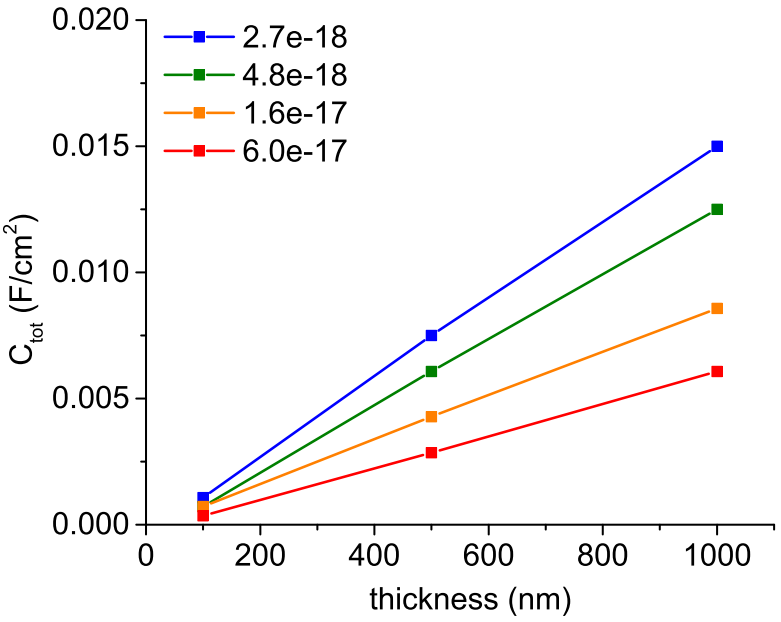

Figure 5.11: Area normalized total capacitance vs film thickness at a constant pO_2. The linear fits pass through the origin, implying that interfacial capacitance is negligible in undoped ceria.

size. We hypothesize that this increase results from coarsening of the Pt electrode microstructure. The resistance dropped sharply after the sample was brush painted with an additional layer of Pt and tested again. In all such cases, it was verified upon fitting that the bulk capacitance was unchanged.

5.4.2 Chemical capacitance

Prior to analyzing trends in the capacitance data, it is necessary to separate the bulk from the interfacial capacitance, C_{int}. Since chemical capacitance scales with volume, varying the sample thickness while keeping the substrate dimensions fixed can be used to back out the volume specific C_{chem} from the slope and C_{int} from the intercept, as shown in Fig. 5.11. The area normalized capacitance scales with thickness, as anticipated, and the linear fit passes through the origin upon extrapolation for all oxygen partial pressures, implying that C_{int} is insignificant compared to C_{chem} in undoped ceria. In contrast, under similar partial pressures, but lower temperatures, Sm and

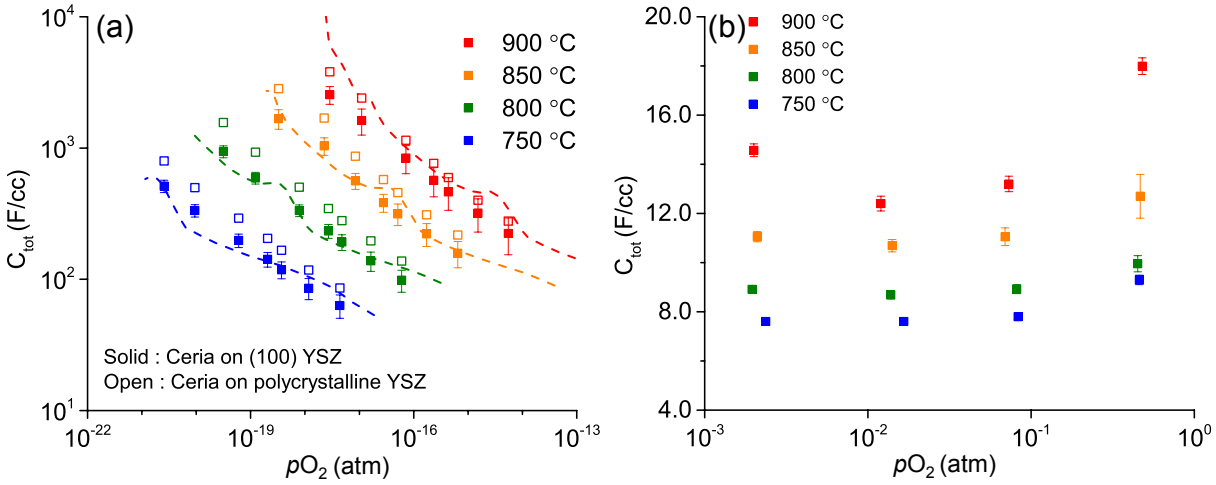

Figure 5.12: Chemical capacitance extracted from the impedance response under (a) reducing conditions and (b) oxidizing conditions. Open and solid points denote polycrystalline and single crystal thin films respectively. For comparison, bulk non-stoichiometry from literature[1](lines) have been overlaid under reducing conditions.

Pr doped ceria have been reported to exhibit an interfacial capacitance[107, 109] in the range of 3×10^{-4} to 1.4×10^{-3} F/cm^2. Further, its magnitude was found to be largely invariant with temperature and oxygen partial pressure, which tied its origin to a physical quantity that is also independent of pO_2 and temperature. Common to both the aliovalently doped oxides is a large extrinsic vacancy concentration, fixed by the trivalent dopant (Sm^{3+} in SDC15; under reducing conditions, Pr exists as Pr^{3+} in PDC10). It is conceivable that the dopants modify the interface chemistry and are responsible for the difference. One possiblity put forth by both studies was that the applied AC voltage induces a change in the concentration of surface oxygen vacancies, which gives rise to a double-layer-like capacitance. Taking the screening length to be equal to the Debye length, it was determined to be 3×10^{-4} F/cm^2 – within an order of magntide of the measured interfacial capacitances. It has also been reported that the surface of SDC films is enriched with [Ce^{3+}] compared to the bulk, and that the enhancement is almost independent of temperature and oxygen partial pressure[119]. This phenomenon could also manifest as an interfacial contribution in the impedance response. Further work is needed to identify and explain the origin of C_{int}.

Figs. 5.12a and 5.12b show log-log plots of volume specific total capacitance C_{tot} vs $p\mathrm{O}_2$ under reducing and oxidizing conditions respectively. The capacitance increases with an increase in temperature and decrease in oxygen partial pressure, consistent with Eq. 5.7. The slope of the isotherms range from -1/4 at 750 °C to nearly -1/3 at 900 °C. The polycrystalline films exhibit nearly 10% larger capacitance than the single crystal films, but exhibit similar trends. The chemical capacitance of undoped ceria has not been measured prior to our work, but approximate values can be computed using published values of partial molar enthalpy of oxygen, ΔH_O^0, and entropy, ΔS_O^0[1]. The mathematical procedure described in Sec. 4.4.2 was employed to fit the δ dependence of ΔH_O^0 and ΔS_O^0. It does not incorporate a defect chemical model, but is sufficiently accurate to capture the physical behavior of C_{chem} and extract reliable estimates with which to compare our experimentally determined values. The lines in Fig. 5.12, representing the bulk C_{chem} obtained using this procedure, show excellent agreement with our values. Under oxidizing conditions, C_{tot} is almost independent of $p\mathrm{O}_2$ and temperature. The possibility of interfacial capacitance being dominant was ruled out by plotting the thickness variation of the area normalized total capacitance. Relative to reducing conditions, the magnitude of volume specific capacitance is about 100 to 1000 times smaller. In this regime, ceria is nominally stoichiometric ($\delta \ll 10^{-3}$). Moreover, even small concentrations ($\sim$ 100 ppm) of lower valence cation impurities (e.g. Ca, Mg) can give rise to extrinsic vacancies, which further decrease the reducibility of ceria and hence, its C_{chem}. In effect, the chemical capacitance under oxidizing conditions merits further work to understand the reasons for its $p\mathrm{O}_2$ independence.

5.4.3 Non-stoichiometry from chemical capacitance

The non-stoichiometry calculated from the capacitance data is plotted on a log-log scale in Fig. 5.13. The $\delta - p\mathrm{O}_2$ isotherms deviate significantly from the expected $p\mathrm{O}_2^{-1/6}$ dependence for a dilute solution of isolated defects. At these temperatures, similar behavior has been observed in bulk ceria as well, with the exponent varying

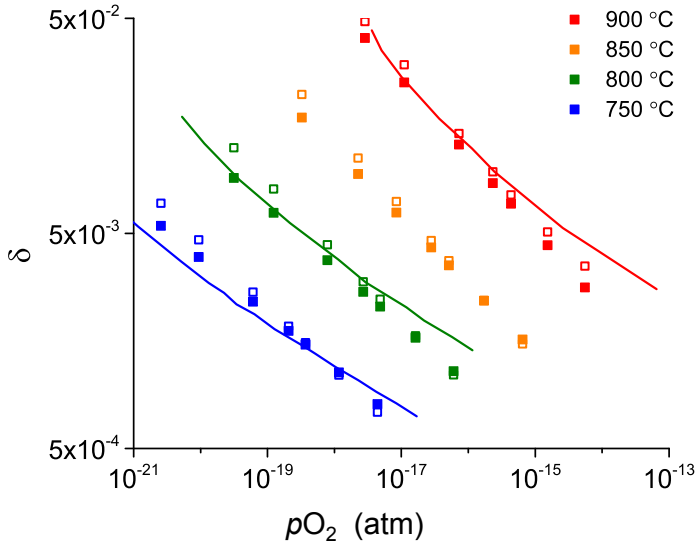

Figure 5.13: Non-stoichiometry as a function of oxygen partial pressure under reducing conditions. Open and solid points denote polycrystalline and single crystal thin films respectively. Lines represent non-stoichiometry of bulk ceria[1].

from -1/5 to -1 as $\log \delta$ varies from -3.2 to -1.2[1]. The variable pO_2 dependence has been attributed to the formation of defect associates. Duncan et al.[55] were able to accurately explain the non-stoichiometry of undoped ceria as a function of pO_2 by including intrinsic defect trimers, $(Ce'_{Ce}V^{\bullet\bullet}_{O}Ce'_{Ce})^{\times}$, in addition to isolated point defects in the defect chemical model. Above 1000 °C, the deviations from ideal behavior become substantially lower.

As with chemical capacitance, the non-stoichiometry agree very well with bulk values, implying that our single and polycrystalline thin films are essentially bulk-like in nature. The thin film non-stoichiometry start to deviate slightly from the bulk values as the intermediate pO_2 range is approached ($> 10^{-15}$ atm). This discrepancy can be addressed by extending the elecrochemical measurements to higher partial pressures, where the dependence of C_{chem} on pO_2 becomes shallower. Within experimental error, excellent agreement between thin film - both single and polycrystalline - and bulk non-stoichiometry was observed under reducing conditions, in consensus with capacitance studies on PDC10[107] and SDC15[109]. In effect, this work demonstrates that capacitance measurement using AC impedance spectroscopy can reliably

and accurately provide the non-stoichiometry in thin film mixed conducting fluorite oxides, even if the candidate system does not obey the ideal solution thermodynamic behavior. The technique offers significant time savings over thermogravimetry. The impedance measurements show considerably less scatter than TGA data, especially at low δ values, and can be used to extract interfacial transport properties if patterened current collectors with well defined surface coverage are used.

For perovskite oxides, the efficacy of this technique is still in question. Kawada and co-authors[111] measured the capacitance of an asymmetric $La_{0.6}Sr_{0.4}CoO_{3-\delta}$ | $Ce_{0.9}Ca_{0.1}O_{1.95}$ sample and reported a 45% increase in the enthalpy of reduction and nearly an order of magnitude reduction in non-stoichiometry under identical temperature and oxygen partial pressure compared to the bulk. They hypothesize a few reasons that might explain the observed discrepancy. From their plots, it is clear that a pO_2 independent capacitance starts to dominate under high oxygen partial pressures. Taking this contribution to be interfacial and subtracting it from the total capacitance would in fact exacerbate the discrepancy in the non-stoichiometry data. It is mentioned that inductively coupled mass spectrometry of the sample (post testing) revealed a 6% lower concentration of Co than expected. Considering that the films were deposited by laser ablation, the surface quality of their substrates, which were fabricated in-house by conventional ceramic processing, is extremely important. This information is not provided. In general, the lack of adequate details about sample preparation and characterization and data analysis pose a lot of questions about the validity of their results. La O' and co-authors[113] measured the capacitance of epitaxial films of $La_{0.8}Sr_{0.2}CoO_{3-\delta}$ on (001) oriented cubic YSZ substrates. The non-stoichiometry of their LSC films were nearly two orders of magnitude greater than those of bulk LSC. However, their films - measuring 25 - 135 nm in thickness - exhibited in-plane tensile strains up to 1.5% and exhibited much larger lattice constants than the bulk at room temperature. There is growing evidence that strained thin films can display dramatically different thermodynamics compared to the bulk[120, 121]. Hence, in this case, the substantial deviation from bulk is likely due to strain effects in the thin films. Further investigations on strain-free films with good compositional

control are necessary to determine if the non-stoichiometry of perovskite oxide thin films from electrochemical measurements differ from the bulk or not.

5.5 Summary

We measured the impedance response of thin films of cerium oxide to extract the chemical capacitance and oxygen non-stoichiometry over a wide range of oxygen partial pressures and temperatures. Both (001) oriented single crystal and polycrystalline films were fabricated using a suitable choice of the substrate (YSZ). The total capacitance was found to be free of any interfacial contributions, unlike the case of Sm and Pr doped ceria. Further, the effect of polycrystallinity on the magnitude of capacitance and its variation with pO_2 and T was negligible. Both C_{chem} and the calculated δ were in excellent agreement with bulk data in the literature, demonstrating the efficacy of the AC impedance spectroscopy to reliably and accurately determine the non-stoichiometry of thin film mixed conducting oxides. This work extends the scope of the electrochemical method to non-ideally behaved oxides and shows that thin films of ceria based oxides possess similar thermodynamic properties to the bulk.

Appendix A

Fits to partial molar oxygen enthalpy and entropy of ceria

Table A.1: The partial molar entropy of reduction of ceria (units of J/K/mol of oxygen vacancies) obtained from the work of Panlener et al.[1].

δ	ΔS_O	δ	ΔS_O
1.0703e-03	3.1295e+02	4.2880e-02	2.0495e+02
1.6959e-03	2.9856e+02	5.4480e-02	1.9523e+02
2.6878e-03	2.8890e+02	6.8100e-02	1.8606e+02
4.2766e-03	2.7911e+02	8.4740e-02	1.7486e+02
6.5570e-03	2.6636e+02	1.0700e-01	1.6340e+02
1.0590e-02	2.5236e+02	1.3600e-01	1.5211e+02
1.7150e-02	2.3697e+02	1.5500e-01	1.4810e+02
2.1690e-02	2.3008e+02	1.7100e-01	1.4609e+02
2.6730e-02	2.2292e+02	2.0000e-01	1.4296e+02
3.3800e-02	2.1432e+02	2.1500e-01	1.4134e+02

The partial molar entropy of reduction tabulated in Table. A.1 was fit using the model described in Eqn. 4.22,

$$\Delta S_O^0 = A \ln \delta + B\delta^3 + C\delta^2 + D\delta + E. \tag{A.1}$$

The first term represents the configurational entropy contribution while the polynomial correction is used to capture gas phase entropy and other contributions. The fit

values (in units of J/K/mol) together with 95% confidence bounds were :

$$A = -23.23(-24.41, -22.05)$$

$$B = -2549(-4199, -899.7)$$

$$C = 2301(1561, 3041)$$

$$D = -602.7(-707.1, -498.4)$$

$$E = 153.3(146.4, 160.3)$$

Table A.2: The partial molar enthalpy of reduction of ceria (units of kJ/mol of oxygen vacancies) obtained from the work of Blumenthal et al.[2]. It was fit using a cubic hermite interpolating polynomial.

δ	ΔH_O	δ	ΔH_O	δ	ΔH_O
3.40E-06	2.49E+02	3.93E-04	4.54E+02	3.38E-02	4.41E+02
1.83E-05	2.60E+02	6.05E-04	4.65E+02	4.29E-02	4.34E+02
3.18E-05	2.73E+02	1.70E-03	4.83E+02	5.45E-02	4.24E+02
4.02E-05	2.83E+02	2.69E-03	4.82E+02	6.81E-02	4.16E+02
6.54E-05	3.10E+02	4.28E-03	4.81E+02	8.47E-02	4.06E+02
8.94E-05	3.57E+02	6.56E-03	4.75E+02	1.07E-01	3.97E+02
1.03E-04	3.72E+02	1.06E-02	4.68E+02	1.36E-01	3.90E+02
1.31E-04	4.06E+02	1.72E-02	4.59E+02	1.55E-01	3.91E+02
2.65E-04	4.35E+02	2.17E-02	4.53E+02	1.71E-01	3.95E+02
3.17E-04	4.43E+02	2.67E-02	4.48E+02	2.00E-01	4.04E+02

Appendix B

Electrical conductivity relaxation studies of ceria and ZDC20 under isothermal cycling conditions

B.1 Background

Two step thermochemical cycling, as outlined in Sec. 1.3, requires considerable solid state heat recovery for attractive system efficiencies. Since the non-stoichiometry of ceria is sensitive to both partial pressure of oxygen and temperature, a practical alternative is to perform isothermal chemical cycling between a reducing gas mixture and steam[122]. While the thermodynamic driving force for oxidation of ceria is diminished at higher temperatures, this strategy allows simplification of reactor design, and obviates the mechanical stresses associated with rapid thermal cycling between high and low temperatures (in a two step process). Ceria is first reduced at 1500°C in an inert gas atmosphere (Ar, $pO_2 < 10^{-5}$ atm) and then reacted with Ar/H_2O mixture to produce hydrogen. The oxidizing gas mixture is obtained by flowing Ar through a water bubbler at 60°C, which corresponds to a saturation water vapor pressure of 0.2 atm. At 1500°C, the water dissociation equilibrium dictates a pO2 of 1.4×10^{-4} atm.

The goal of this ongoing work is to characterize the oxygen transport of ceria and ZDC20 under realistic isothermal cycling conditions, using well defined sample geometry and well controlled pO_2 changes. While small pO_2 step change experiments enable analysis of relaxation profiles using physical models and provide quantitative

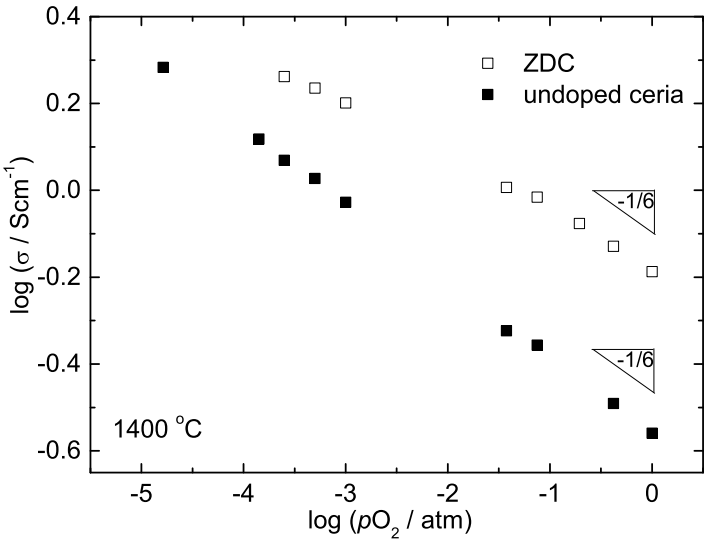

Figure B.1: Log-log plot of conductivity of ceria and ZDC20 vs pO_2 at 1400°C. The conductivity of ceria shows a -1/6 slope, which implies the point defects are non-interacting (Eq. 4.7).

data, large step changes help discern the effect of the thermodynamic driving force on fuel production kinetics.

The experimental and data analytical methodology are outlined in Sec. 3.3. A high temperature furnace capable of handling continuous operation at 1500°C was integrated into the test station. Heated gas lines were set up to enable testing using high humidity gas mixtures and prevent condensation of water vapor. A bubbler maintained at a constant temperature of 60°C (saturation pH_2O = 0.2 atm) was used to humidify the carrier gas, Ar, which was then used in the fuel production step to oxidize ceria. The experiments mentioned in this chapter were carried out at 1400 °C and between 1 atm and 10^{-5} atm oxygen partial pressure. To the best of our knowledge, this is the first quantiative study of oxygen transport under realistic isothermal chemical cycling conditions.

B.2 Conductivity at 1400 °C

The electrical conductivity of ceria and ZDC20 vs pO_2 are plotted in Fig. B.1. Both oxides show n-type conduction, increasing with decreasing oxygen partial pressure. The conductivity of ceria follows the $pO_2^{-1/6}$ behavior, which would be expected for non-interacting defects in the intrinsic regime (refer Eq. 4.7). Indeed, at such high temperatures, entropic effects become pronounced, with the result that a solid solution of isolated, point defects is thermodynamically favored over associated defects. The conductivity, essentially, reflects the dependence of the vacancy concentration on pO_2. Also, the well defined relationship suggests the use of sample conductivity as a measure of pO_2. The conductivity of ZDC20 is only a factor of three larger than that of ceria, compared to a 100 fold difference at lower temperatures (Chap. 4). It follows the -1/6 power law only up to 0.01 atm, below which the dependence starts to become shallower and approaches a maximum. This is consistent with the observation of a similar plateau in conductivity at lower temperatures (750- 850 °C) and at much lower pO_2 ($< 10^{-15}$ atm).

B.3 Relaxation behavior

Fig. B.2 shows a sample ECR profile (raw conductivity) for a 0.5 mm thick bar sample of undoped ceria and a step change from $pO_2 = 10^{-3}$ atm to 5×10^{-4} atm. Based on fits to the measured profiles, the relaxation behavior was found to be limited by the surface reaction step. In the actual thermochemical cycle, employing highly porous microstructures (with diffusion lengths of the order of a few microns), it has been observed that surface reaction limits the fuel production rate[21]. Remarkably, the surface reaction limitation persists even in the present case of dense samples with diffusion lengths of the order of hundreds of microns, indicating facile oxygen transport in the bulk of ceria. The relaxation behavior of ZDC20 was found to be limited by surface transport as well. Further, to test the effect of gas phase composition on the surface reaction step, we carried out the same pO_2 step change

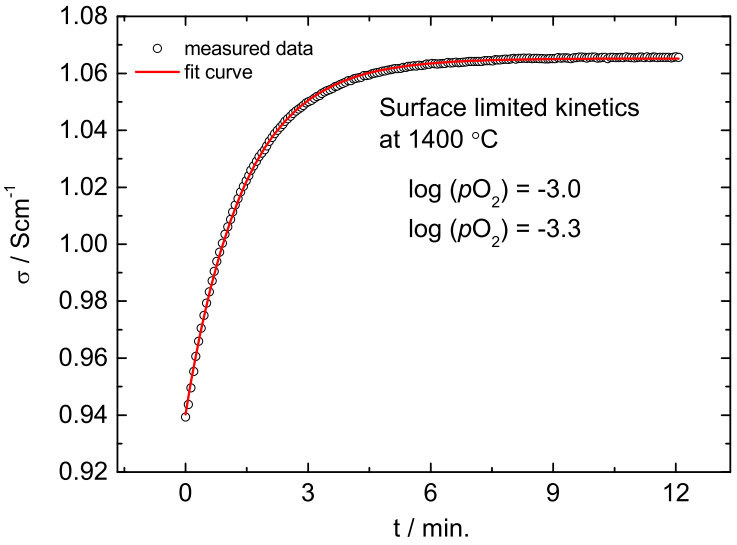

Figure B.2: Sample ECR profile (raw conductivity) in response to a step change from $pO_2 = 10^{-3}$ atm to 5×10^{-4} atm for a 0.5 mm thick ceria sample. The relaxation behavior was found to be surface limited (red line).

from 10^{-4} atm to 1.4×10^{-4} atm using a) a dry gas mixture of 100 ppm and 1000 ppm O_2 and b) wet gas mixture of Ar and H_2O ($pH_2O = 0.2$ atm). The normalized ECR profiles, plotted in Fig. B.3, show that the relaxation proceeds twice as fast in the presence of steam (at the same pO_2).

The measured k_S as a function of pO_2 are plotted in Fig. B.4. The surface reaction constant of ceria markedly decreases with pO_2 and is $\sim$ 2x those of ZDC20 between 1 atm and 10^{-4} atm and nearly the same at lower pO_2. The surface kinetics at the oxygen release step, $pO_2 = 10^{-5}$ atm, are about five times slower relative to the fuel generation step, $pO_2 = 1.4 \times 10^{-4}$ atm. Calculation of D_{Chem} was not possible in the as-prepared samples due to sluggish surface kinetics. However, a lower bound for D_{Chem} was estimated using calculated k_S, assuming $\tilde{L} = 0.03$ in Eq. 3.3.

Preliminary data for conductivity relaxation for a large step change, from $pO_2 = 10^{-5}$ atm to $pO_2 = 1.4 \times 10^{-4}$ atm, representative of the isothermal chemical cycling conditions, is shown in Fig. B.5. The oxidizing direction, representing the fuel production step, proceeds significantly faster than the oxygen release step (20 min

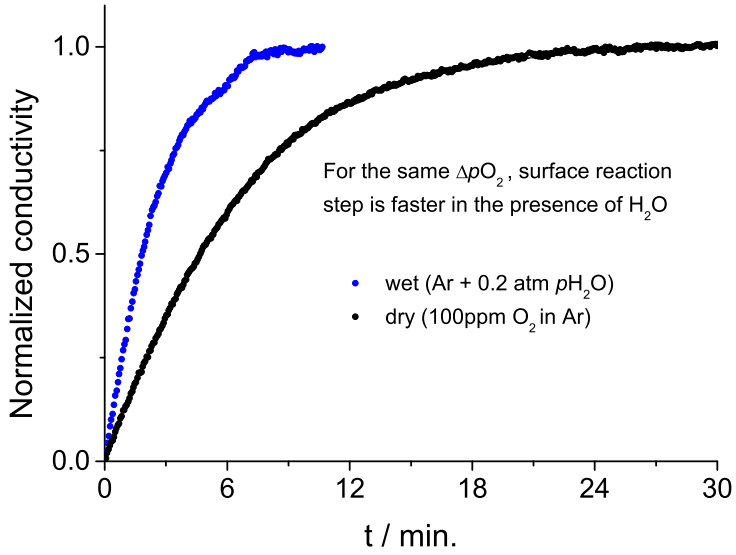

Figure B.3: ECR profile for a pO_2 step change from 10^{-4} to 1.4×10^{-4} atm using a) a dry gas mixture of 100 ppm and 1000 ppm O_2 and b) wet gas mixture of H_2O and Ar.

vs 150 min for a 0.5 mm thick sample). Work is underway to explore the effect of large driving forces on ZDC20 and enable a direct comparison between the inherent transport properties of the two systems.

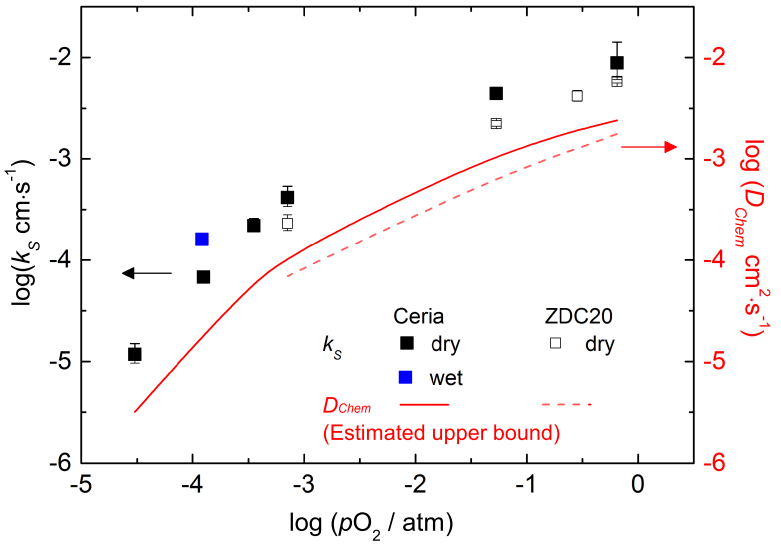

Figure B.4: k_S vs pO_2 for undoped ceria and ZDC20 at 1400°C. A lower bound for D_{Chem} was estimated using Eq. 3.3, assuming $\tilde{L} = 0.03$.

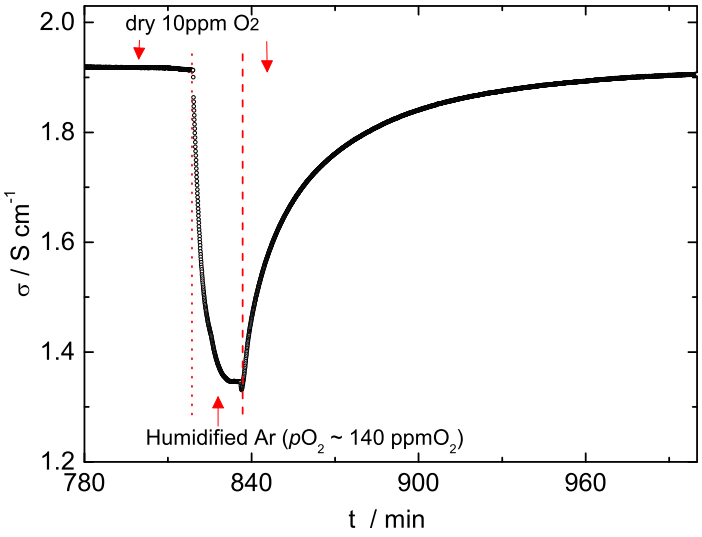

Figure B.5: ECR profiles of undoped ceria for large step changes. $\Delta pO_2 = 10^{-5}$ atm and 1.4×10^{-4} atm.

Appendix C

Thermodynamic integration to obtain reference state

The requirement of a reference δ^{ref} and $p\mathrm{O}_2^{ref}$ at every temperature is common to all conventional non-stoichiometry determination techniques. In their TGA of bulk undoped ceria, Panlener et al.[1] used $\delta^{ref} = 0$ and $p\mathrm{O}_2^{ref} = 0.1$ atm as the reference state up to 900 °C and computed corrections to the reference δ^{ref} at higher temperatures. Chen et al.[107], in their work on PDC10 thin films, used Eq. 5.10 to directly evaluate the non-stoichiometry from chemical capacitance in the region where nearly all the Pr ions are Pr^{4+} or Pr^{3+}. These values were subsequently used as the reference states. In this section, we propose a simple thermodynamic procedure that uses a known reference δ^{ref} and $p\mathrm{O}_2^{ref}$ at one temperature, T^{ref} to compute the reference $p\mathrm{O}_2$ at any other temperature T to attain the same δ^{ref}. From a statistical mechanical perspective, the redox equilibrium of ceria can be best represented by a grand canonical ensemble (μ, V, T). Indeed, experiments determine the non-stoichiometry by controlling temperature and oxygen partial pressure (more appropriately, oxygen activity, which is tied to the chemical potential). The thermodynamic function describing the state of the system is the grand potential Ω, defined by

$$\Omega = U - TS - \mu_O N_O, \tag{C.1}$$

where U is the internal energy, T is the temperature, S is the entropy of the solid, μ is the chemical potential and N is the number of oxygen atoms in the system. In

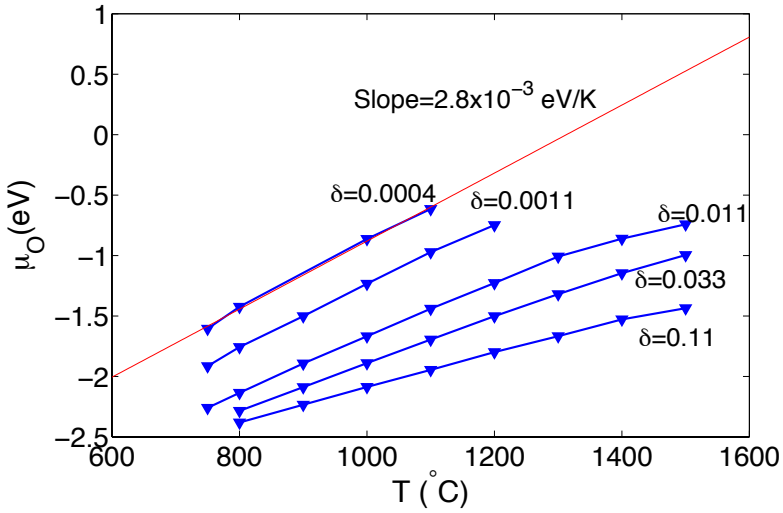

Figure C.1: Change in oxygen chemical potential with temperature for undoped ceria for a constant non-stoichiometry. The slope of each iso-δ plot, constructed from existing thermogravimetric analysis data for ceria[1] is approximately equal to the configurational entropy change at that δ.

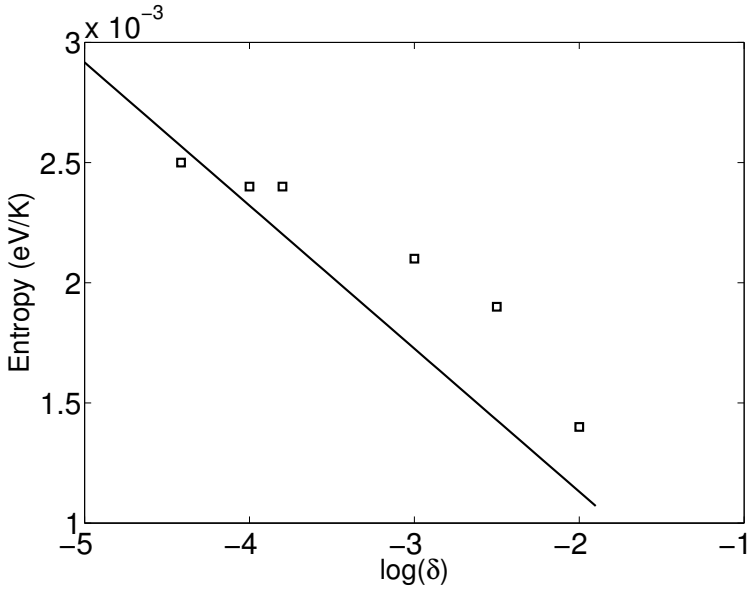

Figure C.2: Slopes of linear fits to iso-δ plots of μ_O vs T (in Fig. C.1) overlaid on a plot of ΔS_{config} vs δ.

principle, all the species that constitute the system need to be accounted for. However, the oxygen concentration is the only independent quantity – the concentrations of the rest are fixed as a consequence of charge and site conservation. At a constant temperature and pressure, creating a vacancy is associated with a change in the grand potential:

$$\Delta\Omega = \Delta U - T\Delta S - \mu_O \Delta N_O. \tag{C.2}$$

$-T\Delta S$, the thermal driving force, favors vacancies at higher temperatures (since $\Delta S > 0$) while $-\mu_O \Delta N_O$, the oxygen potential driving force, favors vacancy formation at lower chemical potentials (i.e. lower $p\mathrm{O}_2$), since $\Delta N_O = -1$ (refer Eq. 2.11). The enthalpy and entropy terms are assumed to be invariant with temperature and depend only on the non-stoichiometry. Applying this to the current problem, the increase in non-stoichiometry due to an incremental increase in temperature from T^{ref} to T can be offset by suitably adjusting the chemical potential driving force in the opposite direction, i.e.,

$$\Delta\mu_O = (T - T^{ref})\Delta S. \tag{C.3}$$

As δ approaches zero, the configurational entropy, ΔS_{config}, given by

$$\Delta S_{config} = -R \ln \left(\frac{[Ce'_{Ce}]^2 [V_O^{\bullet\bullet}]}{[Ce^{\times}_{Ce}]^2 [O^{\times}_O]} \right) \approx -R \ln(2\delta^3) \tag{C.4}$$

starts to predominate ΔS . Using this, Eq. C.3, becomes

$$\mu_O^{ref}(T) = \mu_O^{ref}(T^0) + R(T - T^{ref}) \ln(2\delta^3) \tag{C.5}$$

μ_O can be related to $p\mathrm{O}_2$ using Eq. 5.5. The standard state chemical potential for oxygen at any temperature can be obtained from NIST thermochemical tables[54] and the rest of the terms in the RHS are known. Thus, Eq. C.5 allows calculation of the oxygen partial pressure, $p\mathrm{O}_2^{ref}(T)$ at temperature T that leaves the non-stoichiometry unchanged at δ^{ref}. As an illustration, Fig. C.1 contains iso-δ plots of μ_O vs T for undoped ceria based on published non-stoichiometry data by Panlener et al.[1]. As

δ decreases, the slope of the linear fit to μ_O vs T starts to increase, which is a consequence of increasing configurational entropy change. A plot of the slopes of iso-δ lines in Fig. C.1 versus δ, illustrated in Fig. C.2, shows that the magnitude of the slope becomes roughly equal to $\Delta S_{config}(\delta)$ with decreasing δ.

Bibliography

[1] R. J. Panlener and R. N. Blumenthal. *J. Phys. Chem. Solids*, 13:1213–1222, 1975.

[2] M. A. Panhans and R. N. Blumenthal. *Solid State Ionics*, 60(4):279–298, 1993.

[3] U.S. Energy Information Administration. Annual energy outlook 2014. December 2013.

[4] Nathan S. Lewis. *Science*, 315(5813):798–801, 2007.

[5] M.G. Walter, Warren.E.L, J.R. McKone, S.W. Boettcher, Q.X. Mi, E.A. Santori, and S.N. Lewis. *Chem. Rev.*, 110:6446–6473, 2010.

[6] James R. McKone, Nathan S. Lewis, and Harry B. Gray. *Chem. Mater.*, 26(1):407–414, 2014.

[7] T. Nakamura. *Solar Energy*, 19(5):467 – 475, 1977.

[8] A. Steinfeld. *Int. J. Hydrogen Energy*, 27(6):611 – 619, 2002.

[9] Aldo Steinfeld. *Solar Energy*, 78(5):603 – 615, 2005.

[10] Tatsuya Kodama and Nobuyuki Gokon. *Chem. Rev.*, 107(10):4048–4077, 2007.

[11] Karsten Wegner, Hao C. Ly, Rodrigo J. Weiss, Sotiris E. Pratsinis, and Aldo Steinfeld. *Int. J. Hydrogen Energy*, 31(1):55 – 61, 2006.

[12] T. Kodama, Y. Nakamuro, and T. Mizuno. *J. Solar Energ-T. ASME*, 128(1):3–7, 2006.

[13] Sossina M Haile. *Acta Mater.*, 51(19):5981 – 6000, 2003.

[14] Allan J. Jacobson. *Chem. Mater.*, 22(3):660–674, 2010.

[15] P.J. Gellings and H.J.M. Bouwmeester. *Catalysis Today*, 12(1):1 – 101, 1992.

[16] K. Eguchi, T. Setoguchi, T. Inoue, and H. Arai. *Solid State Ionics*, 52(1-3):165 – 172, 1992.

[17] Mogens Mogensen, Nigel M. Sammes, and Geoff A. Tompsett. *Solid State Ionics*, 129(1-4):63–94, 2000.

[18] M. Ricken, J. Nölting, and I. Riess. *J. Solid State Chem.*, 54:89–99, August 1984.

[19] Stéphane Abanades and Gilles Flamant. *Solar Energy*, 80(12):1611 – 1623, 2006.

[20] H. Kaneko and Y. Tamaura. *J. Phys. Chem. Solids.*, 70(6):1008 – 1014, 2009.

[21] William C Chueh and Sossina M Haile. *Phil. Trans. R. Soc. A*, (1923):3269–94.

[22] William C. Chueh, Christoph Falter, Mandy Abbott, Danien Scipio, Philipp Furler, Sossina M. Haile, and Aldo Steinfeld. *Science*, 330(6012):1797–1801, 2010.

[23] Steven Demers and Axel van de Walle. *Phys. Rev. B*, 85:195208, 2012.

[24] D. A. Andersson, S. I. Simak, B. Johansson, I. A. Abrikosov, and N. V. Skorodumova. *Phys. Rev. B*, 75(3):035109, 2007.

[25] C. W. M. Castleton, J. Kullgren, and K. Hermansson. *J. Chem. Phys.*, 127(24):244704, December 2007.

[26] N. V. Skorodumova, R. Ahuja, S. I. Simak, I. A. Abrikosov, B. Johansson, and B. I. Lundqvist. *Phys. Rev. B*, 64:115108, 2001.

[27] Christoph Loschen, Javier Carrasco, K. M. Neyman, and Francesc Illas. *Phys. Rev. B.*, 75(035115):035115, 2007.

[28] Juarez L. F. Da Silva, M. Verónica Ganduglia-Pirovano, Joachim Sauer, Veronika Bayer, and Georg Kresse. *Phys. Rev. B*, 75:045121, 2007.

[29] Asha Gupta, U. V. Waghmare, and M. S. Hegde. *Chem. Mat.*, 22(18):5184–5198, 2010.

[30] David O. Scanlon, Benjamin J Morgan, and Graeme W. Watson. *Phys. Chem. Chem. Phys.*, 13:4279–4284, 2011.

[31] Zongxian Yang, Gaixia Luo, Zhansheng Lu, Tom K Woo, and Kersti Hermansson. *J. Phys. : Condens. Matter*, 20:035210, 2008.

[32] David A. Andersson, Sergei I. Simak, Natalia V. Skorodumova, Igor A. Abrikosov, and Börje Johansson. *Proc. Nat. Acad. Sci. USA.*, 103(10):3518–3521, 2006.

[33] D A Andersson, S I Simak, N V Skorodumova, I A Abrikosov, and B Johansson. *Appl. Phys. Lett.*, 90:031909, 2007.

[34] Zongxian Yang, Tom K. Woo, and Kersti Hermansson. *J. Chem. Phys.*, 124(22):224704, 2006.

[35] Hsin-Tsung Chen and Jee-Gong Chang. *J. Chem. Phys.*, 132:214702, 2010.

[36] Pratik P. Dholabhai, James B. Adams, Peter Crozier, and Renu Sharma. *J. Chem. Phys.*, 132:094104, 2010.

[37] Arif Ismail, James Hooper, Javier B. Giorgi, and Tom K. Woo. *Phys. Chem. Chem. Phys.*, 13:6116–6124, 2011.

[38] Pratik P. Dholabhai, James B. Adams, Peter Crozier, and Renu Sharma. *Phys. Chem. Chem. Phys.*, 12:7904–7910, 2010.

[39] Tanju Gürel and Resul Eryigit. *Phys. Rev. B.*, 74:014302, 2006.

[40] Gargi Dutta, Srijan Kumar Saha, and Umesh V. Waghmare. *Solid State Commun.*, 150:2020–2022, 2010.

[41] Fei Zhou, Thomas Maxisch, and Gerbrand Ceder. *Phys. Rev. Lett.*, 97:155704, 2006.

[42] A V Ruban and I A Abrikosov. *Rep. Prog. Phys.*, 71(4):046501, 2008.

[43] G Ceder, A Van Der Ven, C Marianetti, and D Morgan. *Modell. Simul. Mater. Sci. Eng.*, 8:311–321, 2000.

[44] A van de Walle and G Ceder. *J. Phase Equilib.*, 23(4):348–359, 2002.

[45] G Kresse and J Furthmüller. *Phys. Rev. B.*, 54(11169):11169–11186, 1996.

[46] P. E. Blöchl. *Phys. Rev. B*, 50:17953–17979, Dec 1994.

[47] S. L. Dudarev, G. A. Botton, S. Y. Savrasov, C. J. Humphreys, and A. P. Sutton. *Phys. Rev. B*, 57:1505–1509, Jan 1998.

[48] A Togo, F Oba, and I Tanaka. *Phys. Rev. B*, 78:134106, Oct 2008.

[49] Axel van de Walle. *Calphad*, 33(2):266–278, 2009.

[50] P. D. Tepesch, G. D. Garbulsky, and G. Ceder. *Phys. Rev. Lett.*, 74:2272, 1995.

[51] A van de Walle, M Asta, and G Ceder. *Calphad*, 26(4):539–553, December 2002.

[52] A van de Walle and M Asta. *Modell. Simul. Mater. Sci. Eng.*, 10(5):521, 2002.

[53] A van de Walle and D E. Ellis. *Phys. Rev. Lett.*, 98:266101, 2007.

[54] P.J. Linstrom and W.G. Mallard. *NIST Chemistry Web Book, NIST Standard Reference Database Number 69. Gaithersburg, MD : Natl. Inst. Standard. Tech.*, 2003.

[55] Keith L. Duncan, Yanli Wang, Sean R. Bishop, Fereshteh Ebrahimi, and Eric D. Wachsman. *J. Appl. Phys.*, 101(4):044906, 2007.

[56] S. R. Bishop, K. L. Duncan, and E. D. Wachsman. *Electrochimica Acta*, 54(5):1436–1443, 2009.

[57] Alex Le Gal, Stéphane Abanades, and Gilles Flamant. *Energy & Fuels*, 25(10):4836–4845, 2011.

[58] William C Chueh and Sossina M Haile. 2(8):735–9, 2009.

[59] J A Lane and J A Kilner. *Solid State Ionics*, 137:927–932, 2000.

[60] Masatoshi Katsuki, Shaorong Wang, Kenji Yasumoto, and Masayuki Dokiya. *Solid State Ionics*, 154-155:589–595, 2002.

[61] K Yashiro, S Onuma, A Kaimai, Y Nigara, T Kawada, and J Mizusaki. *Solid State Ionics*, 153:469–476, 2002.

[62] Wei Lai and Sossina M Haile. *J. Am. Ceram. Soc.*, 11:2979–2997, 2005.

[63] Isamu Yasuda and Tomoji Hikita. *J. Electrochem. Soc*, 141(5):1268–1273, 1994.

[64] S Kim, S Wang, X Chen, Y L Yang, N Wu, A Ignatiev, A J Jacobson, and B Abeles. *J. Electrochem. Soc.*, 147(6):2398–2406, 2000.

[65] Chang-Rock Song and Han-Ill Yoo. *Solid State Ionics*, 120:141–153, 1999.

[66] H Dünwald and C Wagner. *Z. Phys. Chem. B*, 24:53–58, 1934.

[67] Rosemary A Cox-Galhotra and Steven Mcintosh. *Solid State Ionics*, 181:1429–1436, 2010.

[68] Y. Wang, Y. Wang, and C. Xia. *J. Electrochem. Soc.*, 159(9):570–576, 2012.

[69] Annamalai Karthikeyan and Shriram Ramanathan. *App. Phys. Lett.*, 92(24):243109, 2008.

[70] Yunlong Wang, Zhuoying Zhu, and Changrong Xia. *Electrochem. Commun.*, 36(0):10 – 13, 2013.

[71] M W den Otter, L M van der Haar, and H J M Bouwmeester. *Solid State Ionics*, 134:259–264, 2000.

[72] M. W. den Otter, H. J. M. Bouwmeester, B. A. Boukamp, and H. Verweij. *J. Electrochem. Soc.*, 148(2):1–6, 2001.

[73] Bernard A Boukamp, M W den Otter, and Henry J M Bouwmeester. *J. Solid State Electrochem.*, pages 592–598, 2004.

[74] J. Crank. *The Mathematics of Diffusion*. Clarendon Press, Oxford, 2nd edition, 1975.

[75] Francesco Ciucci. *Solid State Ionics*, 239:28–40, 2013.

[76] S Wang, A Verma, Y L Yang, A J Jacobson, and Ben Abeles. *Solid State Ionics*, 140:125–133, 2001.

[77] F. A. Kröger and H. J. Vink. *Solid State Phys.-Advances in Research and Applications*, 3:307–435, 1956.

[78] H Yokokawa, T Horita, N Sakai, K Yamaji, M Brito, Y Xiong, and H Kishimoto. *Solid State Ionics*, 177(19-25):1705–1714, October 2006.

[79] Shaorong Wang, Takehisa Kobayashi, Masayuki Dokiya, and Takuya Hashimoto. *J. Electrochem. Soc.*, 147(10):3606–3609, 2000.

[80] S. Lübke and H.-D. Wiemhöfer. *Berich. Bunsen. Gesell.*, 102(4):642–649, 1998.

[81] Yueping Xiong, Katsuhiko Yamaji, Teruhisa Horita, Natsuko Sakai, and Harumi Yokokawa. *J. Electrochem. Soc.*, 151(3):A407–A412, 2004.

[82] Yueping Xiong, Katsuhiko Yamaji, Haruo Kishimoto, Manuel E. Brito, Teruhisa Horita, and Harumi Yokokawa. *J. Electrochem. Soc.*, 155(12):B1300–B1306, 2008.

[83] Hidenori Yahiro, Yukari Eguchi, Koichi Eguchi, and Hiromichi Arai. *J. App. Electrochem.*, 18(4):527–531, 1988.

[84] S. Kim, Y. L. Yang, A. J. Jacobson, and B. Abeles. *Solid State Ionics*, 121(1-4):31–36, 1999.

[85] S. Kim, S. Wang, X. Chen, Y. L. Yang, N. Wu, A. Ignatiev, A. J. Jacobson, and B. Abeles. *J. Electrochem. Soc.*, 147(6):2398, 2000.

[86] J. Kilner. *Solid State Ionics*, 129(1-4):13–23, 2000.

[87] Takehisa Kobayashi, Shaorong Wang, Masayuki Dokiya, Hiroaki Tagawa, and Takuya Hashimoto. *Solid State Ionics*, 126:349–357, 1999.

[88] Joachim Maier. *Physical Chemistry of Ionic Materials: Ions and Electrons in Solids*. John Wiley & Sons, Ltd, 2005.

[89] William C. Chueh, Chih-Kai Yang, Carol M. Garland, Wei Lai, and Sossina M. Haile. *Phys. Chem. Chem. Phys.*, 13:6442–6451, 2011.

[90] Wei Lai William C. Chueh and Sossina M. Haile. *Solid State Ionics*, 179(21-26):1036 – 1041, 2008.

[91] G. Bryan Balazs and Robert S. Glass. *Solid State Ionics*, 76:155–162, 1995.

[92] Alessandro Trovarelli. *Catal. Rev.*, 38(4):439–520, 1996.

[93] R. Di Monte and J. Kaspar. *Catal. Today*, 100(1-2):27–35, 2005.

[94] H. F. Wang, Y. L. Guo, G. Z. Lu, and P. Hu. *Angew Chem Int Ed Engl*, 48(44):8289–92, 2009.

[95] Z. Yang, T. K. Woo, and K. Hermansson. *J. Chem. Phys.*, 124(22), 2006.

[96] G. Zhou, P. R. Shah, T. Kim, P. Fornasiero, and R. J. Gorte. *Catal. Today*, 123(1-4):86–93, 2007.

[97] M. Kuhn, S. R. Bishop, J. L. M. Rupp, and H. L. Tuller. *Acta Mater.*, 61(11):4277–4288, 2013.

[98] G. Chiodelli, G. Flor, and M. Scagliotti. *Solid State Ionics*, 91(1-2):109–121, 1996.

[99] J. H. Lee, S. M. Yoon, B. K. Kim, H. W. Lee, and H. S. Song. *Journal of Materials Science*, 37(6):1165–1171, 2002.

[100] I. K. Naik and T. Y. Tien. *J. Phys. Chem. Solids*, 39(3):311–315, 1978.

[101] H. L. Tuller and A. S. Nowick. *J. Electrochem. Soc.*, 126(2):209–217, 1979.

[102] M. Yashima, H. Arashi, M. Kakihana, and M. Yoshimura. *J. Am. Ceram. Soc.*, 77(4):1067–1071, 1994.

[103] C. B. Gopal and S. M. Haile. *J. Mater. Chem. A*, 2(7):2405–2417, 2014.

[104] K. L. Duncan, Y. L. Wang, S. R. Bishop, F. Ebrahimi, and E. D. Wachsman. *J. Appl. Phys.*, 101(4), 2007.

[105] C. B. Gopal and A. van de Walle. *Phys. Rev. B*, 86(13), 2012.

[106] E. K. Chang and R. N. Blumenthal. *J Solid State Chem.*, 72(2):330–337, 1988.

[107] Di Chen, Sean R. Bishop, and Harry L. Tuller. *Adv. Func. Mater.*, 23(17):2168–2174, 2013.

[108] Di Chen, Sean R. Bishop, and Harry L. Tuller. *ECS Trans.*, 57(1):1387–1394, 2013.

[109] W. C. Chueh and S. M. Haile. *Phys. Chem. Chem. Phys.*, 11(37):8144–8, 2009.

[110] J. Jamnik and J. Maier. *Phys. Chem. Chem. Phys.*, 3:1668–1678, 2001.

[111] T. Kawada, J. Suzuki, M. Sase, A. Kaimai, K. Yashiro, Y. Nigara, J. Mizusaki, K. Kawamura, and H. Yugami. *J. of Electrochem. Soc.*, 149(7):E252, 2002.

[112] S. Wang, S. Cho, H. Wang, and A. J. Jacobson. *ECS Trans.*, 35(1):1891–1897, 2011.

[113] G. J. la O', S. J. Ahn, E. Crumlin, Y. Orikasa, M. D. Biegalski, H. M. Christen, and Y. Shao-Horn. *Angew. Chem., Int. Ed.*, 49(31):5344–5347, 2010.

[114] William Chueh. *Electrochemical and thermochemical behavior of* $CeO_{2-\delta}$. PhD thesis, California Insititute of Technology, 2010.

[115] Mark E. Orazem and Bernard Tribollet. *Electrochemical Impedance Spectroscopy.* John Wiley & Sons, Inc., 2008.

[116] Evgenij Barsoukov and J. Ross Macdonald. *Impedance Spectroscopy.* John Wiley & Sons, Inc., 2005.

[117] Di Chen, Sean R. Bishop, and Harry L. Tuller. *Journal of Electroceramics*, 28(1):62–69, 2012.

[118] P.S. Manning, J.D. Sirman, R.A. De Souza, and J.A. Kilner. *Solid State Ionics*, 100:1–10, 1997.

[119] William C. Chueh, Anthony H. McDaniel, Michael E. Grass, Yong Hao, Naila Jabeen, Zhi Liu, Sossina M. Haile, Kevin F. McCarty, Hendrik Bluhm, and Farid El Gabaly. *Chem. Mater.*, 24(10):1876–1882, 2012.

[120] Zhuhua Cai, Yener Kuru, Jeong Woo Han, Yan Chen, and Bilge Yildiz. *J. Am. Chem. Soc.*, 133(44):17696–17704, 2011.

[121] Helia Jalili, Jeong Woo Han, Yener Kuru, Zhuhua Cai, and Bilge Yildiz. *J. Phys. Chem. Lett.*, 2(7):801–807, 2011.

[122] Yong Hao, Chih-Kai Yang, and Sossina M. Haile. *Phys. Chem. Chem. Phys.*, 15:17084–17092, 2013.